



Fatigue and damage tolerance performance of additively-manufactured titanium alloys for structural application: A comprehensive review

Jianwen Liu ^{a,b}, Kai Zhang ^{a,b,c,*}, Michael J. Bermingham ^d, Hamish L. Fraser ^e, Peter Hodgson ^f, Martin Heilmaier ^g, Alberto Boretti ^{a,b}, Yuman Zhu ^{a,b,*}, Aijun Huang ^{a,b,h,*}

^a Monash Center for Additive Manufacturing (MCAM), Monash University, Notting Hill, VIC 3168, Australia

^b Department of Materials Science and Engineering, Monash University, Clayton, VIC 3800, Australia

^c School of Iron and Steel, Soochow University, Suzhou, Jiangsu 215137, China

^d School of Mechanical and Mining Engineering, The University of Queensland, St. Lucia, Brisbane, QLD 4072, Australia

^e Center for the Accelerated Maturation of Materials, Department of Materials Science and Engineering, The Ohio State University, Columbus, OH 43210, United States

^f Institute for Frontier Materials, Deakin University, Geelong, VIC 3217, Australia

^g Institute for Applied Materials, Karlsruhe Institute of Technology, Engelbert-Arnold-Straße 4, Karlsruhe 76131, Germany

^h Department of Mechanical and Aerospace Engineering, Monash University, Clayton, VIC 3800, Australia

ARTICLE INFO

Keywords:

Additive manufacturing

Titanium alloys

Damage tolerance

Fatigue

ABSTRACT

Titanium (Ti) alloys have emerged as one of the most sought-after metallic materials for additive manufacturing (AM). This originates from the unparalleled synergy of AM's capability to produce intricate geometries and the superior mechanical properties and corrosion resistance inherent to Ti alloys. Despite these benefits, AM Ti alloys continue to face persistent challenges that hinder their in-service reliability and broader adoption. Unlike conventionally manufacturing, AM introduces unique microstructural features such as non-uniform residual stresses and inhomogeneous grain structures, which often result in pronounced variability in material properties. Crucially, this variability underscores an urgent need for thorough performance evaluation of AM-produced parts, especially for critical structural applications where safety and durability are paramount. Previous reviews have broadly addressed AM Ti alloys' static properties and general processing challenges. In contrast, this review takes a comprehensive approach to examine the dynamic performance aspects—specifically, fatigue and damage tolerance—which remain insufficiently summarized yet vital for real-world applications. It deepens into the underlying mechanisms governing these properties, emphasizing the influence of key defects (e.g., porosity, segregation) as well as microstructural characteristics such as grain morphology and residual stresses. Additionally, this work expands the discussion to assess the behavior of AM Ti alloys under extreme environmental conditions (high-temperature and cryogenic operations), which are increasing demand in the automotive and energy sectors. By providing a detailed evaluation of these critical aspects, this review aims to bridge existing knowledge gaps, offering actionable insights to refine AM Ti alloy processing and enhance their structural reliability for demanding applications.

1. Introduction

Additive Manufacturing (AM), also known as three-dimensional (3D) printing, has emerged as an advanced manufacturing technology capable of producing complex-shaped components layer-by-layer [1–4]. The high design freedom offered by AM has provided significant advantages, especially in the fabrication of high-performance and customized components. As a result, AM has gained widespread interest across various industrial sectors, enabling the production of metallic

components such as fuel nozzles, combustion chambers, engine turbine blades in aircraft, and brackets and fixtures in aircraft and satellites [5–7]. Materials commonly used in AM include titanium alloys, aluminum alloys, stainless steels, nickel alloys, and others [8–11]. Among these materials, titanium alloys are particularly attractive in the aerospace industry due to their excellent specific strength, corrosion resistance, and the ability to achieve a low buy-to-fly ratio through AM [12,13]. Several AM-produced Ti alloy components have already been implemented in commercial aircraft, including EASA-approved A-Links

* Correspondence to: School of Iron and Steel, Soochow University, Suzhou, Jiangsu 215137, China.

E-mail addresses: zhangk@suda.edu.cn (K. Zhang), yuman.zhu@monash.edu (Y. Zhu), aijun.huang@monash.edu (A. Huang).

for the IAE-V2500 engine anti-icing system and multiple FAA-approved structural components for Boeing aircraft [14,15]. Furthermore, AM Ti alloy components have been successfully exposed to harsh environments, including engine compressor disks at temperatures up to 450 °C [16] and liquid hydrogen pump impellers working at -253 °C [17].

Despite these adoptions, their use for structural applications remains limited compared to conventionally manufactured Ti alloy parts. This limitation arises from the unique microstructural features introduced by the AM process, such as randomly distributed pores, elemental segregation, non-equilibrium phases, and columnar grain structures. These features can negatively impact the mechanical performance of the material and create uncertainty surrounding the quality assurance of AM Ti alloy components [18–20]. For instance, in laser powder bed fusion Ti-6Al-4V, unevenly distributed pores can act as crack initiation sites, while the presence of fine α' martensite can reduce fatigue crack growth resistance, resulting in a fatigue limit that is only 30–50 % of the ideal fatigue strength, with significant variability [21,22]. Therefore, a thorough evaluation of in-service performance is essential before AM Ti alloy components can be confidently deployed in applications. Among the in-service properties, fatigue performance is particularly important, as fatigue-related failures were reported to account for approximately 90 % of all structural failures in the aerospace industry [23,24]. Additionally, fracture toughness is a key design parameter for engineering components, as it, along with fatigue crack propagation resistance, defines the damage tolerance of materials used in load-bearing applications [25, 26]. Damage tolerance is the most crucial mechanical property of structural materials for load-bearing applications since it represents the combination of strength and toughness, which denotes the ability of the material to resist failure in the presence of porosity, cracks, or other types of damage [27].

Although several reviews on the fatigue and damage tolerance performance of AM Ti alloys are already available [28–34], the discussion on fatigue performances is predominantly limited to Ti-6Al-4V, while in terms of damage tolerance, the scope is further narrowed to laser powder bed fusion Ti-6Al-4V. Recently, research on AM titanium alloys is increasingly expanding beyond Ti-6Al-4V, with significant advances being made in β -Ti alloys, particularly those requiring high strength for load-bearing applications. Corresponding investigations into their fatigue performance are gaining increasing industrial attention [8,20, 35–38]. Additionally, these existing reviews have predominantly focused on the influence of porosity on fatigue behavior, while recent studies have identified additional critical factors previously attained, such as non-uniform residual stress [39,40] and heterogeneously distributed phase [20,41], which also significantly impact the dynamic performance of AM Ti alloys. Therefore, there is a significant gap in the literature regarding comprehensive reviews that evaluate more critical in-service performance—encompassing fatigue performance and damage tolerance properties—of various AM Ti alloys, as required by safe component design criteria.

This review aims to address the current gap by providing a state-of-the-art examination of the fatigue and damage tolerance properties of various titanium alloys produced by AM techniques. This includes the latest research on the diverse defects (e.g., porosity, segregation defects, and heterogeneous phase), unique grain and phases (such as AM Ti-specific nano-twinned precipitation), process-related attributes (like residual stress), with a particular focus on their correlation with fatigue and damage tolerance. Recent efforts to optimize such microstructure features and enhance mechanical properties are also discussed. Furthermore, the review emphasizes the in-service performance of AM Ti alloys at operational temperatures (high-temperature and cryogenic), offering valuable insights for researchers and practitioners involved in AM titanium alloy development and application. This comprehensive review aims to guide future research, eliminating the need for redundant efforts, and providing substantial benefits to the continued development of AM titanium alloys in both academic and industrial sectors.

2. Brief overviews of titanium alloys and relevant AM techniques

Over the last three decades, several types of AM technologies have been successfully implemented to various titanium alloys [42]. The intent of this section is to provide a brief overview of these alloys and relevant AM techniques as a prelude to discussing the mechanical performance, defects, and microstructure characteristics of AM titanium alloys. Herein, titanium alloys can be classified into three categories— α (α and near- α), $\alpha+\beta$, and β (metastable and stable)—based on their positions within the β isomorphous phase diagram and the phase compositions present at room temperature [12,43]. To aid comparison, a concise summary of alloy classes and their salient characteristics is provided in Table 1.

α titanium alloys: This category of alloys normally contains a minimal amount of β phase at room temperature (less than 5 vol%) [12]. Their compositions are typically enriched in α -stabilizing elements (Al, Zr, Sn) with only minor additions of β -stabilizers (Mo, Ta, Nb, W, V, Cr, Ni, Mn, Co, Fe). Commercial α titanium alloys mainly include Ti-8Al-1Mo-1V, Ti-5Al-2.5Sn, Ti-6Al-2Sn-4Zr-2Mo (Ti-6242), Ti-6Al-2Zr-1Mo-1V (TA15), and Ti-5.8Al-4Sn-3.5Zr-0.7Nb-0.5Mo-0.35Si-0.06 C (IMI 834), etc. The β transus temperatures of α titanium alloys are commonly higher than the other two, due to the lack of β stabilizers. Therefore, the α titanium alloys have good creep resistance and rational high-temperature mechanical property stability (could be up to ~600 °C), which makes it suitable for turbine engine components [44]. For instance, IMI 834 alloy has been successfully used in the compressor discs and rear axles of the Trent 700 engines in Airbus A330, operating at temperatures of up to 600 °C [45]. Furthermore, owing to the low ductile-brittle transition temperature of α -phase (often below -150 °C), α titanium alloys are ideal structural materials for cryogenic temperature applications, and have been widely employed in energy cryogenic engineering, such as liquid hydrogen pump impellers [46,47].

$\alpha+\beta$ titanium alloys: These alloys comprise more β -stabilizing elements than α titanium alloys, resulting in a higher retained equilibrium fraction of β phase at room temperature. Ti-6Al-4V is the most well-known $\alpha+\beta$ titanium alloy, and is considered as the ‘workhorse’ serving more than 50 % of titanium alloy use. The $\alpha+\beta$ titanium alloys offer moderate strength, excellent fatigue resistance, good ductility, and outstanding corrosion resistance [43]. On this basis, the $\alpha+\beta$ titanium alloys are widely used for loading-bearing and low-temperature critical components in aircraft and aero-engines, critical parts in off-shore and marine systems [12]. Since the processability, microstructures, and mechanical behavior of α and $\alpha+\beta$ titanium alloys are relatively similar, the introductions of these two types of titanium alloys processed by AM will not be separated intentionally in this work.

β titanium alloys: This class of alloys contains the highest proportion of β -stabilizing elements among titanium alloys, which disrupt the lattice bonding forces and reduce the elastic modulus (down to 45 GPa) [12]. This property makes β titanium alloys particularly attractive for biomedical implant applications [48]. These elements also allow high-temperature β phase to be fully retained upon rapid cooling (such as water quenching) to room temperature. Further subsequent aging treatment can precipitate fine α -phase (and other metastable phases) in the β -phase matrix, and hence provide strengthening. The ultimate tensile stress of the aged β titanium alloy could be significantly higher than both the α and $\alpha+\beta$ titanium alloys, so they occupy a niche in the overall application of Ti alloys in the airplane industry, particularly in the critical loading-bear parts [49,50]. For instance, Ti-5Al-2Sn-2Zr-4Mo-4Cr (Ti-17) exhibits the yield strength of 1000–1200 MPa, and is mainly used as fan disks at high-strength levels in aircraft engines. In comparison, the yield strength of cold-rolled + aged Ti-3Al-8V-6Zr-4Mo-4Zr (Beta-C) can reach up to 1500 MPa and thereby can be used in aircraft springs, fasteners, and pressure housings.

Additive manufacturing of titanium components involves two major categories based on the materials feeding methods: powder bed fusion

Table 1Summary of α , $\alpha+\beta$, and β titanium alloys: typical compositions, characteristics, and applications.

Category	Common/Commercial alloys	Typical compositions	Typical microstructures	Key characteristics	Typical applications
α titanium alloys	Ti-8Al-1Mo-1V, Ti-5Al-2.5Sn, Ti-6Al-2Sn-4Zr-2Mo, Ti-6Al-2Zr-1Mo-1V	Minimal β -stabilizers; β -phase at RT < 5 vol%	Equiaxed microstructure, α -lamellar, α -Colony	Good creep; very low Ductile-to-brittle transition temperature	Turbine engine compressor discs, cryogenic pump impellers
$\alpha+\beta$ titanium alloys	Ti-6Al-4V, Ti-6Al-3Mo-2Sn-2Zr-2Cr, Ti-6.5Al-3.5Mo-1.5Zr-0.3Si, Ti-6Al-2Mo-2Sn-2Zr-2Cr-2V	More β -stabilizers, significant retained β at RT	Bi-modal microstructure, Grain boundary α -phase, α -lamellar	Balanced strength-ductility; excellent fatigue; outstanding corrosion resistance	Fasteners, compressor blades, seawater pump shafts
β titanium alloys	Ti-5Al-2Sn-2Zr-4Mo-4Cr, Ti-3Al-8V-6Cr-4Mo-4Zr, Ti-5Al-5Mo-5V-3Cr, Ti-5Al-5Mo-5V-3Cr-1Zr, Ti-5Al-2Sn-2Zr-4Mo-4Cr	Highest β -stabilizers, β -phase retained on quench	Nano-size α precipitates, Grain boundary α -phase, Retained β -phase	Very high strength after aging; low modulus suits implants	Fan disks, springs, biomedical implants

(PBF) and direct energy deposition (DED). These techniques can be further distinguished by the type of heat source used, with the details listed below:

Laser powder bed fusion (L-PBF): L-PBF is a powder bed-based additive manufacturing process with a laser beam as the heat source and fine metal powders (with the size ranging from 10 to 100 μm) used as the feedstock materials [51]. A thin metal powder layer with a thickness ranging from 30 to 80 μm is spread evenly onto the substrate within the fabrication chamber. The controlled laser beam selectively melts the powder based on the section information from the digital design model. Once the scanning of the previous layer is completed, the fabrication piston is lowered in the z-axis direction for a layer thickness height, while the powder delivery system spreads a new layer of powder for the next selective melting process [52,53]. The full part could be formed by repeating this coating and melting process for thousands of cycles (Fig. 1a).

The relatively small laser beam spot (approximately 30–200 μm in different machines from various manufacturers) used for the L-PBF process leads to the fabricated parts with relatively high dimensional accuracy. The fabricated finish surface can reach the roughness (R_a) value of less than 10 μm [57]. The capability of fabricating complex parts in a near-net-shaped state makes the L-PBF technique very attractive for end users in different industry sectors. One example is the L-PBF fabricated Ti-6Al-4V bracket for Airbus A350, which is manufactured by LZN Laser Zentrum Nord GmbH [54]. This part adopts a topology-optimized bionic design, which leads to $\sim 30\%$ weight saving compared to the conventionally manufactured brackets (Fig. 1b).

Electron beam powder bed fusion (EB-PBF): EB-PBF is another type of powder-bed AM process similar to the L-PBF with a high-power electron beam as the heat source within a vacuum chamber. EB-PBF system consists of two main elements: the column in the upper part of the system and the work chamber in the lower part of the system [58]. The electron beam is produced by a tungsten filament or a LaB₆ crystal, and the electrons are accelerated up to 10 – 40 % of the speed of light and guided from the top gun toward the working chamber. The EB-PBF process generally involves two steps. Firstly, each layer of powder is pre-heated using a low-energy electron beam to prevent electrostatic charging and powder particle repulsion. Then, another pass using a high-energy electron beam is applied to melt the area defined by the part model (Fig. 1c) [59,60]. Substrate heating temperatures up to 1000 °C can be achieved due to the full vacuum building chamber. These features enable the titanium alloy components fabricated by EB-PBF with reduced residual stress and lower oxygen contamination. Therefore, EB-PBF is very suitable for high-performance parts like blades. One typical example is the liquid-hydrogen pump impellers made by the EB-PBF process, as shown in Fig. 1d [61,62].

Laser direct energy deposition (L-DED): L-DED is a process of feeding alloy powders or alloy wires simultaneously into the melt path

or melt pool created by a high-energy laser beam to deposit materials layer-by-layer upon a substrate plate (Fig. 1e), which is also known as Laser Engineered Net Shaping (LENS) [63]. The power of the laser used for the L-DED process ($\geq 1\text{ kW}$) could be significantly larger than that for the L-PBF process ($\leq 500\text{ W}$). It is one of the direct energy depositions (DED) techniques. Since the L-DED fabrication of titanium alloys is very oxygen reactive, inert gas like argon and helium is required to protect the molten pool and solidified parts from oxidation and exposure. Compared to L-PBF, L-DED is more suitable for building large-scale parts since its working space is not limited by the powder bed dimensions. For instance, a large-scale titanium alloy spar with a length of over 1 m was manufactured by L-DED for airplane applications (Fig. 1f) [64]. Furthermore, the building rate of L-DED titanium alloys is much higher than the L-PBF process, with more than ten kilograms of material deposited in one hour with optimal processing parameters.

Wire arc additive manufacturing (WAAM): WAAM is another type of DED technique, with the electric arc as the heat source and metallic wires as feeding materials [65,66]. With its capability of high deposition efficiency (it could deposit tens of kilograms in one hour), the WAAM technique is considered another feasible AM technique to fabricate large-scale parts (Fig. 1g) [67,68]. For instance, WAAM-3D Company fabricated a prototype of a large-scale Ti-6Al-4V alloy pressure vessel for a space exploration task, $\sim 1\text{ m}$ in height and 8.5 kg in weight, as shown in Fig. 1h [56,65]. By using WAAM to manufacture these parts, $\sim 65\%$ of production lead time was saved and $\sim 80\%$ of raw material usage was reduced with the performance criteria maintained. The disadvantages of using WAAM to fabricate parts include suboptimal surface quality, insufficient dimensional accuracy, and occasional high porosity due to violent melt pool interactions. Post processing including surface treatments is essential for WAAM fabricated components. Furthermore, compared to other DED processes, the relatively large heat source of the WAAM process often lead to higher residual stress and larger distortion in the as-build parts [69,70].

Other emerging additively manufacturing technologies: binder jetting additive manufacturing, first adapted from ink-jet sand-casting tools, has now matured into a true additively-manufacturing route for titanium components [71,72]. In this ambient-temperature process, a thin layer of powder is spread, micro-droplets of polymer binder are selectively deposited to create a “green” body, and the part is then de-powdered, de-bound, and vacuum-sintered (1250–1350 °C) or hot-isostatically pressed to reach functional density ($> 97\%$). Because no melting occurs, distortion is minimal, enabling fine heat-exchanger lattices and porous biomedical scaffolds that are hard for fusion-based AM. Commercially, Desktop Metal and GE Additive platforms have already produced flight-qualified Ti-6Al-4 V brackets for satellites and e-VTOL airframes, signaling that binder-jetted titanium is moving from laboratory to industrial reality [73].

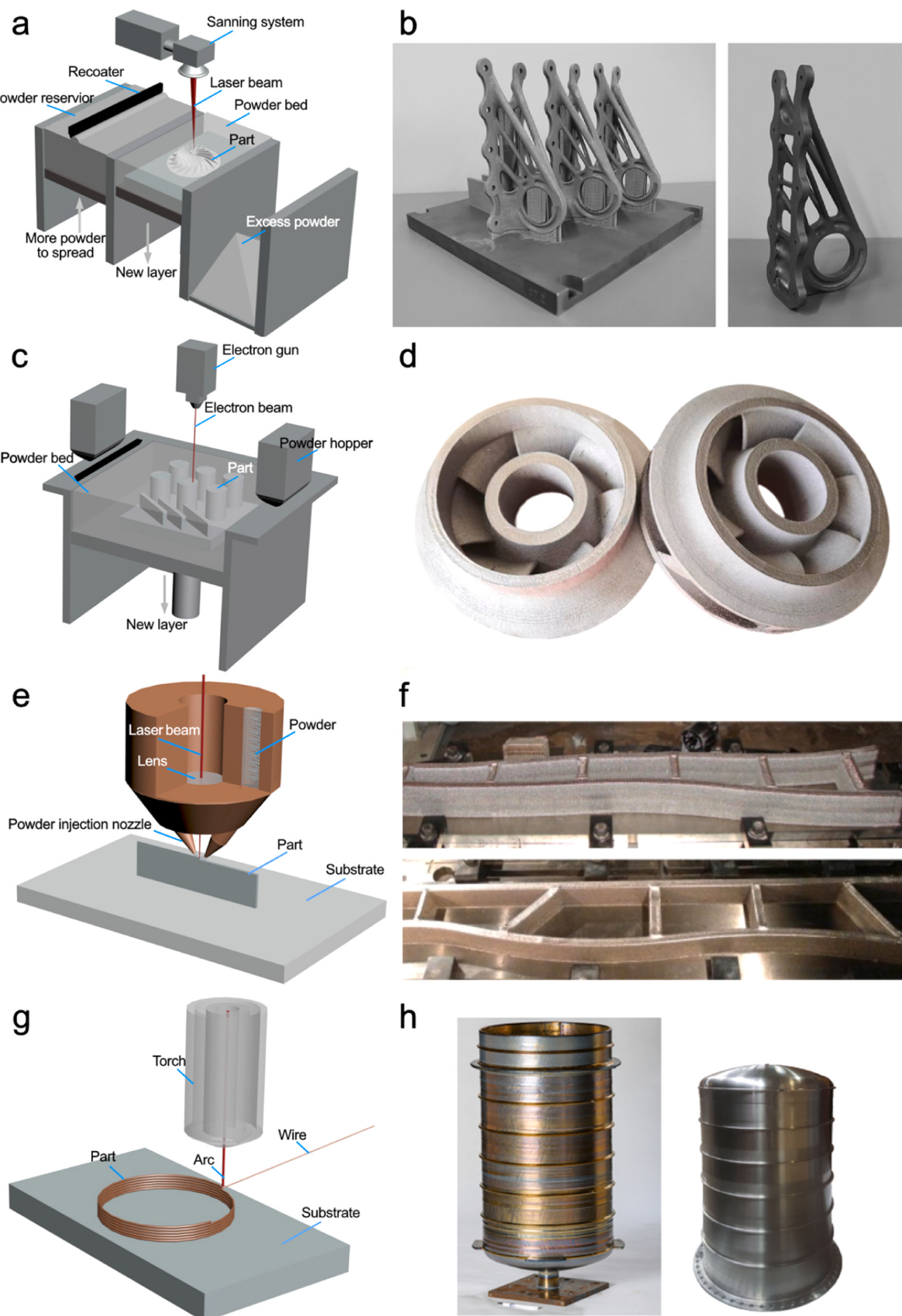


Fig. 1. (a) Schematic diagram showing the L-PBF set-up and fabrication process; (b) L-PBF Ti-6Al-4V brackets for Airbus A350 [54]; (c) Schematic diagram of EB-PBF; (d) EB-PBF titanium alloy liquid hydrogen pump impellers (diameter: ~ 20 cm) [17]; (e) Schematic diagram of L-DED; (f) L-DED titanium alloy spar (length: 1.1 m) [55]; (g) Schematic diagram of WAAM; (h) WAAM Ti-6Al-4V alloy pressure vessel for a space exploration task (height: ~1 m) [56].

3. Mechanical performance

3.1. Tensile properties

Quasi-static tensile performances provide basic material properties and are often used as a reference indicator for dynamic performance aspects [27]. Therefore, before examining the fatigue and damage tolerance characteristics of AM titanium alloys, we begin by summarizing their room-temperature tensile properties achieved so far. This assessment will encompass α titanium alloys, $\alpha+\beta$ titanium alloys, and β titanium alloys, examining their tensile properties both in the as-built condition and after post-AM heat treatment.

3.1.1. α titanium alloys

The tensile performance of α titanium alloys, including grade 2 commercially pure titanium (CP-Ti), Ti-6Al-2Zr-1Mo-1V (TA15), Ti-5Al-2.5Sn, Ti-6Al-2Sn-4Zr-2Mo (Ti-6242), and Ti-6Al-2Sn-4Zr-2Mo-0.1Si (Ti-6242S), processed by various AM technologies, is presented in Table 2 [74–81]. Among them, L-PBF α titanium alloys has been most widely investigated. In as-built state, a large variation of the tensile strength exists between different L-PBF α titanium alloys, with the lowest ultimate tensile strength (refers to UTS) of CP-Ti (~ 700 MPa) and the highest UTS of Ti-6242S (> 1500 MPa) [74,81]. In contrast, the total elongation (EL) of most L-PBF α titanium alloys in as-built state is relatively consistent, typically less than 10 %. One exception is CP-Ti, with the EL greater than 20 % [74,82]. On this basis, various post-AM treatments have been developed to further tune the tensile performances of L-PBF α titanium alloys. After annealing in the range of 490–890 °C, the ductility of L-PBF CP-Ti slight increase (within 3 %), while its strength continuously decrease with the rise in HT temperature [83]. In comparison, the UTS of L-PBF Ti-6242 can be improved from 1381 MPa in the as-built state to 1438 MPa through direct aging [77]. This is one of the few works that enhance strength of L-PBF α titanium alloys through heat treatment, even though it is accompanied by a significant decrease in ductility (failure before yield in L-PBF Ti-6242). With more optimized heat treatments, including commonly used solution and aging treatments and novel cyclic heating approach, L-PBF α titanium alloys could exhibit the better combination of strength and ductility (Table 2) [78,81,84,85]. For example, after cyclic heat treating between 960 and 860 °C for 140 min, the total elongation of L-PBF Ti-6242 can be significantly improved to ≥ 15 %, with the yield stress values of ≥ 1000 MPa [78]. Furthermore, a strong tensile property anisotropy in the L-PBF α titanium alloys is also evident both in the as-built and post-AM treatment states (Table 2). For instance, in L-PBF CP-Ti, there is a difference in EL over 2 % between the transverse (10.4 ± 2.6 %) and longitudinal (8.3 ± 1.6 %) directions in the as-built state [74]. After post-AM HIP treatment, such difference in ductility between the two directions is further increased to 7.8 % [74].

For α titanium alloys produced using AM approaches other than L-PBF, limited studies have focused on CP-Ti, Ti-6Al-2Zr-1Mo-1V, and Ti-6Al-2Sn-4Zr-2Mo [80,83,86,88,90], while their mechanical performances are generally unremarkable. Specifically, Ti-6Al-2Zr-1Mo-1V processed by L-DED exhibits a yield strength of ~ 940 MPa, lower than that of same alloy fabricated by L-PBF (with the YS of ~ 1000 MPa) [88]. Ti-6Al-2Zr-1Mo-1V fabricated by WAAM also shows moderate tensile strength (YS = 822 MPa) and poor ductility (EL = 3.5 %) [83]. EB-PBF Ti-6Al-2Sn-4Zr-2Mo possess the UTS of ~ 1100 MPa in the as-built state, which is also significantly lower than that of Ti-6Al-2Sn-4Zr-2Mo processed by L-PBF (with the UTS of > 1290 MPa) [80,90].

3.1.2. $\alpha+\beta$ titanium alloys

Numerous efforts have been made to investigate the quasi-static tensile performance of AM dual-phase titanium alloys, particularly Ti-6Al-4V, as shown in Table 3. Among these AM technique, L-PBF Ti-6Al-4V exhibits relatively higher UTS (> 1100 MPa in the as-built

state) [12,91]. In comparison, due to the lower cooling rates that lead to relatively coarser microstructures, Ti-6Al-4V fabricated by DED-based techniques (including L-DED and WAAM processes) shows relatively low UTS that is commonly lower than 1050 MPa in the as-built state (Table 3) [92]. Despite these general trends, the large number of published results show that tensile properties of AM Ti-6Al-4V in as-built state, even when processed using the same AM approach, can exhibit substantial variability. For instance, the total elongations of L-PBF Ti-6Al-4V varied from 4 % to 13 % with different printing parameters or L-PBF machine, while the tensile stress ranges from 1150 to 1250 MPa [22,93–95]. More specifically, with the layer thickness increases from 30 μm to 60 μm and the scan rotation angle changes from 90° to 67°, the ductility of L-PBF Ti-6Al-4V change from 7.8 % to 12.8 % [22]. These variations in the tensile performance are largely attributed to the inconsistent microstructures in AM $\alpha+\beta$ titanium alloys, along with the unpredictability of defects, which will be further discussed in Sections 4–5 [22,67,92–104].

Various post-AM treatment processes have been applied to AM Ti-6Al-4V alloy to optimize the tensile properties. Directly annealing treatments at a two-phase regime with a temperature ranging from 600 to 950 °C are normally used, aiming for the relief of residual stress and microstructure homogenization. This type of HT process mostly leads to the increase of the tensile ductility with the cost of UTS, as shown by the summarized results in Table 3. For example, the total elongation of L-PBF Ti-6Al-4V increases to 19 % upon annealing at 800 °C for 6 h (the ductility of the as-built state is 9 %) [91,118]. In addition, solution treatment and aging treatment is another typical method to obtain a good combination of strength and ductility in L-DED or WAAM Ti-6Al-4V (for instance, tensile ductility of WAAM Ti-6Al-4V can be enhanced to 16 % with a UTS of ≥ 850 MPa with 930 °C/1 h + 800 °C/2 h) [67,119]. Solution treatment temperatures can be above or below the β -transus, whereas aging temperatures typically fall within the range of 400–750 °C. Furthermore, post-AM HIP treatments can be performed below or above the β -transus [95,107,55,120]. With appropriate post-LPBF HIP treatments, the total elongation of AM Ti-6Al-4V can be improved to 15–20 %, while maintaining a YS of ≥ 850 MPa, as shown in Table 3.

In the meantime, anisotropic tensile properties have been identified in most L-DED and WAAM Ti-6Al-4V, while they have been less obvious in the Ti-6Al-4V processed by both L-PBF and EB-PBF. For example, the ductility of L-DED Ti-6Al-4V in the transverse orientation is only half of that in the building direction, even though the strength differences are insignificant [55]. However, the total elongation of the transverse samples is not always lower than that of the longitudinal samples [101,121]. This variation depends on the printing parameter (like scanning strategy and laser power), the built part geometry, and the location of the test specimens. For instance, the study that focused on the WAAM Ti-6Al-4V found that the parallel scanning strategy built sample show significant ductility between the longitudinal (EL = 24.3 %) and transverse (EL = 14.7 %) specimens, while specimens built with oscillation scanning strategy exhibit nearly consistent elongation in both directions [110].

Besides fusion-based AM technologies, the tensile performances of Ti-6Al-4V produced by novel binder jetting AM have also been studied recently [111]. In the as-built state, binder jetting AM Ti-6Al-4V shows the relatively low strength (YS = 790 MPa) and acceptable ductility (9.3 %). After HIP treatment, the yield stress can be increased to approximately 1000 MPa without compromising ductility (~ 10 %). These values are comparable to those reported for certain L-PBF Ti-6Al-4V subjected to similar HIP [95], underscoring the potential of binder jet AM for Ti alloys.

Along with Ti-6Al-4V, other $\alpha+\beta$ titanium alloys processed by AM were also investigated, including Ti-6.5Al-3.5Mo-1.5Zr-0.3Si, Ti-6Al-2Mo-2Sn-2Zr-2Cr-2V, and Ti-6Al-3Mo-2Sn-2Zr-2Cr, which show comparable tensile performance with AM Ti-6Al-4V (Table 3). For instance, L-PBF Ti-6.5Al-3.5Mo-1.5Zr-0.3Si exhibits a tensile strength of

Table 2Tensile properties of AM α titanium alloys.

Material	Method	State (i.e. treatments and testing directions)	Yield Stress (SD, MPa)	Ultimate Tensile Stress (SD, MPa)	Total Elongation (SD, %)	Ref.
CP-Ti	L-PBF	As-built, transverse	722	742	22.2	[83]
		650 °C/1 h/AC, transverse	667	742	25.2	
		750 °C/1 h/AC, transverse	640	727	25.7	
		850 °C/1 h/AC, transverse	574	659	25.4	
CP-Ti	L-PBF	As-built, transverse	521 (13)	607 (17)	10.4 (2.6)	[74]
		As-built, longitudinal	630 (22)	720 (23)	8.3 (1.6)	
		HIP (730 °C/101 MPa/1 h), transverse	512 (14)	587 (22)	7.3 (1.3)	
		HIP (730 °C/101 MPa/1 h), longitudinal	622 (10)	716 (13)	15.1 (3.1)	
		HIP (950 °C/101 MPa/1 h), transverse	482 (13)	573 (27)	6.3 (1.3)	
		HIP (950 °C/101 MPa/1 h), longitudinal	573 (33)	662 (39)	7.4 (2.2)	
CP-Ti	L-PBF	As-built, longitudinal	620	717	20.2	[82]
		490 °C/2 h/FC, longitudinal	615	685	20.9	
		590 °C/2 h/FC, longitudinal	570	645	21.8	
		690 °C/2 h/FC, longitudinal	575	643	21.1	
		790 °C/2 h/FC, longitudinal	586	638	21.4	
		890 °C/2 h/FC, longitudinal	490	603	22.5	
CP-Ti	EB-PBF	As-built, longitudinal	616	688	18.1	[86]
		Cyclic heat treating between 25 and 1000 °C for 1 time, longitudinal	566	641	17.1	
		Cyclic heat treating between 25 and 1000 °C for 3 times, longitudinal	528	631	18.2	
		Cyclic heat treating between 25 and 1000 °C for 5 times, longitudinal	494	630	16.2	
		As-built, transverse	1048	1214	9.2	[75]
Ti-6Al-2Zr-1Mo-1V	L-PBF	As-built, longitudinal	1088	1234	8.4	
		800 °C/1 h/AC, transverse	980	1058	13.5	
		800 °C/1 h/AC, longitudinal	1005	1064	14.4	
		800 °C/4 h/AC, transverse	966	980	13.8	
		800 °C/4 h/AC, longitudinal	988	1008	14.5	
		As-built, transverse	-	1234 (53)	7.3 (0.7)	[87]
		650 °C/2 h/FC, transverse	-	1207 (4)	8.9 (0.1)	
		750 °C/2 h/FC, transverse	-	1124 (14)	11.3 (0.7)	
Ti-6Al-2Zr-1Mo-1V	L-PBF	850 °C/2 h/FC, transverse	-	1025 (20)	9.0 (0.4)	
		950 °C/2 h/FC, transverse	-	937 (5)	8.0 (1.0)	
		1000 °C/2 h/FC, transverse	-	907 (5)	5.8 (0.2)	
		1100 °C/2 h/FC, transverse	-	780 (7)	3.8 (0.4)	
		As-built, longitudinal	1123	1281	8.1	[84]
		800 °C/2 h/AC, longitudinal	993	1077	14.4	
		970 °C/1.5 h/AC + 600 °C/3 h/AC, longitudinal	917	1012	15.7	
		970 °C/1.5 h/AC + 750 °C/3 h/AC, longitudinal	868	964	16.7	
Ti-6Al-2Zr-1Mo-1V	L-PBF	970 °C/1.5 h/AC + 850 °C/3 h/AC, longitudinal	834	981	16.1	
		970 °C/1.5 h/AC + 930 °C/3 h/AC, longitudinal	838	1001	14.0	
		970 °C/1.5 h/AC + 930 °C/3 h/AC + 600 °C/4 h/AC, longitudinal	934	1019	16.3	
		As-built, transverse	937 (6)	1004 (7)	8.6 (1.0)	[88]
		As-built, longitudinal	900 (8)	987 (9)	15.3 (1.9)	
		As-built, transverse	822	942	3.5	[83]
		As-built, transverse	1077	1173	7.7	[76]
		As-built, longitudinal	1064	1169	8.2	
		600 °C/2 h/FC, transverse	1043	1142	9.4	
		600 °C/2 h/FC, longitudinal	1044	1166	9.4	
Ti-5Al-2.5Sn	L-PBF	650 °C/2 h/FC, transverse	987	1095	10.5	
		650 °C/2 h/FC, longitudinal	1016	1104	10.6	
		750 °C/2 h/FC, transverse	956	1064	11.5	
		750 °C/2 h/FC, longitudinal	977	1070	12	
		850 °C/2 h/FC, transverse	808	894	15.2	
		850 °C/2 h/FC, longitudinal	832	926	14.4	
		As-built, longitudinal	1030 (20)	1080 (25)	13.2 (0.2)	[89]
		850 °C/2 h/FC, longitudinal	900 (14)	920 (30)	16.1 (0.1)	
Ti-6Al-2Sn-4Zr-2Mo	L-PBF	850 °C/4 h/FC, longitudinal	895 (5)	905 (10)	17.8 (0.2)	
		HIP (850 °C/120 MPa/2 h), longitudinal	895 (15)	910 (8)	15.1 (0.2)	
		As-built, transverse	1293 (37)	1381 (79)	5.3	[77]
		595 °C/8 h/AC, transverse	Failure before yield	1438 (103)	1.4	
Ti-6Al-2Sn-4Zr-2Mo	L-PBF	As-built, transverse	1296 (44)	1437 (13)	5.7 (1.1)	[78]
		630 °C/8 h/AC, transverse	1318 (2)	1402 (23)	4.6 (0.6)	
		850 °C/3 h/AC, transverse	1110 (8)	1185 (4)	9.3 (1.2)	
		955 °C/1 h/AC+ 595 °C/8 h/AC, transverse	1068 (3)	1162 (7)	15.0 (0.9)	
		Cyclic heat treating between 960 and 860 °C for 140 min, transverse	1019 (17)	1157 (20)	16.5 (1.3)	
		As-built, transverse	1293 (37)	1293 (37)	5.3	[85]
Ti-6Al-2Sn-4Zr-2Mo	L-PBF	650 °C/6 h/WQ + 598 °C/8 h/AC, transverse	1393	1405	1.8	
		750 °C/2 h/WQ + 598 °C/8 h/AC, transverse	1233 (20)	1250 (11)	1.6	

(continued on next page)

Table 2 (continued)

Material	Method	State (i.e. treatments and testing directions)	Yield Stress (SD, MPa)	Ultimate Tensile Stress (SD, MPa)	Total Elongation (SD, %)	Ref.
Ti-6Al-2Sn-4Zr-2Mo	EB-PBF	800 °C/1 h/WQ + 598 °C/8 h/AC, transverse	1253 (17)	1259 (22)	1.8	[80]
Ti-6Al-2Sn-4Zr-2Mo	EB-PBF	850 °C/0.5 h/WQ + 598 °C/8 h/AC, transverse	Failure before yield	1172 (4)	1.4	[90]
Ti-6Al-2Sn-4Zr-2Mo-0.1Si	L-PBF	1025 °C/1 h/WQ + 598 °C/8 h/AC, transverse	Failure before yield	697 (47)	< 1	[81]
Ti-6Al-2Sn-4Zr-2Mo-0.1Si	L-PBF	As-built, longitudinal	853 (10)	914 (8)	7.9 (0.9)	[80]
		As-built	1018 (14)	1115 (18)	7.8 (0.1)	[90]
		HIP (850 °C/103 MPa/2 h)	937 (19)	1048 (7)	16.4 (0.1)	
		HIP (950 °C/103 MPa/2 h)	887 (21)	1000 (4)	16.2 (0.1)	
		HIP (1050 °C/103 MPa/2 h)	836 (8)	963 (6)	12.2 (0.1)	
Ti-6Al-2Sn-4Zr-2Mo-0.1Si	L-PBF	As-built	1406 (17)	1526 (6)	4.3 (0.8)	[81]
		700 °C/1 h/AC + 600 °C/24 h/AC	1390 (2)	1421 (5)	0.9 (0.3)	
		800 °C/1 h/AC + 600 °C/24 h/AC	1172	1263	6.5	
		900 °C/1 h/AC + 600 °C/24 h/AC	1075 (4)	1155 (7)	16.0 (0.1)	
Ti-6Al-2Sn-4Zr-2Mo-0.1Si	L-PBF	As-built	1296	1420	9.0	[85]
		900 °C/10 min/WQ	883	1102	17.5	
		900 °C/10 min/WQ + 300 °C/48 h	1055	1147	14.7	

1107 MPa with ductility of 12.3 % (the UTS and elongation of L-PBF Ti-6Al-4V are 1202 MPa and 10.1 %, respectively) [22,112]. Post-AM heat treatment has also been applied to such alloys to achieve the desirable tensile performances. The study of L-DED Ti-6Al-2Mo-2Sn-2Zr-2Cr-2V alloy reveals that solution treatment and aging can simultaneously enhance both strength and ductility (the UTS increases from 1025 MPa to 1170 MPa and the elongation rises from 6.0 % to 7.8 % after 900 °C/2 h + 540 °C/4 h) [116]. Furthermore, in these limited works, these $\alpha+\beta$ titanium alloys processed by AM also exhibit strong ductility anisotropy in both as-built and heat-treated states. In particular, the ductility of as-built Ti-6.5Al-3.5Mo-1.5Zr-0.3Si processed by L-DED is 18.8 % in the longitudinal direction, while it is only 8.2 % in the transverse direction [113].

3.1.3. β titanium alloys

Compared with the most widely explored AM $\alpha+\beta$ titanium alloy Ti-6Al-4V, fewer attempts have been made to explore the tensile performance of the AM β titanium alloys. Current research efforts are mainly focused on Ti-6Al-2Sn-4Zr-6Mo (Ti-6246), Ti-5Al-2Sn-2Zr-4Mo-4Cr (Ti-17), Ti-5Al-5Mo-5V-1Cr-1Fe (Ti-55511), Ti-5Al-5Mo-5V-3Cr-1Zr (Ti-55531) alloy, Ti-5Al-5V-5Mo-3Cr (Ti-5553), and Ti-3Al-8V-6Cr-4Mo-4Zr (Beta-C). As shown in Table 4, most AM β titanium alloys in the as-built state exhibit the UTS below 1000 MPa, while maintaining the superior ductile of ≥ 15 %. This is primarily related to the presence of soft phases in the as-built condition, which will be discussed in 5.

Post-AM heat treatments can greatly modify the tensile properties of AM β titanium alloys, and more specifically their tensile strength, as shown in Table 4. Solution treatment, whether above or below the β transus temperatures, along with aging, can significantly enhances the strength (both YS and UTS) of AM β titanium alloys, which can greatly exceed that of the AM Ti-6Al-4V [122,141,130,142,134,137]. The ultimate tensile stress of L-DED Ti-55531, treated by β solution treatment and aging, reached 1352 MPa with the total elongation retained as 5.9 % [130]. Upon direct aging of L-PBF Beta-C, over 1600 MPa tensile strength (refers to UTS) and ~ 5 % uniform elongation can be achieved, which is the highest strength of all AM titanium alloys reported to date [138]. However, the solution + aging treatments and direct aging normally lead to lower ductility of AM β titanium alloys, for instance, L-PBF Ti-55531 exhibits a limited ductility of less than 2 % after solution + aging treatments [129]. To this end, triplex anneal treatment (β solution treatment, α/β solution treatment, and aging) in the L-DED Ti-55531 was developed to improve ductility (total elongation increased from 5.9 % in solution + aging sample to 8.5 %) [130]. Other research on L-PBF Ti-55511 [132] and L-PBF Ti-17 [136] have been shown that increasing the aging temperature can achieve comparatively better elongation (improvement from brittle failure before yielding (450 °C aging) to ~ 8 % elongation (650 °C aging)). Furthermore, pre-heat

treatment (prior to annealing) L-DED Ti-55511 at 900 °C followed by furnace cooling from the β phase field also achieved the ~ 1100 MPa UTS and ~ 12 % elongation [135]. For AM β titanium alloys with relatively less β -stabilizing elements, like Ti-6Al-2Sn-4Zr-6Mo, annealing in the ranges of 600 – 900 °C was normally performed to induce the α'' martensite decomposition into α -phase and β -phase (more details can be seen in 5), which results in high yield strength (from ~ 450 MPa to ~ 1050 MPa) with acceptable ductility (> 15 %) [140,143].

3.2. Fatigue properties

3.2.1. High-cycle fatigue

Since titanium alloys are mostly used for critical components like load-bearing components in aircraft and rotating components in aero engines, fatigue properties of AM titanium alloys is considered the most important mechanical properties to the end users [12]. Currently, most efforts have been made to understand the fatigue behavior of the AM Ti-6Al-4V, the most widely used titanium alloy. However, most of the published research found that the fatigue properties, especially high-cycle fatigue properties, of AM Ti-6Al-4V vary greatly, as shown in Fig. 2a [34,118,144–153]. For instance, L-PBF Ti-6Al-4V with optimal printing parameters and annealing process has two orders of magnitude differences in the fatigue life at the same stress level from different published works (Fig. 2a) [147,149]. Similarly, WAAM Ti-6Al-4V has two different fatigue limits from two different studies, one at 270 MPa and another one at 500 MPa, despite the fact that both Ti-6Al-4V are fabricated with optimal process parameters and annealed (Fig. 2a) [147,151]. These significant variations result in the lower bound of AM Ti-6Al-4V being inferior to that of conventionally cast products, while its best performance can match or even exceed that of conventionally wrought Ti-6Al-4V reported in the ASM handbook, as shown in Fig. 2a. Besides fusion-based AM technologies, the fatigue performances of Ti-6Al-4V produced by sinter-based AM (like binder jetting AM) are also explored [111]. However, the HCF performance of binder jetting AM Ti-6Al-4V remains unsatisfactory, even after HIP treatment, with the fatigue strength of less than 200 MPa. This is significantly lower than the high-cycle fatigue strength of fusion-based AM and conventionally manufactured Ti-6Al-4V. This may be related to the higher porosity (> 4 %) and elevated interstitials resulting from binder decomposition. Furthermore, compared to the significant anisotropic tensile performance, there is no obvious trend in the anisotropic HCF performance of AM Ti-6Al-4V alloy (Fig. 2b). Some studies found that the HCF performance of the transverse specimen was superior to that of the longitudinal specimen [154–157], while other studies have reported the opposite results [158–161]. This is considered to be related to the presence of printing pores and large columnar grain, which will be further discussed in Sections 4–5 [154,162].

Table 3Tensile properties of AM $\alpha+\beta$ titanium alloys.

Material	Method	State (i.e. treatments and testing directions)	Yield Stress (SD, MPa)	Ultimate Tensile Stress (SD, MPa)	Total Elongation (SD, %)	Ref.
Ti-6Al-4V	L-PBF	As-built, transverse	946 (10)	1151 (9)	4.4 (0.7)	[94]
Ti-6Al-4V	L-PBF	As-built (30 μm layer thickness and the 90° scan rotation), transverse	1121 (42)	1186 (42)	7.8 (0.6)	[22]
		As-built (30 μm layer thickness and the 90° scan rotation), longitudinal	1161 (30)	1237 (30)	7.6 (1.0)	
		As-built (30 μm layer thickness and the 67° scan rotation), transverse	1121 (9)	1202 (11)	10.1 (0.3)	
		As-built (30 μm layer thickness and the 67° scan rotation), longitudinal	1121 (42)	1186 (42)	8.1 (0.6)	
		As-built (60 μm layer thickness and the 90° scan rotation), transverse	1115 (18)	1183 (22)	9.7 (0.3)	
		As-built (60 μm layer thickness and the 90° scan rotation), longitudinal	1151 (11)	1222 (25)	9.8 (1.1)	
		As-built (60 μm layer thickness and the 67° scan rotation), transverse	1063 (19)	1137 (23)	12.8 (0.9)	
		As-built (60 μm layer thickness and the 67° scan rotation), longitudinal	1102 (16)	1145 (14)	12.8 (0.9)	
Ti-6Al-4V	L-PBF	As-built, transverse	1080 (20)	1220 (20)	5.5 (2)	[95]
		As-built, longitudinal	1060 (15)	1180 (13)	7.8 (1)	
		Stress relieved, HIP (920 °C/103 MPa/4 h), transverse	980 (22)	1040 (20)	12.0 (1)	
		Stress relieved, HIP (920 °C/103 MPa/4 h), longitudinal	850 (2)	980 (2)	16.0 (3)	
Ti-6Al-4V	L-PBF	As-built, transverse	1075 (25)	1199 (49)	7.6 (0.5)	[105]
		As-built, longitudinal	978 (5)	1143 (6)	11.8 (0.5)	
		730 °C/2 h, transverse	974 (7)	1065 (21)	7.0 (0.5)	
		730 °C/2 h, longitudinal	958 (6)	1057 (8)	12.4 (0.7)	
Ti-6Al-4V	L-PBF	As-built, transverse	1040	1201	9.5	[91]
		700 °C/2 h/FC, transverse	1011	1109	13.4	
		800 °C/2 h/FC, transverse	953	1050	14.7	
		800 °C/6 h/FC, transverse	937	1040	18.8	
		800 °C/12 h/FC, transverse	929	1031	18.5	
Ti-6Al-4V	EB-PBF	As-built, transverse	1049 (14)	1195 (17)	8.9 (0.7)	[106]
		As-built, longitudinal	1045 (17)	1187 (20)	11.1 (0.7)	
Ti-6Al-4V	EB-PBF	As-built, transverse	881 (12)	979 (12)	10.7 (1.5)	[107]
Ti-6Al-4V	EB-PBF	HIP (900 °C/103 MPa/4 h), transverse	876 (12)	978 (9.5)	13.5 (1.5)	
		1100 °C/0.5 h/FC, longitudinal	774 (112)	913 (38)	13.0 (2.0)	[108]
		1100 °C/0.5 h/AC, longitudinal	847 (90)	998 (52)	13.0 (7.0)	
		1100 °C/0.5 h/WQ, longitudinal	932 (80)	1200 (50)	1.8 (1.5)	
Ti-6Al-4V	L-DED	As-built, transverse	950 (2)	1025 (2)	5.0 (1.0)	[55]
		As-built, longitudinal	950 (2)	1025 (10)	12.0 (1.0)	
		HIP (920 °C/100 MPa/4 h), longitudinal	850 (2)	920 (1)	17.0 (2.0)	
Ti-6Al-4V	L-DED	As-built, transverse	945 (53)	1037 (46)	10.5 (0.3)	[101]
		As-built, longitudinal	950 (10)	1056 (19)	10.8 (0.5)	
Ti-6Al-4V	L-DED	As-built, transverse	960 (26)	1063 (20)	13.3 (1.8)	[100]
		As-built, longitudinal lower	970 (17)	1087 (8)	17.6 (0.7)	
		As-built, longitudinal upper	945 (13)	1041 (12)	18.7 (1.7)	
Ti-6Al-4V	L-DED	As-built, transverse	841 (0.3)	922 (2)	14.1 (0.5)	[109]
		As-built, longitudinal	770 (48)	824 (56)	17.7 (2.2)	
Ti-6Al-4V	L-DED	700 °C/2 h, transverse	923 (11)	975 (19)	13.2 (0.6)	[99]
		700 °C/2 h, longitudinal	788 (55)	881 (50)	27.8 (1.9)	
Ti-6Al-4V	WAAM	As-built (bidirectional), transverse	700 (13)	820 (30)	10.4 (2.6)	[92]
		As-built (unidirectional), transverse	710 (8)	830 (15)	15.5 (2.0)	
		As-built (unidirectional), transverse	755 (3)	853 (10)	12.6 (1.8)	
Ti-6Al-4V	WAAM	As-built, transverse	746 (17)	847 (10)	12.2 (2.8)	[67]
		600 °C/4 h, transverse	772 (12)	845 (15)	11.8 (0.9)	
		850 °C/2 h, transverse	734 (25)	845 (18)	13.6 (2.8)	
		930 °C/1 h (slow cooling), 550 °C/4 h, transverse	783 (11)	865 (8)	9.9 (0.9)	
Ti-6Al-4V	WAAM	930 °C/1 h (fast cooling), 550 °C/4 h, transverse	951 (25)	1034 (18)	7.5 (0.9)	
		930 °C/1 h (fast cooling), 800 °C/2 h, transverse	771 (9)	886 (8)	16.6 (1.6)	
		As-built (parallel scanning strategy), transverse	-	1131	14.7	[110]
		As-built (parallel scanning strategy), longitudinal	-	1013	24.3	
		As-built (oscillation scanning strategy), transverse	-	1309	11.6	
		As-built (oscillation scanning strategy), longitudinal	-	1322	12.8	
Ti-6Al-4V	Binder jet AM	As-built	790	912	9.3	[111]
		HIP (920 °C/100 MPa/4 h)	1002	1089	10.5	
		HIP (920 °C/100 MPa/4 h)	974	1043	9.2	
Ti-6.5Al–3.5Mo–1.5Zr–0.3Si	L-PBF	As-built, transverse	1011	1107	12.3	[112]
Ti-6.5Al–3.5Mo–1.5Zr–0.3Si	L-DED	As-built, transverse	920	1025	8.2	[113]
		As-built, longitudinal	840	925	18.8	

(continued on next page)

Table 3 (continued)

Material	Method	State (i.e. treatments and testing directions)	Yield Stress (SD, MPa)	Ultimate Tensile Stress (SD, MPa)	Total Elongation (SD, %)	Ref.
Ti-6.5Al-3.5Mo-1.5Zr-0.3Si 1018	L-DED	530 °C/6 h, transverse	1001	1089	9.9	[114]
		530 °C/6 h, longitudinal	932	1018	14.7	
		1000 °C/1 h+530 °C/6 h, transverse	971	1099	11.8	
		1000 °C/1 h+530 °C/6 h, longitudinal	895	1033	16.8	
		1000 °C/1 h, transverse	895	1059	9.0	
	WAAM	1000 °C/1 h, longitudinal	915	1038	10.0	
		550 °C/4 h/AC, transverse	970	1044	10.3	[115]
		550 °C/4 h/AC, longitudinal	905	969	18.1	
		970 °C/2 h/AC + 550 °C/4 h/AC, transverse	896	999	17.3	
		970 °C/2 h/AC + 550 °C/4 h/AC, longitudinal	861	970	21.6	
Ti-6.5Al-3.5Mo-1.5Zr-0.3Si	WAAM	990 °C/2 h/AC + 550 °C/4 h/AC, transverse	900	1012	16.2	
		990 °C/2 h/AC + 550 °C/4 h/AC, longitudinal	851	967	19.2	
		1020 °C/2 h/AC + 550 °C/4 h/AC, transverse	872	987	13.5	
		1020 °C/2 h/AC + 550 °C/4 h/AC, longitudinal	852	948	16.5	
		As-built, transverse	943	1025	6.0	[116]
		900 °C/2 h/AC + 540 °C/4 h/AC, transverse	1035	1170	7.8	
		920 °C/2 h/AC + 540 °C/4 h/AC, transverse	1074	1196	7.2	
		940 °C/2 h/AC + 540 °C/4 h/AC, transverse	1083	1201	6.2	
		920 °C/2 h/AC + 540 °C/4 h/AC, transverse	1026 (13)	1187 (12)	3.3 (1.7)	[117]
		920 °C/2 h/AC + 540 °C/4 h/AC, longitudinal	1017 (18)	1166 (16)	13.2 (4.8)	

The hot isostatic pressing (HIP) process, which is introduced as an effective post-AM treatment approach for closing detrimental pores like lack-of-fusion (LOF) and gas porosity, is very beneficial in improving the high-cycle fatigue performance, [144,148,150,153]. The samples after the HIP process showed better high-cycle fatigue properties than those in wrought Ti-6Al-4V, with significantly improved consistency as compared with those before HIP. For instance, after HIP treatment at 920 °C/2 h/100 MPa, the fatigue strength of EB-PBF Ti-6Al-4V can be increased from ~ 350 MPa in the as-built state to ~ 550 MPa [168]. Very recently, HIP combined with post-AM heat treatment has been developed (named the Net-AM post-processing technique), which achieves a fatigue limit of around 1000 MPa (the corresponding specific fatigue strength exceeds 200 MPa·g⁻¹·cm³) in L-PBF Ti-6Al-4V [39, 169]. This is the best HCF performance in titanium alloys (Fig. 2a), and even the highest specific fatigue limit among all metallic materials.

Besides the well-investigated high-cycle fatigue properties of AM Ti-6Al-4V, other research efforts into the fatigue properties of other AM titanium alloys produced by various AM technologies have been published, as shown in Fig. 3. L-DED processed Ti-6.5Al-3.5Mo-1.5Zr-0.3Si (a $\alpha+\beta$ titanium alloy), Ti-6Al-2Zr-Mo-V (a high-temperature α titanium alloy), and Ti-6Al-2Mo-2Sn-2Zr-2Cr-2V (a new type of $\alpha+\beta$ titanium alloy with more β stabilizer) show comparable fatigue performances with L-DED Ti-6Al-4V in the stress ratio of 0.06 [170–176]. In recent studies, L-DED Ti-6.5Al-3.5Mo-1.5Zr-0.3Si has been shown to match the high-cycle fatigue performance of its wrought counterpart at a stress ratio of 0.5 [177,178]. In comparison, L-PBF processed titanium alloys other than Ti-6Al-4V, including Ti-6Al-2Sn-4Zr-2Mo [179], Ti-5V-5Mo-5Al-3Cr [180], CP-Ti [181], Ti-6Al-2Zr-Mo-V [182], and Ti-6Al-7Nb [183], show the lower HCF performance (the HCF data at a stress ratio of -1 are presented in Fig. 3b). In particular, even after stress-relief treatment, L-PBF Ti-6Al-4Nb exhibits a fatigue strength of less than 200 MPa [183]. In the meantime, it is found that large variations of HCF data also still exist in these titanium alloys even after post-AM heat treatments. Moreover, very recently, β titanium alloys processed by EB-PBF, including Ti-5Al-5Mo-5V-1Cr-1Fe and Ti-5V-5Mo-5Al-3Cr, were also studied, as shown in Fig. 3c [180,184, 185]. It is found that post-AM HIP can significantly enhance the fatigue performance of EB-PBF Ti-5Al-5Mo-5V-1Cr-1Fe (fatigue limit increase from 300 MPa to 450 MPa), while also reducing the variations of HCF results [185]. These findings highlight that HIP is also an effective post-AM processing method for AM β titanium alloys, capable of eliminating the printing pores and improving the HCF performance. However, as compared to conventionally manufactured Ti-5Al-5Mo-5V-1Cr-1Fe (generally higher than 700 MPa [186]), the

fatigue strength of AM Ti-5Al-5Mo-5V-1Cr-1Fe is still limited, even after post-AM HIP. Similarly, WAAM Ti-5Al-2Sn-2Zr-4Mo-4Cr (Ti-17, a typical β titanium alloy) exhibits HCF performance that is also markedly inferior to that of its conventionally forged counterpart (whose values exceed 600 MPa), as shown in Fig. 3d [187]. This also suggests that further efforts are needed to develop the fatigue performance of AM β titanium alloy.

It should be mentioned that all the above-reported HCF results were obtained from specimens whose as-built surfaces had been removed by machining, however, surface defects also influence the HCF performance of AM titanium alloys. Fig. 4a illustrates the HCF life of Ti-6Al-4V processed by several AM technologies before and after mechanical processing, revealing significant differences. For example, the fatigue limit of EB-PBF Ti-6Al-4V was approximately 150 MPa before machining, while after machining, this value increased to ~ 400 MPa [166]. The same trend extends beyond the work-horse Ti-6Al-4 V alloy. As shown in Fig. 4b, LPBF Ti-5V-5Mo-5Al-3Cr gains nearly 200 MPa in fatigue strength after machining [192]. These results suggest that the rough surface of the as-built part has a significant negative effect on the fatigue performance of AM titanium alloys. To this end, various surface treatments have been applied to AM titanium alloys to improve HCF performance [29,193–196]. For instance, by closing surface defects and introducing compressive residual stresses on the sample surface, shot peening can further enhance the fatigue life of L-DED Ti-6Al-2Zr-Mo-V from 2.4×10^4 cycles after machining to 7.2×10^4 cycles at a stress level of 720 MPa, representing a relative improvement of approximately 200 % [193]. Another example is that electrochemical polishing can reduce the surface roughness (R_a) of L-PBF Ti-6Al-4V from ~ 11 μm in the un-machined state to less than 1 μm , and this refinement is mirrored by a jump in fatigue strength from about 400 MPa to nearly 750 MPa [194]. Taken together, these literatures underscore that surface condition is a critical determinant of the high-cycle fatigue performance of additively manufactured titanium alloys.

3.2.2. Fatigue crack propagation

Damage tolerance is another important design parameter for aircraft, which is used to represent the capacity of a material to sustain the fracture with the cracks initiated. Damage tolerance performance mainly includes fatigue crack propagation (FCG) property and fracture toughness. To date, most efforts have been made to investigate the damage tolerance performance of AM Ti-6Al-4V. In the as-built condition, L-PBF Ti-6Al-4V alloy generally shows the poor FCG resistance, with the FCG thresholds of 1.5–1.8 MPa $\sqrt{\text{m}}$ [198]. After post-AM heat treatment, the FCG resistance of L-PBF Ti-6Al-4V alloy can be improved,

Table 4Tensile properties of AM β titanium alloys.

Material	Method	State (i.e. treatments and testing directions)	Yield Stress (SD, MPa)	Ultimate Tensile Stress (SD, MPa)	Total Elongation (SD, %)	Ref.
Ti-12Mo-6Zr-2Fe	L-PBF	As-built (single scanned), transverse	Failure before yield	1291 (25)	1.3 (0.1)	[122]
		As-built (chess scanned), transverse	1025 (5)	1026 (5)	12.7 (1.0)	
Ti-5Al-5V-5Mo-3Cr	L-PBF	Chess-scanned, solution treated at 1000 °C, transverse	943 (8)	587 (21.6)	7.3 (1.3)	
		300 °C/1 h/FC, longitudinal	801 (14)	824 (13)	17.2 (1.5)	[123]
		400 °C/1 h/FC, longitudinal	1178	1190 (90)	1.9 (0.1)	
		500 °C/1 h/FC, longitudinal	1397	1397 (36)	1.4 (0.1)	
		600 °C/1 h/FC, longitudinal	1332 (32)	1371 (21)	3.5 (0.6)	
		700 °C/1 h/FC, longitudinal	996 (17)	1088 (11)	14.2 (4.0)	
Ti-5Al-5V-5Mo-3Cr	L-PBF	800 °C/1 h/FC, longitudinal	895 (39)	951 (23)	15.6 (4.5)	
		As-built, transverse	831 (7)	856 (6)	18.9 (0.9)	[124]
Ti-5Al-5V-5Mo-3Cr	L-DED	600 °C/0.5 h/WQ (with faster heating), longitudinal	1060 (5)	1345 (5)	11.6 (0.5)	[125]
		600 °C/0.5 h/WQ (with slower heating), longitudinal	1200 (6)	1380 (8)	4.2 (0.2)	
		300 °C/8 h + 600 °C/0.5 h/WQ, longitudinal	1200 (4)	1365 (4)	4.0 (0.3)	
Ti-5Al-5V-5Mo-3Cr	L-DED	900 °C/0.5 h/WQ + 600 °C/0.5 h/WQ, longitudinal	925 (4)	1150 (3)	8.2 (0.4)	
		As-built	-	800	14.0	[126]
Ti-5Al-5V-5Mo-3Cr	WAAM	As-built, longitudinal	1048 (11)	1065 (10)	21.0 (1.4)	[127]
		As-built, transverse	1036 (14)	1094 (1)	8.3 (3.2)	
Ti-5Al-5Mo-5V-3Cr-1Zr	L-PBF	As-built (200 °C substrate heating), transverse	801	816	16.9	[128]
		As-built (700 °C substrate heating), transverse	1200	1440	1.6	
Ti-5Al-5Mo-5V-3Cr-1Zr	L-PBF	As-built, longitudinal	804 (5)	819 (7)	16.5 (0.6)	[129]
		As-built, transverse	794 (6)	806 (3)	19.2 (1.5)	
		880 °C/1.5 h/AC + 600 °C/6 h/AC, longitudinal	Failure before yield	1412 (9)	-	
		880 °C/1.5 h/AC + 600 °C/6 h/AC, transverse	Failure before yield	1430 (13)	-	
		880 °C/1.5 h cooling to 750 °C/1.5 h/AC+ 600 °C/6 h/AC, longitudinal	1267 (3)	1329 (6)	8.0 (0.1)	
		880 °C/1.5 h cooling to 750 °C/1.5 h/AC+ 600 °C/6 h/AC, transverse	1278 (6)	1338 (11)	7.2 (0.5)	
		790 °C/1.5 h/AC + 600 °C/6 h/AC, longitudinal	1180 (9)	1234 (5)	25.0 (0.2)	
		790 °C/1.5 h/AC + 600 °C/6 h/AC, transverse	1255 (10)	1274 (6)	18.0 (0.1)	
		As-built, transverse upper	825 (8)	861 (12)	19.8 (0.1)	[130]
		As-built, transverse lower	865 (12)	912 (20)	16.4 (0.5)	
Ti-5Al-5Mo-5V-3Cr-1Zr	L-DED	As-built, longitudinal	822 (14)	866 (9)	17.2 (0.9)	
		880 °C/1 h/AC + 600 °C/4 h/AC, transverse upper	1186 (7)	1225 (11)	8.9 (0.4)	
		880 °C/1 h/AC + 600 °C/4 h/AC, transverse lower	1354 (7)	1365 (10)	5.9 (0.4)	
		880 °C/1 h/AC + 600 °C/4 h/AC, longitudinal	1347 (7)	1352 (9)	5.4 (0.9)	
		880 °C/1 h, furnace cooling to 790 °C/1.5 h/AC, 600 °C/4 h/AC, transverse upper	1192 (19)	1219 (17)	8.5 (0.3)	
		880 °C/1 h, furnace cooling to 790 °C/1.5 h/AC, 600 °C/4 h/AC, longitudinal	1172 (16)	1210 (10)	7.8 (0.4)	
		As-built, transverse	1070	1135	11.2	[131]
		As-built, transverse	853 (16)	889 (19)	19.4 (1.8)	[132]
		450 °C/2 h/WQ, transverse	Failure before yield	892 (25)	-	
		550 °C/2 h/WQ, transverse	Failure before yield	1325 (24)	-	
Ti-5Al-5Mo-5V-1Cr-1Fe	L-PBF	600 °C/2 h/WQ, transverse	Failure before yield	1495 (22)	-	
		650 °C/2 h/WQ, transverse	1334 (18)	1410 (20)	4.3 (0.6)	
		750 °C/2 h/WQ, transverse	1121 (11)	1143 (12)	8.2 (0.7)	
		750 °C/2 h/WQ + 600 °C/2 h/WQ, transverse	1235 (9)	1264 (19)	9.3 (0.7)	
		As-built, transverse	833 (8)	883 (4)	23.7 (1.7)	[133]
		As-built, longitudinal	868 (7)	875 (13)	17.3 (1.6)	
		As-built, 45° off the longitudinal	797 (10)	848 (12)	22.3 (1.7)	
		750 °C/2 h/WQ + 600 °C/2 h/WQ, transverse	1110 (10)	1146 (14)	13.3 (2.0)	
		750 °C/2 h/WQ + 600 °C/2 h/WQ, longitudinal	1101 (27)	1145 (26)	15.9 (1.7)	
		750 °C/2 h/WQ + 600 °C/2 h/WQ, offset 45° along the longitudinal	1123 (6)	1166 (13)	15.6 (0.9)	
Ti-5Al-5Mo-5V-1Cr-1Fe	L-DED	As-built, longitudinal	1147 (15)	1178 (20)	5.0 (0.8)	[134]
		750 °C/2 h/FC, longitudinal	935 (5)	940 (5)	9.3 (1.2)	
		830 °C/2 h, FC to 750 °C/2 h/AC, longitudinal	898 (5)	906 (3)	16.5 (0.5)	
		830 °C/2 h, FC to 750 °C/2 h/AC, 600 °C/4 h/AC, longitudinal	1069 (25)	1120 (25)	7.8 (0.6)	
		870 °C/2 h, FC to 750 °C/2 h, 600 °C/4 h/AC, longitudinal	1036 (15)	1135 (7)	10.7 (1.2)	
Ti-5Al-5Mo-5V-1Cr-1Fe	L-DED	900 °C/0.5 h/FC + 830 °C/2 h/WQ, 830 °C/2 h, FC + 750 °C/2 h/AC + 600 °C/4 h/AC, longitudinal	1065 (5)	1107 (5)	11.5 (1.2)	[135]
		900 °C/0.5 h/FC + 840 °C/2 h/WQ, 830 °C/2 h, FC + 750 °C/2 h/AC + 600 °C/4 h/AC, longitudinal	1067 (6)	1111 (7)	12.3 (0.6)	
		900 °C/0.5 h/FC + 850 °C/2 h/WQ,	1037 (17)	1104 (20)	9.5 (1.1)	
		830 °C/2 h, FC + 750 °C/2 h/AC + 600 °C/4 h/AC, longitudinal				

(continued on next page)

Table 4 (continued)

Material	Method	State (i.e. treatments and testing directions)	Yield Stress (SD, MPa)	Ultimate Tensile Stress (SD, MPa)	Total Elongation (SD, %)	Ref.
Ti-5Al-5Mo-5V-1Cr-1Fe	EB-PBF	As-built (substrate heating 650 °C), transverse	987	1042	19.0	[122]
		As-built (substrate heating 650 °C), transverse	1053	1150	11.0	
		As-built (substrate heating 750 °C), transverse	1137	1178	7.0	
		As-built (substrate heating 750 °C), transverse	1172	1230	6.0	
Ti-5Al-2Sn-2Zr-4Mo-4Cr	L-PBF	As-built, transverse	-	1495	1.9	[136]
		600 °C/1 h/AC, transverse	-	1500	3.6	
		650 °C/1 h/AC, transverse	-	1478	3.8	
		660 °C/1 h/AC, transverse	-	1318	5.0	
		670 °C/1 h/AC, transverse	-	1305	6.2	
		680 °C/1 h/AC, transverse	-	1259	8.2	
		690 °C/1 h/AC, transverse	-	1218	10.2	
		700 °C/1 h/AC, transverse	-	1200	10.3	
		750 °C/1 h/AC, transverse	-	1115	11.0	
Ti-5Al-2Sn-2Zr-4Mo-4Cr	EB-DED	750 °C/2 h/WQ + 630 °C/4 h/AC, longitudinal	820	896	12.6	[137]
		850 °C/2 h/WQ + 630 °C/4 h/AC, longitudinal	986	1072	5.4	
		800 °C/2 h/WQ + 550 °C/4 h/AC, longitudinal	980	1137	4.2	
		800 °C/2 h/WQ + 630 °C/4 h/AC, longitudinal	888	989	10	
		800 °C/2 h/WQ + 710 °C/4 h/AC, longitudinal	783	846	17.9	
Ti-3Al-8V-6Cr-4Mo-4Zr	L-PBF	As-built, transverse	-	930	26.8	[138]
		520 °C/3 h/WQ, transverse	-	1425	7.8	
		480 °C/6 h/WQ, transverse	-	1611	5.4	
Ti-3Al-8V-6Cr-4Mo-4Zr	L-DED	As-built, transverse	880	915	23.0	[139]
		480 °C/6 h/AC, transverse	1415	1506	6.8	
Ti-6Al-2Sn-4Zr-6Mo	L-PBF	As-built, transverse	483	1183	25.0	[140]
		600 °C/2 h/FC, transverse	1383	1457	6.1	
		750 °C/2 h/FC, transverse	1060	1130	15.0	
		875 °C/2 h/FC, transverse	1055	1105	20.0	
		900 °C/2 h/FC, transverse	1005	1145	17.2	

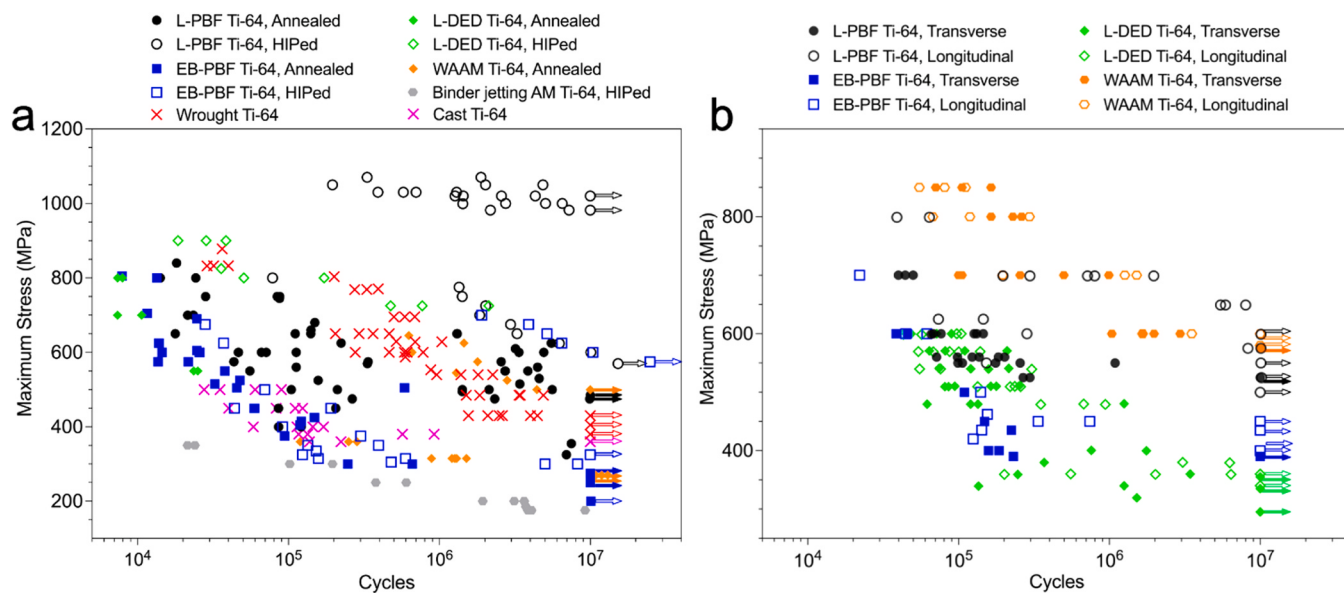


Fig. 2. (a) High-cycle fatigue properties of AM Ti-6Al-4V with consistent R as 0.1, including L-PBF, L-DED, EB-PBF, WAAM, and novel binder jetting AM Ti-6Al-4V by using optimal processing parameters with full annealing and post-AM HIP process, and compared with cast and wrought Ti-6Al-4V from ASM handbook [39,111,144,145,147,148-151,153,163,164]. The loading directions are all along the building direction. (b) The anisotropy of high-cycle fatigue properties of AM titanium alloys with consistent R as 0.1, including L-PBF [160], L-DED [165], EB-PBF [166], and WAAM Ti-6Al-4V [167] by using optimal processing parameters, all in as-built states.

and is comparable with that of wrought titanium alloys [74,199–204], as shown in Fig. 5. In the meanwhile, L-PBF Ti-6Al-4V in the heat-treated state exhibits reasonably consistent FCG resistance in both transverse and longitudinal directions (Fig. 5) [205,206]. For instance, the FCG thresholds of L-PBF Ti-6Al-4V after a full stress annealing, 650 °C for 3 h, are approximately in the range of 5.3–5.8 MPa $\sqrt{\text{m}}$ in both transverse and longitudinal directions, similar to that of conventionally manufactured Ti-6Al-4V (approximately 5.4 MPa $\sqrt{\text{m}}$) [22]. With more optimized heat treatments, the FCG thresholds of L-PBF Ti-6Al-4V can be

further enhanced, reaching the range of 7.1–8.4 MPa $\sqrt{\text{m}}$ after 920 °C/0.5 h + 700 °C/2 h/AC [205]. Furthermore, the FCG steady regime, which is commonly characterized by Paris equation $da/dN = C(\Delta K)^m$, is also reported as isotropic in L-PBF Ti-6Al-4V after the heat treatments, with the exponent m of this equation ranged from 3.2 to 4.0 in both transverse and longitudinal directions, which is also comparable with those in wrought Ti-6Al-4V (m value commonly between 3.0 and 4.8) [205,207,208].

In L-DED Ti-6Al-4V, the FCG thresholds (2.6–2.9 MPa $\sqrt{\text{m}}$) are

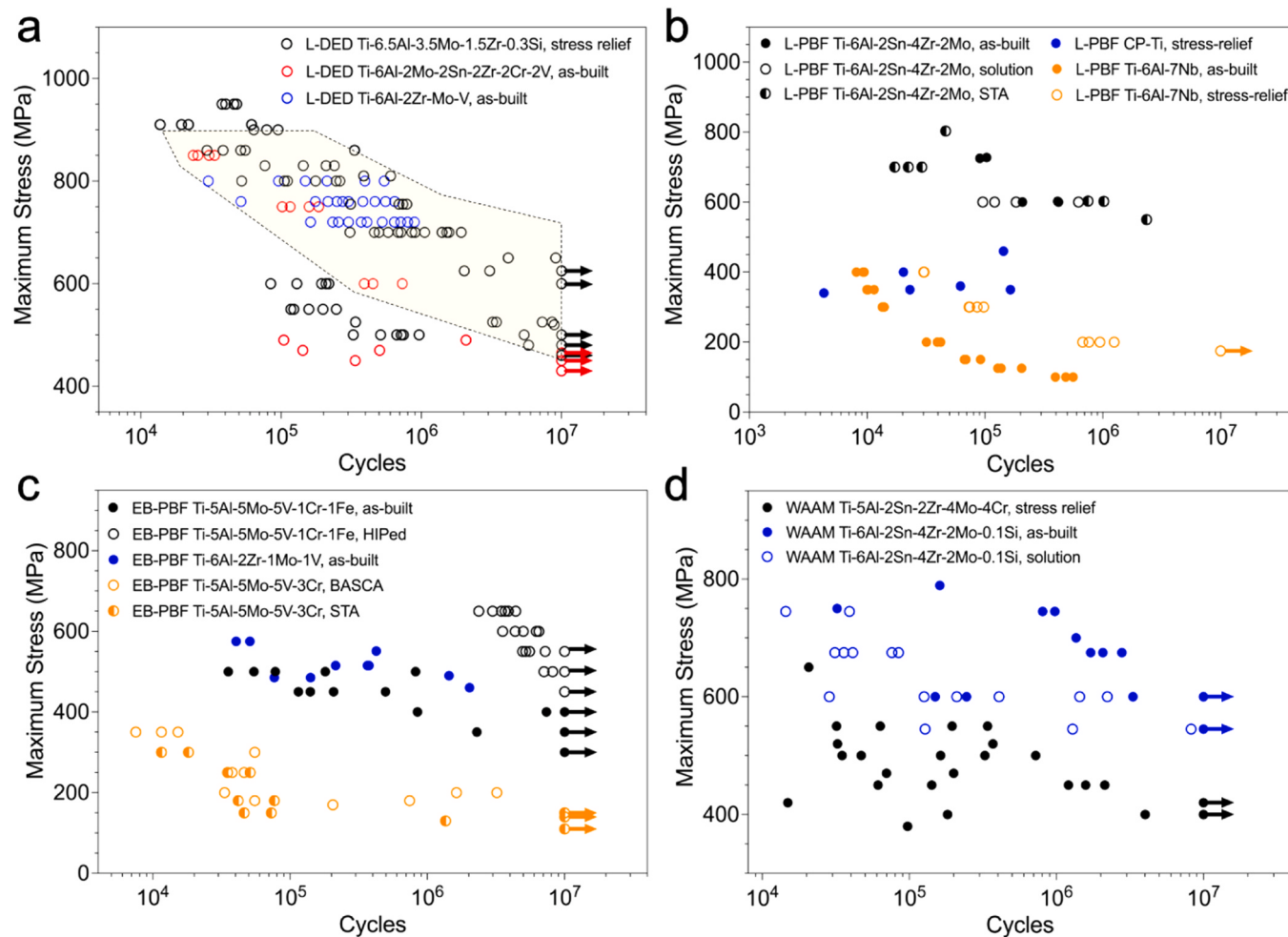


Fig. 3. High-cycle fatigue properties of additively manufactured titanium alloys other than Ti-6Al-4 V: (a) L-DED processed Ti-6.5Al-3.5Mo-1.5Zr-0.3Si [178], Ti-6Al-2Zr-Mo-V [171,172], and Ti-6Al-2Mo-2Sn-2Zr-2Cr-2V [173] ($R = 0.06$). The yellow area highlights the fatigue life of the L-DED Ti-64 for comparison [188, 189]. (b) L-PBF Ti-6Al-2Sn-4Zr-2Mo [179], CP-Ti [181], and Ti-6Al-7Nb [183] ($R = -1$). (c) EB-PBF Ti-5Al-5Mo-5V-1Cr-1Fe [185], Ti-5V-5Mo-5Al-3Cr [184], and Ti-6Al-2Zr-Mo-V [190] ($R = 0.1$) (d) WAAM Ti-5Al-2Sn-2Zr-4Mo-4Cr [187] and Ti-6Al-2Sn-4Zr-2Mo-0.1Si [191] ($R = -1$).

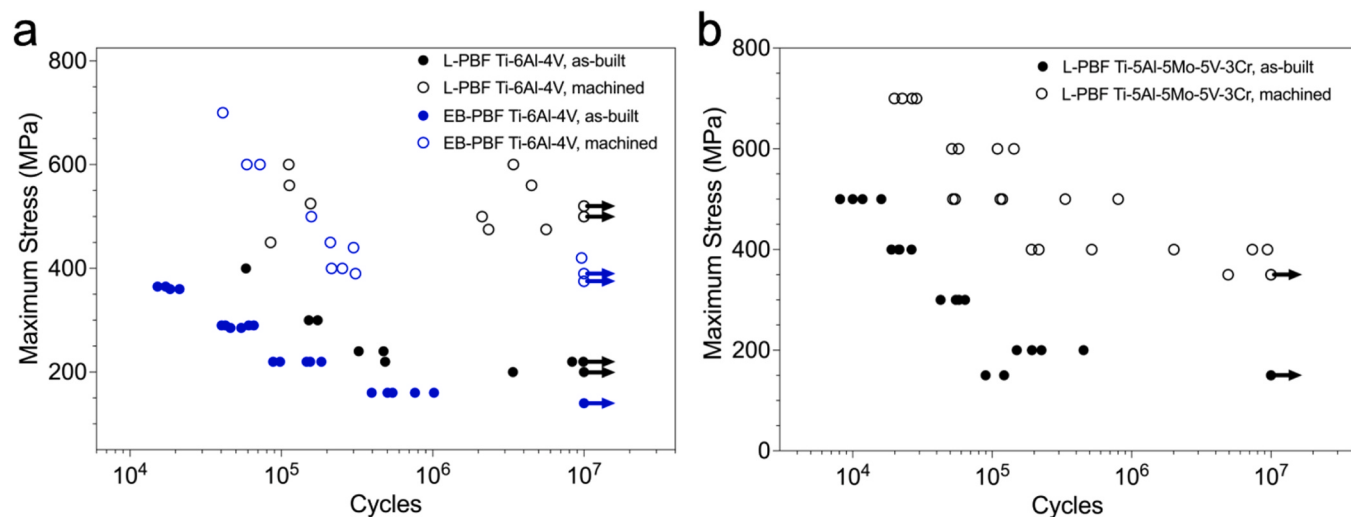


Fig. 4. Stress-life curves showing the HCF performances of (a) AM Ti-6Al-4V alloys in as-built and machined states [166,197] ($R = 0.1$), and (b) L-PBF Ti-5Al-5V-5Mo-3Cr in as-built and machined conditions [192] ($R = 0.1$).

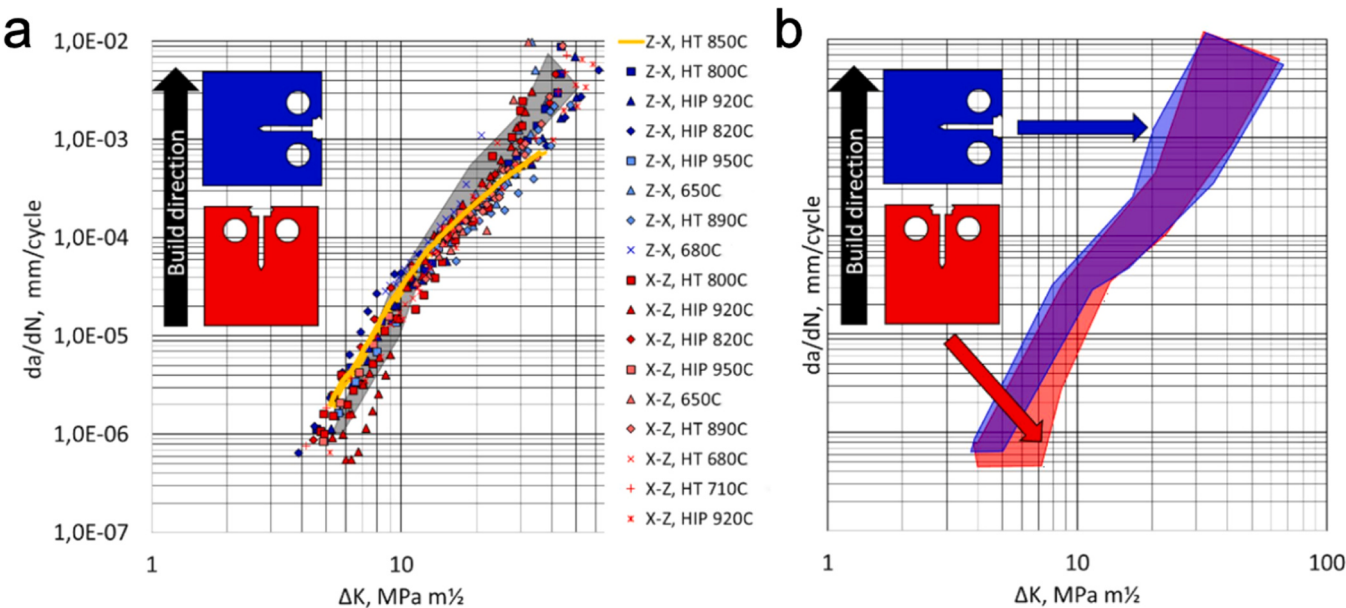


Fig. 5. (a) Fatigue crack propagation rates of L-PBF Ti-64 with different treatments (HIP and heat treatments), and compared with the conventionally manufactured Ti-64 [202–204]. The grey-colored area represents the conventionally manufactured Ti-64. (b) All FCG results combined. The red-colored means the Z-X crack direction, and the blue-colored means the X-Y crack direction.

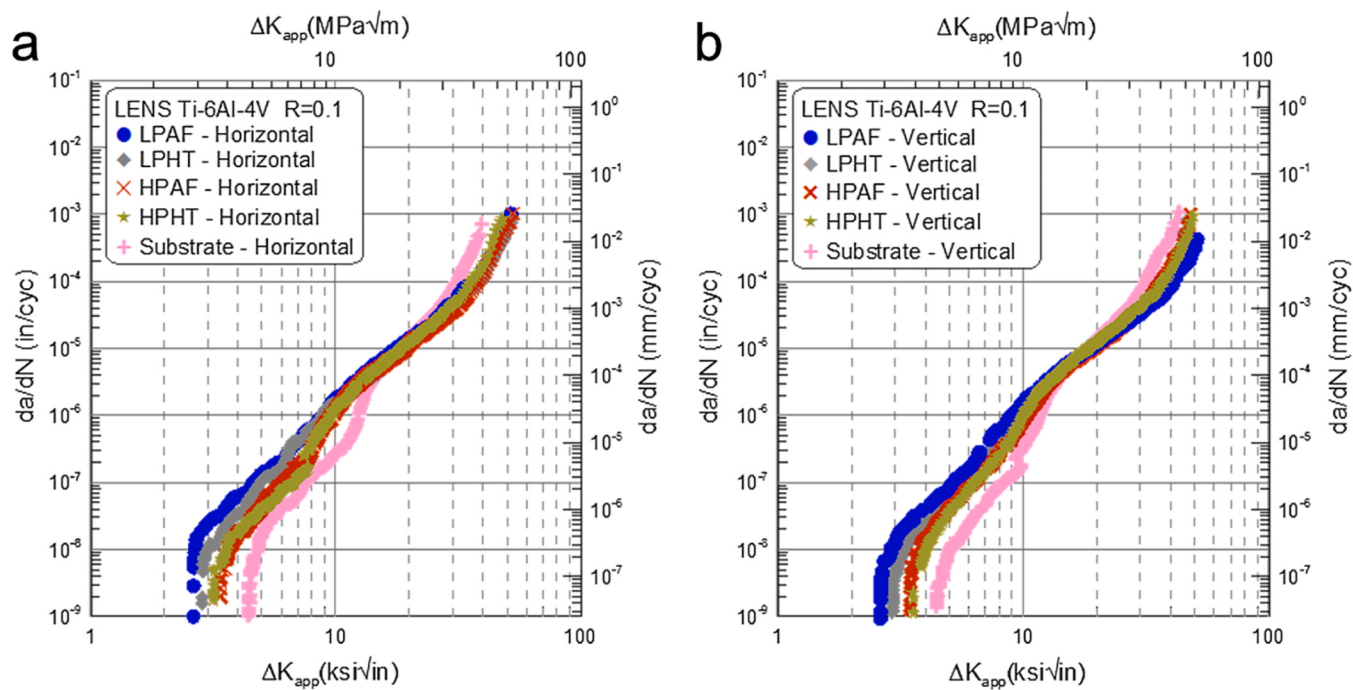


Fig. 6. FCG rates of L-DED Ti-6Al-4V with different processing parameters (LP, lower power; HP, high power) in both as-built and heat-treated (HT) states at (a) transverse and (b) longitudinal directions, and compared with those in taken from the substrate [199].

considered slightly smaller than those in wrought products, while the propagation rates during the steady regime are relatively comparable (m value ranged from 3.2 to 4.0), as shown in Fig. 6 [199,209]. Furthermore, the same study shows that the FCG propagation rates after the steady regime become slower as compared with those in wrought products [199]. The FCG resistance in EB-PBF Ti-6Al-4V is slightly better than that in wrought material, with similar fatigue thresholds and slightly better Paris law parameter (the exponent m value) (Fig. 7a) [210]. Further investigation into the effects of HIP on the FCG resistance in EB-PBF Ti-6Al-4V is carried out, and confirms that the reduction in

porosity may not be as beneficial as in HCF properties: the FCG thresholds might be improved after the HIP process, while the propagation resistance in Paris regime and that after Paris regime can be reduced [210]. Although the change of the microstructure after the HIP process is suspected to overwhelm the positive effects of porosity reduction on the FCG resistance, it also indicates the negligible effect of printing pores (under a reasonable level) on FCG resistance in AM titanium alloys.

Compared with other AM Ti-6Al-4V alloy, WAAM Ti-6Al-4V shows relatively high crack propagation resistances, with the m value ranged

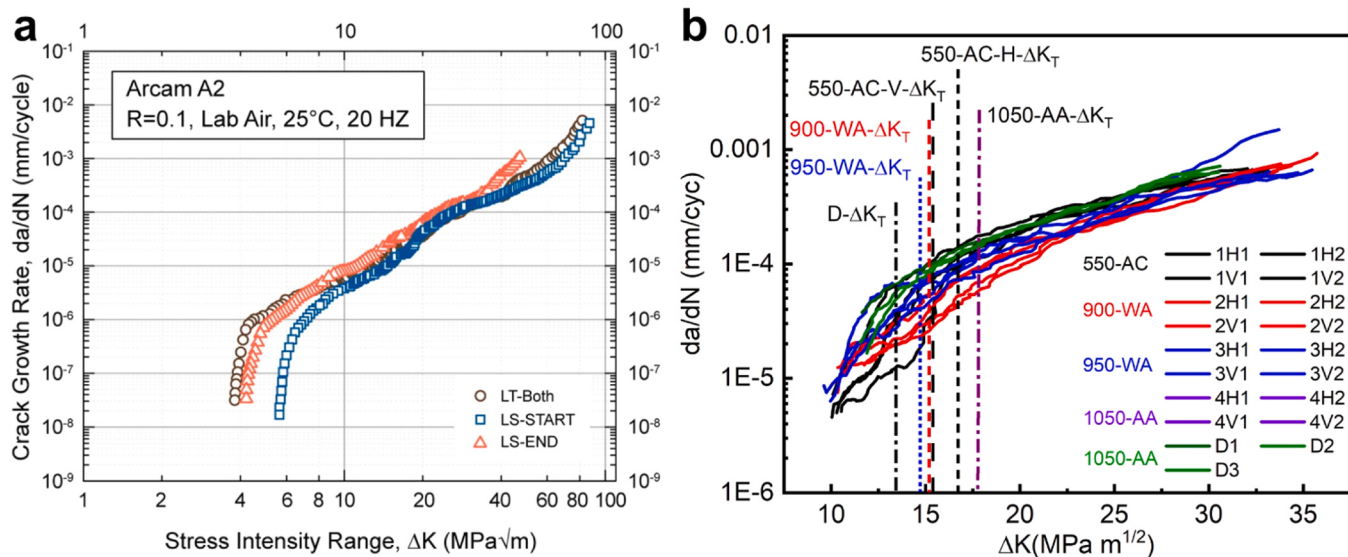


Fig. 7. (a) Fatigue crack propagation rates of EB-PBF Ti-6Al-4V at three different directions in the as-fabricated state [210], (b) fatigue crack propagation rates of WAAM Ti-6Al-4V after various heat treatments at both transverse (H) and vertical (V) directions [200].

from 2.8 to 3.5 (Fig. 7b) [211–214]. However, several works have indicated that the FCG rates of WAAM Ti-6Al-4V alloys are marginally greater in the longitudinal than the transverse direction after post-AM heat treatment, since the directional solidification with relatively small cooling rates (as compared with L-PBF, EB-PBF, and L-DED) during the WAAM process causes the presence of large columnar grains (even larger than 1 mm) and coarsening of continuous grain boundary α -phase [201]. These microstructure characteristics could serve as the favored fatigue crack propagation pathway, and lead to rapid crack propagation.

More investigations into the other AM titanium alloys have been also made in the published studies [74,170,215–218]. For instance, the FCG properties of commercially pure titanium (CP-Ti) fabricated by using L-PBF in different states (as-built and post-AM HIP state) are evaluated and compared with wrought CP-Ti (Fig. 8). The FCG properties of the L-PBF CP-Ti in the as-built state are better than the wrought CP-Ti, with improved consistency. The HIP process below the β transus temperature (post-AM HIP at 730°C for 1 h) and above the β transus (950°C for 1 h)

can further improve the FCG resistance, with consistency in both directions [74]. The anisotropy of FCG performances was further investigated in α titanium alloy, Ti-6.5Al-2Zr-1Mo-1V processed by WAAM [218]. No statistical difference can be found in samples with different directions, which is contrary to the conclusion drawn from WAAM Ti-6Al-4V (Fig. 8). This discrepancy is primarily attributed to differences in phases and grains between the two alloys (will be discussed in 5). In comparison, the high-temperature $\alpha+\beta$ titanium alloy, Ti-6.5Al-3.5Mo-1.5Zr-0.3Si, fabricated by L-DED, shows similar FCG rates in both directions, which is consistent with the conclusion for L-DED Ti-6Al-4V [170,219] (as shown in Fig. 8c).

More recent works on AM β -titanium alloys, including Ti-5Al-5Mo-5V-1Cr-1Fe [216,220] and Ti-5Al-3Mo-3V-2Zr-2Cr-1Nb-1Fe [219, 221], were also published. L-DED Ti-5Al-5Mo-5V-1Cr-1Fe alloy shows a classic three-stage response with an m value of around 3 in the Paris region. This value is comparable to L-DED Ti-6Al-4V [199,209]. However, significant fluctuations can be identified in the steady-state growth region. This could be related to the crack branching caused by coarse

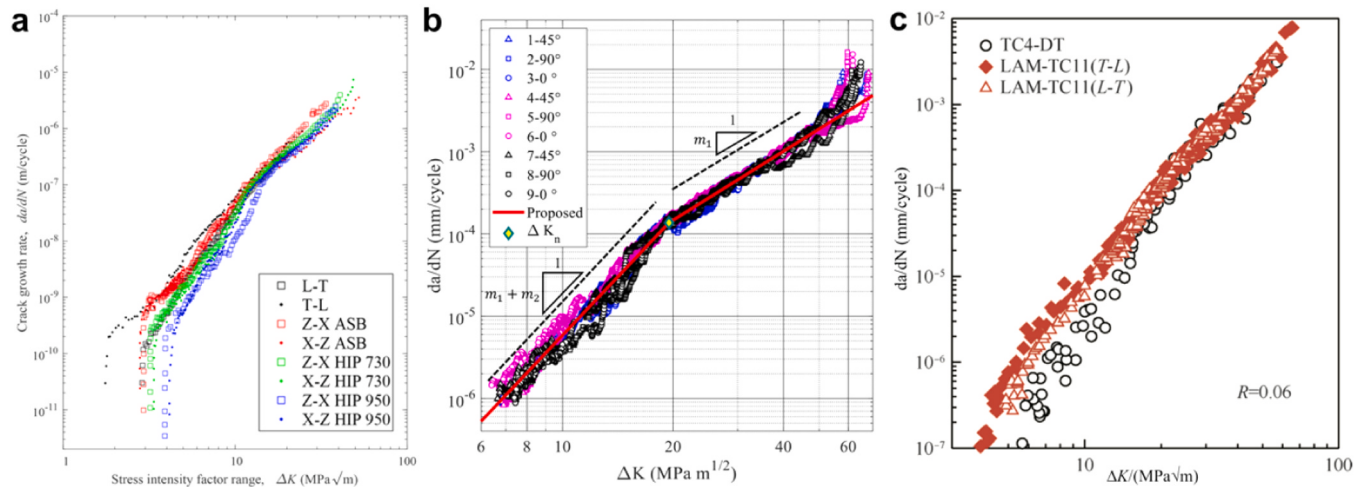


Fig. 8. (a) Fatigue crack propagation rates of L-PBF and wrought commercially pure titanium, with L-T and T-L representing the longitudinally and transversely oriented samples from wrought products, ASB represents L-PBF products in the as-built state, HIP represents L-PBF products after HIP at different temperatures [74]. (b) Fatigue crack propagation rates of WAAM Ti-6.5Al-2Zr-Mo-V in diagonal, longitudinal, and transverse directions [218]. (c) Fatigue crack propagation rates of L-DED (displayed as LAM) Ti-6.5Al-3.5Mo-1.5Zr-0.3Si in both longitudinal and transverse directions, and compared with L-DED Ti-6Al-4V ELI (labeled as TC4-DT) [170].

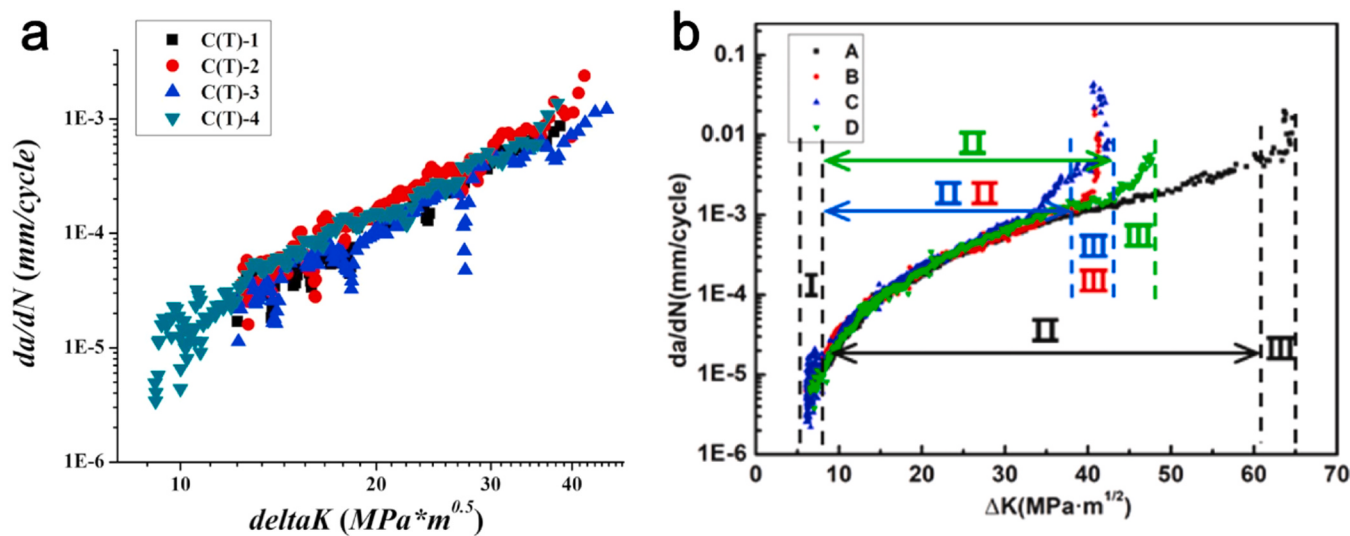


Fig. 9. Fatigue crack propagation rates of (a) L-DED Ti-5Al-5Mo-5V-1Cr-1Fe in transverse direction [216], and (b) L-DED Ti-5Al-3Mo-3V-2Zr-2Cr-1Nb-1Fe in transverse direction, with A, B, C, and D representing after 650 °C/4 h/AC, 880 °C/1 h cooling to 800 °C/AC + 580 °C/6 h/AC, 880 °C/1 h/AC + 580 °C/6 h/AC, and 800 °C/1 h/AC+ 580 °C/6 h/AC, respectively [221].

primary α lath. For L-DED Ti-5Al-3Mo-3V-2Zr-2Cr-1Nb-1Fe, the influence of four distinct post-build heat treatments on FCG performance was explored [221], and significant differences were observed, as shown in Fig. 9a. After undergoing stress-relieving treatment, L-DED Ti-5Al-3Mo-3V-2Zr-2Cr-1Nb-1Fe exhibits the highest FCG threshold value of 7.50 MPa \sqrt{m} as compared to other HT strategies. At the same time, a wider Paris region is also observed under this condition (zone II in Fig. 9b), indicating that the microstructure in this state has better fatigue crack resistance. Collectively, these results demonstrate that—much like in α and $\alpha+\beta$ systems—the FCG resistance of AM β -titanium alloys can be tailored through targeted microstructural engineering.

3.3. Fracture toughness

Fracture toughness defines the resistance to cracking of a material, which is a critical performance for ensuring structural integrity and reliability. For additive manufacturing of metallic materials, both plain-strain fracture toughness (K_{Ic}) and conditional fracture toughness (K_q) are used in the literature for the indication of the fracture toughness properties. It should be noted, however, conditional fracture toughness (K_q) is insufficient to satisfy the strain conditions specified by ASTM E399-12. Nevertheless, since the sample size for achieving a plain-strain state is much larger and difficult to obtain by using some AM methods like L-PBF, K_q values in the published works are considered valid [205]. For reference, conventionally wrought Ti-6Al-4V typically exhibits $K_{Ic} \approx 30-100$ MPa \sqrt{m} and $K_q \approx 88-110$ MPa \sqrt{m} (Table 5) according to the ASM handbook [222,223], which can be used here as the baseline.

Several studies have reported that the fracture toughness of AM Ti-6Al-4V alloys is comparable to that of conventionally manufactured Ti-6Al-4V, even though this often requires post-AM processing, as shown in Table 5 [28]. L-PBF Ti-6Al-4V in as-built state is very brittle with low fracture toughness properties (K_{Ic} commonly less than 30 MPa \sqrt{m}) due to the high residual stress and non-equilibrium microstructures. With post-AM heat treatments used, the fracture toughness properties of L-PBF Ti-6Al-4V can be significantly improved, achieving K_{Ic} value above 55 MPa \sqrt{m} and the K_q values exceeding 80 MPa \sqrt{m} [205,227]. Further optimization, like duplex heat treatment, can enhance K_q values to exceed 105 MPa \sqrt{m} [205]. This value exceeds that of most conventionally wrought titanium alloys [222,223].

In contrast, Ti-6Al-4V fabricated by other AM approaches like EB-

PBF and WAAM can achieve much higher fracture toughness properties without heat treatment (K_{Ic} values exceeding 50 MPa \sqrt{m} and K_q values above 110 MPa \sqrt{m}), potentially due to the lower residual stress and coarse microstructure caused by relatively slow cooling rates [210, 225,226]. Furthermore, the same studies found that post-AM HIP has minimal impact on these values [210]. This strongly indicates that the presence of pores, as long as the total porosity level is maintained below a reasonable and attainable value, is not influential on the fracture toughness properties.

In addition to Ti-6Al-4V, other conventionally high-toughness β titanium alloys processed by AM are also published, including Ti-5Al-3Mo-3V-2Zr-2Cr-1Nb-1Fe, Ti-6.5Al-3.5Mo-1.5Zr-0.3Si, Ti-5Al-5Mo-5V-1Cr-1Zr, and Ti-5Al-5Mo-5V-3Cr-1Zr (Table 5), which can also achieve competitive fracture toughness after appropriate post-AM heat treatment (K_{Ic} above 70 MPa \sqrt{m}) [233,234,230,232]. In particular, L-DED Ti-6.5Al-3.5Mo-1.5Zr-0.3Si can achieve a superior K_{Ic} value above 100 MPa \sqrt{m} after solution and aging treatment [230]. In addition, other AM $\alpha+\beta$ titanium alloys also show comparable fracture toughness to the conventionally manufactured counterpart. For instance, L-PBF Ti-5.6Al-3.8 V exhibits K_{Ic} values exceeding 75 MPa \sqrt{m} after stress relief treatment, which surpasses the basic forged Ti-5.6Al-3.8 V (K_{Ic} is around 70 MPa \sqrt{m}) [229]. These data show that the fracture toughness of AM titanium alloys could be comparable to that of wrought products and, can even surpass those of wrought products with more optimized heat treatments. This provided a new perspective for the AM titanium alloys to penetrate the application markets.

3.4. Fatigue and damage tolerance at extreme temperatures

3.4.1. Elevated temperatures

AM titanium alloys can also be employed for structural parts operating in the 200–600 °C temperature range such as gas turbine compressors and the blades of aero-engines [235]. In this case, evaluating their mechanical properties at the service temperatures is more valuable for the application than at room temperature. Due to the higher thermal stability, most high-temperature titanium alloys are α or $\alpha+\beta$ type titanium alloys. Fig. 10 shows the ultimate tensile strength and elongations for published AM titanium alloys as a function of testing temperature. As a general trend, tensile strength (refers to UTS) decreases while ductility improves with increasing temperature, which

Table 5

Fracture toughness values of AM Ti alloys, and compared with those of conventionally manufactured Ti alloys.

Material	Method	State and sample orientation*	Fracture toughness (K_{Ic} or K_q , MPa \sqrt{m}), with SD	Ref.
Ti-6Al-4V	Wrought	-	$K_{Ic} = 30\text{--}100$ $K_q = 88\text{--}110$	[223]
Ti-6Al-4V	L-PBF	As-built, Z-Y direction As-built, Y-Z _{up} direction As-built, Y-X direction 650 °C/4 h, Z-Y direction 650 °C/4 h, Y-Z _{up} direction 650 °C/4 h, Y-X direction 890 °C/2 h, Z-Y direction 890 °C/2 h, Y-Z _{up} direction 890 °C/2 h, Y-X direction	$K_{Ic} = 28$ (2) $K_{Ic} = 23$ (1) $K_{Ic} = 16$ (1) $K_{Ic} = 28$ (2) $K_{Ic} = 30$ (1) $K_{Ic} = 31$ (1) $K_{Ic} = 41$ (2) $K_{Ic} = 49$ (2) $K_{Ic} = 49$ (1)	[208]
Ti-6Al-4V	L-PBF	950 °C/1 h + 700 °C/1 h, X-Y direction 950 °C/1 h + 700 °C/1 h, X-Z direction	$K_{Ic} = 80$ (4) $K_{Ic} = 84$ (4)	[224]
Ti-6Al-4V	L-PBF	Varied process parameters, 650 °C/3 h, X-Y direction Varied process parameters, X-Z direction	$K_{Ic} = 48\text{--}58$ (52, 48, 51, 58) $K_{Ic} = 52\text{--}58$ (55, 54, 52, 58)	[22]
Ti-6Al-4V	L-PBF	Varied process parameters, 920 °C/3 h, cooling to 700 °C/2 h, X-Z direction Varied process parameters, 920 °C/3 h, cooling to 700 °C/2 h, X-Y direction	$K_q = 96\text{--}106$ (106, 96, 97, 101) $K_q = 77\text{--}95$ (77, 93, 83, 95)	[205]
Ti-6Al-4V	L-PBF	710 °C/2 h, X-Y direction HIP (920 °C/100 MPa/2 h), X-Z direction	$K_{Ic} = 49.5$ (1.5) $K_q = 93.5$ (0.5)	[150]
Ti-6Al-4V	EB-PBF	As-built, Z-X direction As-built, X-Z _{up} direction As-built, Z-Y direction As-built, Y-X direction As-built, Z-X direction As-built, X-Y direction As-built, Y-X direction As-built, X-Z direction	$K_q = 68, 80$ $K_q = 76$ $K_q = 67$ $K_q = 65$ $K_q = 82$ $K_q = 91$ $K_q = 105$ $K_q = 95$	[225]
Ti-6Al-4V	EB-PBF	HIP (950 °C/100 MPa/3 h), Z-X direction HIP (950 °C/100 MPa/3 h), Y-X direction HIP (950 °C/100 MPa/3 h), X-Y direction HIP (950 °C/100 MPa/3 h), X-Z direction	$K_q = 84$ $K_q = 84$ $K_q = 96$ $K_q = 94$	[210]
Ti-6Al-4V	EB-PBF	As-built, X-Y direction As-built, X-Z direction	$K_q = 110$ (8.9) $K_q = 102$ (7.4)	[226]
Ti-6Al-4V	EB-PBF	710 °C/2 h, X-Y direction HIP (920 °C/100 MPa/2 h), X-Z direction	$K_q = 106.5$ (3.5) $K_q = 119$	[150]
Ti-6Al-4V	L-DED	1000 °C/1 h, X-Y direction	$K_{Ic} = 83.6$ (31.3)	[223]
Ti-6Al-4V	WAAM	As-built, Y-X direction As-built, Y-Z _{up} direction	$K_{Ic} = 74.3$ (2.6) $K_{Ic} = 82.1$ (1.5)	[227]
Ti-6Al-3Mo-1Zr	L-PBF	As-built, Y-X direction 800 °C/2 h/FC, Y-X direction	$K_{Ic} = 33.9$ $K_{Ic} = 43.9$	[228]
Ti-5.6Al-3.8 V	L-PBF	580 °C/6 h/AC, X-Y direction	$K_{Ic} = 77.1$	[229]
Ti-6.5Al-3.5Mo-1.5Zr-0.3Si	L-DED	1000 °C/2 h/AC + 530 °C/4 h, Y-X direction 1000 °C/2 h/AC + 530 °C/4 h, Y-Z _{up} direction	$K_{Ic} = 116.1$ $K_{Ic} = 115.1$	[230]
Ti-5Al-3Mo-3V-2Zr-2Cr-1Nb-1Fe	L-DED	530 °C/6 h/AC, X-Y direction 880 °C/1 h cooling to 800 °C/6 h/AC + 580 °C/6 h/AC, X-Y direction	$K_{Ic} = 68.0$ $K_{Ic} = 46.0$	[219]
Ti-5Al-5Mo-5V-1Cr-1Fe	L-PBF	-		
Ti-5Al-5Mo-5V-1Cr-1Fe	L-PBF	830 °C/1.5 h/AC + 620 °C/6 h/AC, X-Z direction 900 °C/1.5 h cooling to 600 °C/6 h/FC, X-Z direction	$K_{Ic} = 64.0$ (2.1) $K_{Ic} = 70.0$ (2.2)	[231]
Ti-5Al-5Mo-5V-1Cr-1Fe	L-PBF	920 °C/2 h/WQ + 600 °C/2 h/WQ, X-Y direction 770 °C/2 h/WQ + 500 °C/6 h/WQ, X-Y direction 840 °C/1 h cooling to 750 °C/2 h/AC + 580 °C/4 h/AC, X-Y direction	$K_{Ic} = 62.3$ (1.1) $K_{Ic} = 44.1$ (2.4) $K_{Ic} = 72.9$ (3.9)	[232]
Ti-5Al-5Mo-5V-3Cr-1Zr	EB-PBF	As-built, Y-Z _{up} direction As-built, Y-X direction As-built, Y-Z _{down} direction	$K_{Ic} = 81.6$ $K_{Ic} = 86.2$ $K_{Ic} = 75.1$	[233]
Ti-5Al-5Mo-5V-3Cr-1Zr	L-DED	865 °C/0.5 h cooling to 715 °C/2 h/AC + 620 °C/4 h/AC, X-Z direction 830 °C/1.5 h/WQ + 620 °C/10 h/AC, X-Z direction	$K_q = 81.7$ (1.1) $K_q = 51.6$ (6.8)	[234]

*: The first and last letters in sample orientation denote the crack opening and crack growth direction, respectively. Up or down represent cracks growth from the top or bottom.

could be attributed to the increased dislocation mobility and potential grain boundary sliding [236–238]. Table 6 further summarizes the specific high-temperature tensile properties for various AM titanium alloys. Below 500 °C, most AM α or $\alpha+\beta$ titanium alloys could provide superior tensile strength compared to conventionally manufactured Ti alloys. For instance, L-PBF Ti-6Al-2Zr-1Mo-1V has a UTS of 907 MPa at 500 °C (the UTS of wrought Ti-6Al-2Zr-1Mo-1V is only 650 MPa at 500 °C [239]) [87]. However, once the temperature exceeds 500 °C, the tensile strength of AM α or $\alpha+\beta$ titanium alloys is significantly reduced

(e.g., the UTS of L-PBF Ti-6Al-4V drastically decreased from 834 MPa to 562 MPa as the testing temperature increased from 500 °C to 550 °C [240]). This could be related to the decomposition of martensites, which will be discussed in 5.3.1.

Furthermore, it is found that most conventionally high-temperature titanium alloys (like Ti-6Al-2.7Sn-4Zr-0.4Mo-0.45Si [259] and Ti-6Al-4Sn-4Zr-0.5Mo-0.65 Nb (IMI834) [260]) are not suitable for additive manufacturing technologies [248]. This is attributed to the wide range of solidification temperatures of these alloys, which can

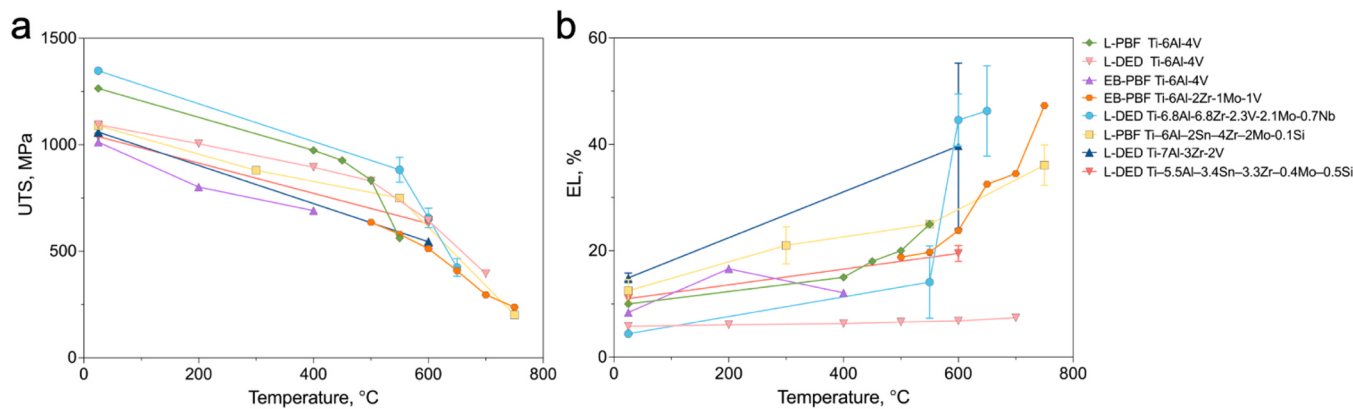


Fig. 10. (a) Ultimate tensile stress and (b) elongation as a function of temperature for AM titanium alloys [87,240,248,250,243,251,249,245,247,242]. Table 6 gives more detail for all the data shown.

cause microstructural inhomogeneities and printing pores formation [261]. To this end, high-temperature titanium alloys tailored for AM were designed based on the ‘cluster formula method’ [248,250]. This strategy takes Ti-6Al-4V as the compositional prototype, which can be represented by the 17-unit dual-cluster formula, $\alpha\text{-}\{\text{Al-Ti}_{12}\}(\text{AlTi}_2)_{12} + \beta\text{-}\{\text{Al-Ti}_{14}\}(\text{V}_2\text{Ti})_5$. On this basis, the composition is modified to enhance β -phase stability and narrow the liquidus–solids interval, which benefits additive manufacturing. For instance, Ti-6.8Al-6.8Zr-2.3V-2.1-Mo-0.7 Nb was designed by retaining the 12:5 α : β unit ratio of Ti-6Al-4V and co-alloying the β unit to $[\text{Al-Ti}_{12}\text{Zr}_2](\text{AlV}_{1.2}\text{Mo}_{0.6}\text{Nb}_{0.2})$ while keeping the liquidus–solids interval (~ 27 °C) compatible with AM [248]. L-DED Ti-6.8Al-6.8Zr-2.3V-2.1Mo-0.7 Nb exhibits impressive ductility over 45 % and tensile strength of > 400 MPa at 650 °C (for comparison, the elongation of L-DED Ti-64 is only 7.4 % at 700 °C [243]) [248]. Another example is Ti-7Al-3Zr-2V, derived by increasing the α -unit fraction from the Ti-6Al-4V parent to 15/17 and converting the β -unit to $\{\text{Al-Ti}_{12}\text{Zr}_2\}(\text{V}_3)_2$, achieving a narrow liquidus–solidus interval (~ 7 °C) suitable for AM [250]. L-DED Ti-7Al-3Zr-2V also shows the high-temperature strength–ductility trade-off compared to L-DED Ti-64 (L-DED Ti-7Al-3Zr-2V has a tensile strength and ductility of 545 MPa and 39.7 % at 600 °C [250], while L-DED Ti-64 has a tensile strength and ductility of 645 MPa and 6.8 % [243]).

In addition to tensile performance, high-temperature fatigue performance is also a critical factor in determining the serviceability of AM titanium alloys in elevated environments. Very high cycle fatigue (VHCF) tests performed at various temperatures [262–264] show that the fatigue properties of L-PBF Ti-6Al-4V tested at 350 °C and 400 °C decrease significantly under high-stress levels as compared to the room temperature (Fig. 11a). Specifically, fatigue samples tested at 350 °C failed at 10^5 cycles under 300 MPa stress level, while those of specimens tested at 25 °C at the same stress level reached 10^7 cycles. In contrast, the fatigue life under relatively low-stress levels becomes similar (both $> 10^7$ cycles at 250 MPa). Furthermore, under the evaluated stress conditions, the fatigue performance of L-PBF Ti-6Al-4V at 350 °C is much better than that of conventionally manufactured Ti-6Al-4V [265, 266]. On this basis, post-AM HIP, which could eliminate pores like LOF, can further enhance the high-temperature fatigue performance of L-PBF Ti-6Al-4V (improve fatigue strength at 350 °C from ~ 250 MPa (as-built) to ~ 350 MPa (after HIP), Fig. 11a). The beneficial effects that printing pore are also detrimental to high-temperature fatigue performance, which is consistent with conclusions drawn from room-temperature HCF performance.

Apart from commonly used Ti-6Al-4V, the elevated-temperature HCF performance of L-PBF Ti-6.5Al-3.5Mo-1.5Zr-0.3Si (high-temperature α + β titanium alloy) has been investigated recently, as shown in Fig. 11b [267]. It was found that L-PBF Ti-6.5Al-3.5Mo-1.5Zr-0.3Si still maintains an acceptable fatigue performance at testing temperatures up

to 500 °C (while Ti-64 could only operate up to 300 °C), with a fatigue life of 10^6 cycles at 230 MPa. In addition, L-DED Ti-5.8Al-3.5Zr-3.5Sn-0.5Mo-2.0Ta-0.3Nb-0.4Si-0.8 W (Ti-65, which belongs to the same Al-cluster formula family as aforementioned Ti-6.8Al-6.8Zr-2.3V-2.1Mo-0.7 Nb) exhibits superior high-temperature HCF performance up to 650 °C, achieving the fatigue strength of ~ 375 MPa (Fig. 11c) [246]. These results further indicate that AM titanium alloy has the potential for service at temperatures up to 650 °C.

The damage tolerance performance of AM titanium alloy, including fracture toughness and fatigue crack growth (FCG) resistance, at elevated temperatures has also been investigated [228]. L-PBF Ti-6Al-3Mo-1Zr (a high-temperature α + β titanium alloy) shows a relatively low fracture toughness of 33.9 MPa $\sqrt{\text{m}}$ at room temperature, while this value significantly improves to 87.6 MPa $\sqrt{\text{m}}$ at 300 °C. But with the testing temperature increase to 500 °C, the fracture toughness of L-PBF Ti-6Al-3Mo-1Zr decreases to 51.6 MPa $\sqrt{\text{m}}$, and further drops to 29.1 MPa $\sqrt{\text{m}}$ at 600 °C, which is even lower than that at RT. The significant deterioration of fracture toughness from 300 °C to 500 °C could be attributed to more intense oxidation at higher temperatures, leading to the embrittlement of the titanium alloy. Regarding fatigue crack growth (FCG) rates, irrespective of whether it is as-built or post-AM heat treatment states, an increase in temperature leads to a decline in FCG resistance within the Paris regime, which is illustrated by the upward shift of the FCG curves with temperature rises (Fig. 12). However, due to the creep-related blunting of the crack tip at high temperatures, the m values for both as-built and heat-treated samples decrease with the increase of test temperature, indicating a slower acceleration in crack propagation rate with increasing ΔK . At the testing temperature over 500 °C, the m values are even below 2 (for instance, the m value of the as-built sample is 1.5 at 600 °C), which is much lower than the typical range of 2 ~ 4 for common metals at room temperature [28].

3.4.2. Cryogenic temperatures

Owing to the highest specific strength and extremely low thermal expansion coefficient (at low temperature) among commonly cryogenic metallic materials (including Al alloys, austenitic stainless steels, titanium alloys, and nickel alloys, etc.), coupled with high design freedom offered by AM, AM titanium alloys are increasingly utilized in structural components intended for cryogenic environments [268]. Table 7 summarizes the cryogenic-temperature tensile properties of various titanium alloys processed by AM. For most commonly L-PBF Ti-6Al-4V, the UTS significantly increases (from 1027 MPa to 1332 MPa) with the testing temperature decreasing from RT to -150 °C, while the ductility experiences a slight reduction (from 16 % to 13 %) [269]. This trend is similar to that observed in conventionally manufactured Ti-6Al-4V, while cast Ti-6Al-4V becomes more brittle (with a limited ductility of 2.9 %) when subjected to -196 °C testing [270]. L-PBF Ti-5Al-2.5Sn

Table 6

High-temperature tensile properties of AM Ti alloys, and compared with those of conventionally manufactured Ti alloys.

Material	Method	State (i.e. treatments and testing directions)	Testing temperature (°C)	Yield Stress (SD, MPa)	Ultimate Tensile Stress (SD, MPa)	Total Elongation (SD, %)	Ref.
Ti-6Al-4V	L-PBF	HIP (945 °C/103 MPa/2 h), longitudinal	25	-	945	7.8	[241]
			250	-	715	24.5	
			450	-	587	21.5	
Ti-6Al-4V	L-PBF	As-built, transverse	25	1025	1210	7.8	[242]
			250	1000	1203	9.7	
			300	923	1102	9.6	
			350	873	1107	9.8	
			400	839	1016	7.8	
Ti-6Al-4V	L-PBF	As-built, transverse	25	-	1265	10.0	[240]
			400	-	974	15.0	
			450	-	927	18.0	
			500	-	834	20.0	
			550	-	562	25.0	
Ti-6Al-4V	L-DED	As-built, transverse	25	-	1095	5.8	[243]
			200	-	1005	6.1	
			400	-	895	6.3	
			500	-	830	6.6	
			600	-	645	6.8	
Ti-6Al-4V	EB-PBF	As-built, longitudinal	25	953	1013	8.4	[244]
			200	708	802	16.6	
			400	575	691	12.1	
			25	927	1007	12.6	
			400	506	658	14.5	
Ti-6Al-2Zr-1Mo-1V	L-PBF	As-built, transverse	25	-	1234 (53)	7.3 (0.7)	[87]
			500	-	907 (5)	11.8 (0.4)	
			650 °C/4 h/AC, transverse	25	1207 (4)	8.9 (0.1)	
			500	-	853 (11)	12.5 (1.1)	
			750 °C/4 h/AC, transverse	25	1123 (14)	11.3 (0.7)	
			500	-	757 (7)	13.4 (1.1)	
			850 °C/4 h/AC, transverse	25	1025 (20)	9.0 (0.4)	
			500	-	715 (4)	13.0 (0.9)	
			950 °C/4 h/AC, transverse	25	936 (5)	8.0 (1.0)	
			500	-	640 (7)	14.3 (0.9)	
			1000 °C/4 h/AC, transverse	25	907 (5)	5.8 (0.2)	
			500	-	602 (5)	15.9 (5.0)	
			1100 °C/4 h/AC, transverse	25	780 (7)	3.8 (0.4)	
Ti-6Al-2Zr-1Mo-1V	EB-PBF	As-built, transverse	500	-	596 (6)	15.6 (2.5)	
			500	498	636	18.8	[245]
			550	474	580	19.7	
			600	453	513	23.8	
			650	378	409	32.5	
			700	272	296	34.5	
			750	209	238	47.3	
Ti-5.8Al-3.5Zr-3.5Sn-0.5Mo-2.0Ta-0.3Nb-0.4Si-0.8 W	L-DED	As-built, longitudinal	500	515	640	19.3	
			25	967	1058	9.1	[246]
Ti-5.8Al-4Sn-4Zr-0.7Nb-1.5Ta-0.4Si	EB-DED	As-built, longitudinal	650	525	690	23.6	
			25	850	924	8.2	[247]
		As-built, transverse	600	441	558	12.7	
			25	863	932	7.1	
			600	452	569	11.4	
			1030 °C/2 h/AC	25	823	897	11.4
			+ 750 °C/2 h/AC, longitudinal	600	422	543	16.0
			1030 °C/2 h/AC	25	832	911	11.0
			+ 750 °C/2 h/AC, transverse	600	433	554	15.1
Ti-6Al-3Mo-1Zr	L-PBF	As-built, transverse	25	1167 (12)	1281 (5)	5.8 (0.6)	[228]
			300	881 (38)	1037 (28)	6.9 (0.6)	
			500	827 (60)	934 (49)	6.3 (0.9)	
			600	487 (50)	587 (41)	3.8 (0.9)	
			800 °C/2 h/FC, transverse	25	1022 (11)	1093 (12)	8.8 (1.0)
			800 °C/2 h/FC, transverse	300	697 (10)	828 (8)	15.0 (0.4)
			800 °C/2 h/FC, transverse	500	606 (17)	692 (18)	16.2 (1.8)
			800 °C/2 h/FC, transverse	600	563 (20)	637 (2)	16.9 (2.8)
			25	1253 (11)	1348 (15)	4.4 (0.5)	[248]
			550	829 (36)	883 (59)	14.1 (6.8)	
Ti-6.8Al-6.8Zr-2.3V-2.1Mo-0.7 Nb	L-DED	As-built, transverse	600	578 (24)	657 (46)	44.6 (4.9)	

(continued on next page)

Table 6 (continued)

Material	Method	State (i.e. treatments and testing directions)	Testing temperature (°C)	Yield Stress (SD, MPa)	Ultimate Tensile Stress (SD, MPa)	Total Elongation (SD, %)	Ref.
Ti-5.5Al-3.4Sn-3.3Zr-0.4Mo-0.5Si	L-DED	650 °C/4 h/AC, transverse	650	337 (23)	424 (42)	46.3 (8.5)	[249]
			25	965 (12)	1048 (6)	7.5 (1.0)	
			600	513 (2)	655 (10)	14.0 (1.5)	
			1020 °C/1 h/AC	25	936 (13)	1033 (11)	
			+ 700 °C/2 h/AC, transverse	600	468 (25)	605 (40)	
			1040 °C/1 h/AC	25	944 (2)	1039 (4)	
			+ 700 °C/2 h/AC, transverse	600	495 (5)	630 (5)	
Ti-7Al-3Zr-2V	L-DED	As-built, transverse	25	976 (2)	1060 (17)	14.9 (0.9)	[250]
			600	497 (12)	545 (11)	39.7 (15.6)	
Ti-6Al-2Sn-4Zr-2Mo-0.1Si	L-PBF	940 °C/1 h/AC + 595 °C/8 h/AC, longitudinal	25	1045 (4)	1130 (0)	16.2 (0.3)	[251]
			300	751 (1)	902 (2)	21.0 (0.5)	
			550	572 (9)	697 (8)	18.0 (1.0)	
			750	141 (16)	156 (12)	79.2 (4.9)	
			25	985 (5)	1064 (4)	12.2 (0.3)	
		980 °C/1 h/AC + 595 °C/8 h/AC, longitudinal	300	700 (6)	860 (3)	22.2 (1.0)	
			550	585 (0)	703 (7)	30.3 (2.1)	
			750	147 (2)	163 (2)	71.2 (3.8)	
			25	988 (4)	1090 (0)	12.5 (2.1)	
			300	720 (7)	880 (3)	21.0 (3.5)	
Ti-6Al-2Sn-4Zr-2Mo-0.1Si	L-PBF	As-built	550	617 (1)	750 (8)	25.0 (0.7)	[252]
			750	192 (0)	202 (2)	36.1 (3.8)	
			25	1296 (44)	1437 (13)	5.7 (1.1)	
			500	886 (16)	1045 (6)	6.3 (1.8)	
			955 °C/0.5 h/AC	25	1068 (3)	1162 (7)	14.9 (0.9)
		+ 595 °C/8 h/AC 1050 °C/2 h/FC	500	658 (20)	829 (16)	14.8 (0.8)	
			25	963 (12)	1034 (15)	8.0 (2.1)	
			500	505 (5)	647 (4)	12.9 (2.2)	
			925 °C/2 h/WQ	25	992 (35)	1243 (16)	14.5 (1.5)
Ti-6Al-2Sn-4Zr-2Mo-0.1Si	L-DED	+ 595 °C/6 h/AC, transverse	500	706 (9)	900 (8)	11.0 (0.8)	[253]
			25	543	722	18.3	
			480	883	997	15.5	
		960 °C/1 h/AC + 595 °C/6 h/AC, longitudinal	25	519	698	20.1	
			480	840	978	16.0	
Ti-6Al-4V	Wrought	As-received	25	840	920	10.0	[254]
			125	710	810	15.0	
			225	600	730	16.5	
			350	515	650	18.0	
Ti-6Al-2Zr-1Mo-1V	Rolled	As-received	25	946	955	13.5	[255]
			500	553	640	16.8	
Ti-6Al-2Zr-1Mo-1V	Wrought	850 °C/1.5 h/AC	25	905	965	16.0	[239]
			500	515	640	19.3	
Ti-6Al-2Sn-4Zr-2Mo-0.1Si	Cast	HIP (900 °C/100 MPa/2 h)	455	542	569	8.2	[256]
			25	867	968	10.2	
Ti-6Al-4Sn-4Zr-0.5Mo-0.65 Nb (IMI834)	Cast	Annealed	500	430	594	11.1	[257]
			25	1047	1170	12.2	
			300	795	957	11.7	
			400	681	851	12.0	
			500	657	812	11.0	
			600	612	730	12.0	

exhibits almost consistent cryogenic-temperature tensile performance after post-AM heat treatment and HIP under the same temperature and dwell time conditions [89]. Specifically, after post-AM heat treatment at 850 °C/2 h/FC, L-PBF Ti-5Al-2.5Sn shows a UTS of ~1455 MPa and an elongation of ~13.1 % at -196 °C. Similarly, after post-AM HIP at 850 °C/120 MPa for 2 h, it demonstrates a comparable UTS of 1498 MPa and ductility of 12.5 %. This suggests that the impact of printing pores on cryogenic-temperature tensile performance is relatively minor. In addition, due to the requirement of high strength under load-bearing conditions, L-PBF Ti-6.5Al-2Zr-Mo-V was reported to achieve an ultra-high UTS exceeding 1700 MPa and an acceptable ductility of 5.2 % at -196 °C [271]. For applications at lower temperatures (liquid-hydrogen temperature, -253 °C), Ti-3Al-3Mo-3Zr-0.2Y was developed and successfully fabricated by EB-PBF, which exhibits a UTS of 1410 MPa and excellent ductility over 20.0 % at -253 °C [272].

However, due to the localized strain hardening and discontinuous plastic flow (with detailed discussion in 5.3.2), EB-PBF Ti-3Al-3Mo-3Zr-0.2Y show the serrated tensile curves with stress fluctuating periodically at -253 °C. During the tensile process, the stress amplitude ($\Delta\sigma$) gradually increases during the tensile process as the strain increment ($\Delta\varepsilon$) between adjacent valley values of flow stress increases. This behavior is different the continuous strain-stress curve typically observed in most titanium alloys at room temperature (Fig. 13a). Correspondingly, multiple necking phenomena can be observed on the tensile sample fracture at -253 °C (Fig. 13b), which is also different from the single necking seen at room temperature.

Furthermore, compared to the extensively investigated tensile properties, only a few studies in L-PBF Ti-6Al-4V focused on fracture toughness at cryogenic temperature. L-PBF Ti-6Al-4V shows the fracture toughness of 64.8 MPa \sqrt{m} at room temperature, while at -50 °C and

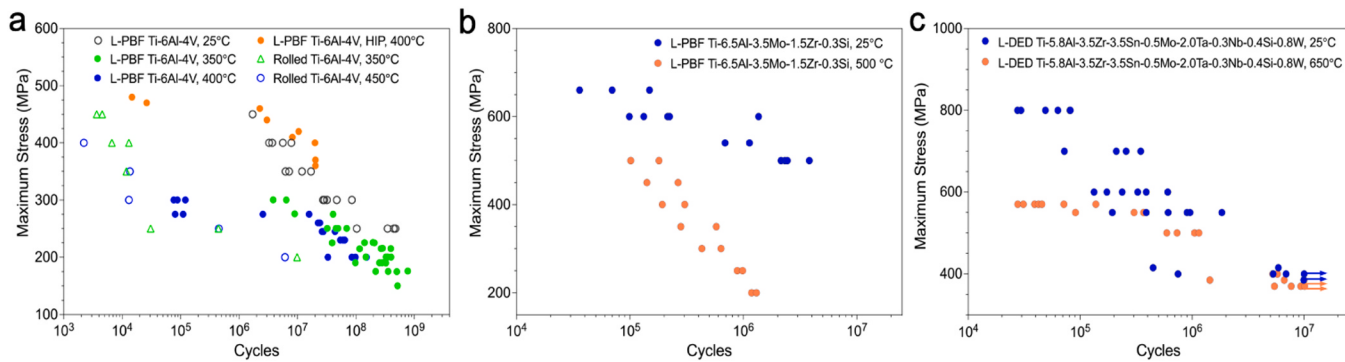


Fig. 11. High-cycle fatigue properties of AM titanium alloys at different testing temperatures: (a) L-PBF Ti-6Al-4V [262–264] with consistent R as -1 , and compared with rolled Ti-6Al-4V [266]. (b) L-PBF Ti-6.5Al-3.5Mo-1.5Zr-0.3Si with the R of 0.1 [267]. (c) L-DED Ti-5.8Al-3.5Zr-3.5Sn-0.5Mo-2.0Ta-0.3Nb-0.4Si-0.8 W (Ti-65) with the R of -1 [246].

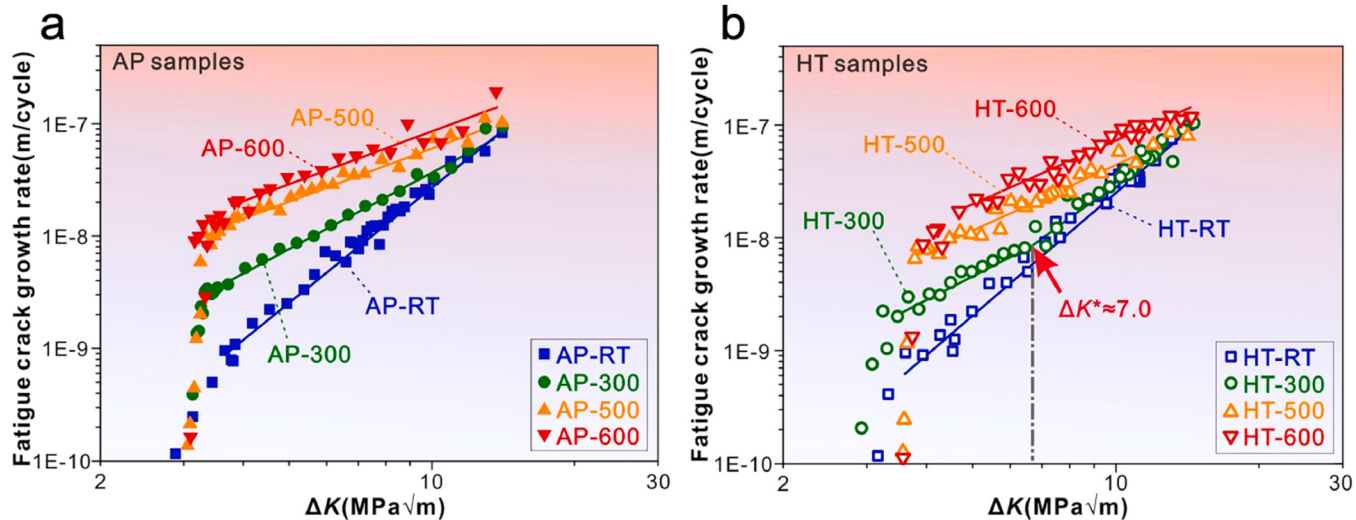


Fig. 12. Fatigue crack growth rates of L-PBF Ti-6Al-3Mo-1Zr test at $25\text{ }^\circ\text{C}$ (room temperature, RT), $300\text{ }^\circ\text{C}$, $500\text{ }^\circ\text{C}$, $600\text{ }^\circ\text{C}$ for (a) as-built state (displayed as AP), and (b) $800\text{ }^\circ\text{C}/2\text{ h}/\text{FC}$ post-AM heat treatment state (displayed as HT) [228]. The numbers in the figure indicate the corresponding test temperature.

$-150\text{ }^\circ\text{C}$, this value drops to $57.8\text{ MPa}\sqrt{\text{m}}$ and $54.4\text{ MPa}\sqrt{\text{m}}$, respectively [269]. It can be evident that fracture toughness decreases with the lowering of testing temperature, which is related to lower dislocation mobility at cryogenic temperatures (more discussion can be found in 5.3.2).

4. Defects and their influence on mechanical performances

4.1. Types of defects in AM titanium alloys

4.1.1. Internal pores

It is widely accepted that printing pores in AM titanium alloys are inevitable without any additional methods like micro-rolling. The common printing pores seen in laser-based AM of titanium alloys include lack-of-fusion (LOF) defects, keyhole porosity, and entrapped gas pores [276,277]. The process parameters, within which the most important ones are laser power, scan speed, layer thickness, and hatch distance, are considered the most substantial to the pores formation (as shown in Fig. 14a) [278]. Improper energy inputs, which could be either too high or too low, result in the formation of keyhole and LOF defects [279]. Process parameter optimization is commonly acknowledged as an important step for the elimination of these two kinds of pores. In contrast, the entrapped inert gas in the feedstock powders, mostly manufactured by gas atomization, is considered the main cause of gas pore formation in AM products, which is relatively more difficult to

eliminate using AM process control [280,281].

LOF defects, which are sometimes defined as incomplete fusion holes, are commonly characterized by large-size and irregular morphology that cause severe issues in mechanical performance (Fig. 14c) [282,284,283]. LOF defects are usually distributed between the scan tracks and the deposited layers [285]. Numerous research works have been published regarding the formation mechanism of LOF defects, which could be mostly attributed to the incorrect processing parameters that lead to insufficient energy inputs [2,286,287]. For instance, a process parameter combination of low laser power and high scan speed leads to a small melt pool width, potentially resulting in insufficient melting between the laser tracks [2]. The presence of large particles, which could be spatters or coarse powders, are hardly melted by using the optimized process parameters. This also leads to the formation of LOF defects. Titanium alloys, particularly Ti-6Al-4V, are considered more susceptible to the thermal strain generated during the AM process, and are more vulnerable to the LOF defect formation, as compared with other metals like Ni-based and Fe-based alloys [288].

Keyhole defects are also commonly found in AM titanium alloys [280]. They are spherical pores trapped at the bottom of the melt pools with relatively large diameters (Fig. 14b) [282,289]. Similar to the LOF defects, the formation of the keyhole could be related to the inappropriate processing parameters that cause excessive energy inputs into the melt pool. The keyhole depth-to-length aspect ratio can be used to indicate the keyhole defect formation [289]. It is clear that keyhole

Table 7

Cryogenic tensile properties of AM Ti alloys, and compared with those of conventionally manufactured Ti alloys.

Material	AM Method	State (i.e. treatments and testing directions)	Testing temperature (°C)	Yield Stress (SD, MPa)	Ultimate Tensile Stress (SD, MPa)	Total Elongation (SD, %)	Ref.
Ti-6Al-4V	L-PBF	As-built, longitudinal	25	973 (9)	1027 (2)	16.0 (0.1)	[269]
			-50	1092 (5)	1133 (3)	15.6 (0.5)	
			-100	973 (20)	1222 (15)	13.6 (0.2)	
			-150	1314 (4)	1332 (3)	13.0 (3.3)	
Ti-6Al-4V	L-PBF	650 °C/3 h, longitudinal	25	1192	1252	11.5	[273]
			-183	1680	1724	6.4	
			-196	1730	1797	4.6	
			-253	-	1968	-	
Ti-6.5Al-2Zr-Mo-V	L-PBF	As-built, transverse	25	1103 (7)	1281 (17)	6.3 (0.4)	[271]
			-196	1548 (25)	1750 (8)	5.2 (0.1)	
Ti-5Al-2.5Sn	L-PBF	As-built, longitudinal	25	1041	1078	13.4	[89]
		As-built, longitudinal	-196	1401	1477	12.6	
		850 °C/2 h/FC, longitudinal	25	903	945	15.9	
		850 °C/2 h/FC, longitudinal	-196	1374	1455	13.1	
		850 °C/4 h/FC, longitudinal	25	877	918	17.9	
		850 °C/4 h/FC, longitudinal	-196	1311	1390	17.2	
		HIP (850 °C/120 MPa/2 h), longitudinal	25	883	927	15.1	
		HIP (850 °C/120 MPa/2 h), longitudinal	-196	1420	1498	12.5	
		HIP (925 °C/170 MPa/3 h), longitudinal	25	-	693	20.5	[17]
		HIP (925 °C/170 MPa/3 h), longitudinal	-196	-	1127	19.5	
Ti-3Al-3Mo-3Zr-0.2Y	EB-PBF	HIP (925 °C/170 MPa/3 h), longitudinal	-253	-	1500	10.9	
		HIP (925 °C/170 MPa/3 h) + 910 °C/1 h/FC, longitudinal	25	-	654	21.9	
		HIP (925 °C/170 MPa/3 h) + 910 °C/1 h/FC, longitudinal	-196	-	1099	29.5	
		HIP (925 °C/170 MPa/3 h) + 910 °C/1 h/FC, longitudinal	-253	-	1580	20.0	
		HIP (925 °C/170 MPa/3 h) + 950 °C/1 h/FC, longitudinal	25	-	648	19.5	
		HIP (925 °C/170 MPa/3 h) + 950 °C/1 h/FC, longitudinal	-196	-	1090	29.0	
		HIP (925 °C/170 MPa/3 h) + 950 °C/1 h/FC, longitudinal	-253	-	1410	20.0	
		HIP (850 °C/120 MPa/2 h) + 950 °C/1 h/FC, longitudinal	-196	945 (5)	1090 (8)	29.0 (1.5)	[272]
		HIP (850 °C/120 MPa/2 h) + 950 °C/1 h/FC, longitudinal	-253	1160 (8)	1410 (12)	20.0 (0.7)	
CP-Ti	Rolled	As-received	25	-	519	28.7	[274]
			-80	-	679	35.4	
			-180	-	852	42.5	
			25	784 (13)	830 (23)	13.2 (2.4)	[270]
Ti-6Al-4V	Cast	HIP (900 °C/100 MPa/2 h)	-196	1237 (8)	1353 (5)	2.9 (1.2)	
			-253	1386 (27)	1544 (2)	5.9 (1.4)	
			25	859	908	13.6	[275]
Ti-5Al-2.5Sn	Rolled	As-received	-196	1344	1392	12.1	
			25	906	958	16.0	[46]
Ti-3Al-3Mo-3Zr	Wrought	910 °C/1 h/FC	-196	1266	1331	13.8	
			25	-	740	20.0	
			-196	-	1290	12.5	[47]
			-253	-	1530	4.0	

walls have fluctuations due to the collapse of the vapor cavity in high aspect ratio vapor depression, which leads to pinched-off bubbles containing the gas in the vapor chamber [280,289]. The formed bubble is ejected towards the front of solidification [290]. With the heating source moving away from the melting pool, the spherical keyhole pores are formed due to the keyhole instability, indicated by the high depth-to-length aspect ratios [291,292]. Meanwhile, the keyhole front wall angle (θ) could also be used to indicate the formation mechanism of keyhole defects in the manufacturing process [282,293]. With (θ) values exceeding 77°, large keyhole defects are formed in AM titanium alloys [278,290].

Gas pores, which mostly are small spherical holes with relatively small diameters, are currently considered inevitable defects in the AM products [280,281]. It is a bit tricky to distinguish the gas pores and keyhole pores, as both of which are spherical defects with gas entrapped. However, the gas pores have relatively small diameters and are mostly

randomly distributed. As mentioned before, the main source for gas pores in AM Ti alloys is the release of gas trapped in the powder during the gas atomization process [52,294,295]. During the printing process, due to the rapid cooling rate, the gas bubbles are unable to escape from the melting pool before solidification, and thus lead to the formation of gas pores.

Hot isostatic pressing (HIP) process is a widely acknowledged effective post-AM processing method to reduce the porosities in AM titanium alloys. The HIP processing temperatures used for AM Ti-6Al-4V are mostly below β transus in the range of 895–955 °C with the stress higher than 100 MPa according to ASTM standard F3301 [296–298], and effectively eliminate the LOF defects (Fig. 15a). However, the HIP process cannot close open pores that are exposed to the outer surface (Fig. 15b). Furthermore, some published works show that the HIP process (above β transus for L-PBF Ti-6Al-4V) could eliminate most of the pores, while some might still be retained (Fig. 15c) [299].

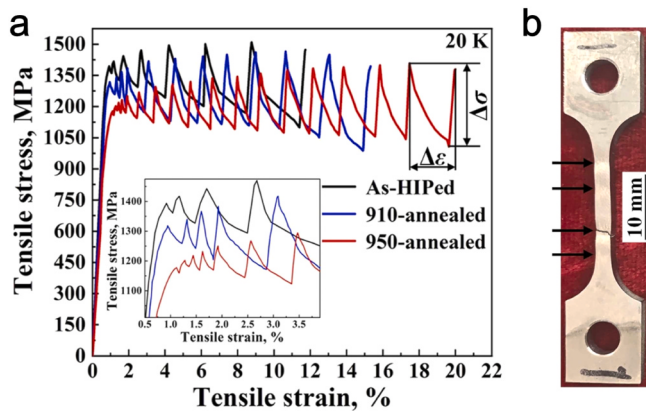


Fig. 13. (a) Tensile curves of EB-PBF Ti-3Al-3Mo-3Zr-0.2Y at $-253\text{ }^{\circ}\text{C}$. (b) The corresponding tensile fractured sample shows the multiple necking [17].

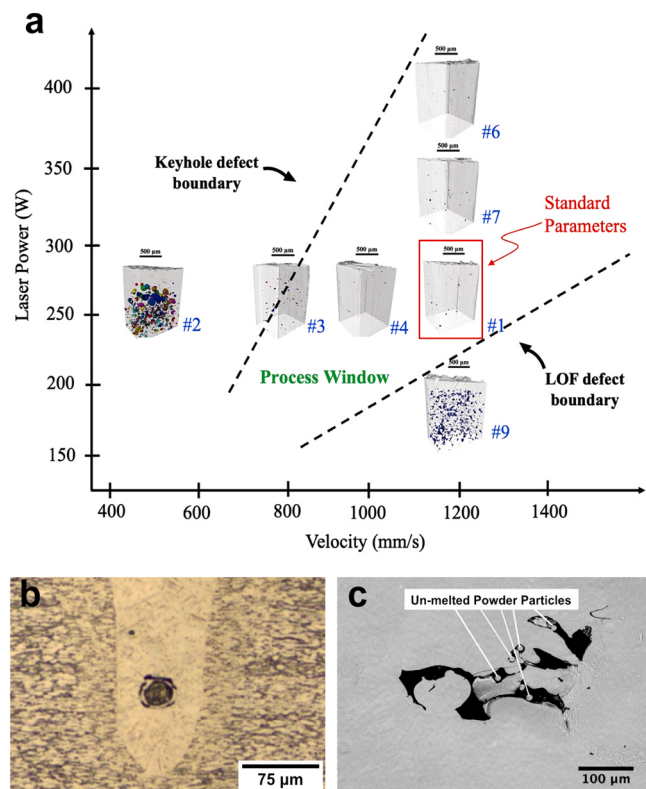


Fig. 14. (a) The correlation of laser processing parameters (laser power and scan velocity) and the defect formation in L-PBF Ti-6Al-4V [278]; (b) Optical micrograph of a keyhole in L-PBF Ti-6Al-4V-3Cu [282]; (c) Optical micrograph showing the typical LOF pores in L-PBF Ti-6Al-4V along with un-melted powder particles distributed around such pores [283].

4.1.2. Surface defects

In addition to internal defects, surface defects or surface roughness also play a critical role in the in-service performance of AM titanium alloys. These defects can result from variations in printing parameters, beam source/material interactions, and component geometry. Common surface defects in AM titanium alloys include balling and adhered particles.

Balling refers to a surface defect where the molten metal fails to form a continuous track and instead breaks up into spheroidal beads due to fluid instabilities during the melting and solidification process, as shown in Fig. 16a [300]. The severe balling even jams the powder coating process and causes the failure of the L-PBF process. The formation

mechanism of balling is mainly attributed to insufficient wetting of the layer and the surface tension [301]. Specifically, when the molten line's length-to-diameter ratio exceeds π , Plateau-Rayleigh instability induces the necking and fluctuation of the melt track, leading to discrete droplets that solidify as beads. In addition, in materials enriched with highly surface-activity elements (like S and O), the surface tension of the molten liquid could be significantly reduced, thus changing the direction of the gradient of surface tension with temperature [302]. As a result, the Marangoni flow that usually flows from the center to the edge of the molten pool is reversed and flows from the edge to the center of the molten pool. This phenomenon causes a large amount of molten liquid to gather at the top of the melt track to form agglomerates, which could lead to the formation of balling after solidification.

The formation of adhered particles is typically related to spatter during the AM process [280,289]. Spatter denotes the phenomenon in laser- or electron-beam additive manufacturing whereby molten or solid metal particles are ejected from the melt pool onto the surrounding powder bed or part surface under the action of gas recoil, melt-flow dynamics, or shock waves, as shown in Fig. 16b [302,304]. Spatter phenomenon arises from two underlying mechanisms. Firstly, the formation of spatter is related to gas-dynamic forces. Specifically, metal vaporization creates a strong recoil jet and accompanying blast wave that shoot molten or solid particles upward and forward along the beam path. On the other hand, molten liquid flowing force could also result in the formation of spatter. Marangoni convection drives liquid from the melt pool center toward its boundary, entraining larger droplets that are flung backward from the melt pool. Both mechanisms cause the spatter to fall onto the surface of the powder bed, roughening the surface. In addition, spatters with larger sizes are hard to melt by the subsequent printing process, which can result in adhered particles in the surface of final part.

The improvement of surface quality can be divided into two types: in-process treatment and post-processing treatment. For in-process treatment, printing parameter optimization is a common method to reduce balling formation. For instance, increasing the energy input can improve the wettability of the melt pool and thus suppress the formation of balling [301]. However, only optimizing laser-related (or electron beam-related) printing parameters is not enough to reduce spatter generation, due to the inherent and violent melt pool flow characteristics of AM processes. An effective way is to change the fabrication atmosphere [304,305]. For example, changing the commonly used argon atmospheres to helium can significantly reduce the formation of spatter in LPBF Ti-6Al-4V [304]. This is because high thermal conductivity and low density of helium could cool the melt pool faster and softens the vapor/plume forces, which prevent fling droplets. Recently, hybrid additively-manufacturing technology has also been considered as a promising way to enhance the surface quality of printed parts [306–309]. Its effectiveness has already been demonstrated in steel and nickel alloys and is expected to extend to titanium alloys. For instance, a hybrid AM process comprising L-PBF and three-axis milling could reduce the surface roughness for top surfaces $\text{Ra} = 9.0\text{ }\mu\text{m}$ in maraging steel, which corresponds to a reduction of 40 % as compared to pure L-PBF part [308].

For post-AM treatment, machining is still the most widespread method [302,310]. However, due to the high strength and low thermal conductivity of AM titanium alloy, conventional machining processes may not always be effective. To this end, some novel machining techniques applied to AM Ti have been developed. For instance, a hybrid dry-cutting strategy—combining minimum-quantity lubrication with CO_2 cryogenic cooling—can curb tool wear and reduce the Ra of L-DDE Ti-6Al-4 V less than $10\text{ }\mu\text{m}$ [311]. In addition, laser polishing is also an effective post-processing method. Laser polishing uses continuous or ultra-fast pulse lasers to form instantaneous molten pools on the surface layer. Surface peaks flow back under the action of surface tension and gravity to fill in depressions, thereby eliminating surface defects and reducing surface roughness. The latest multi-step or asynchronous laser

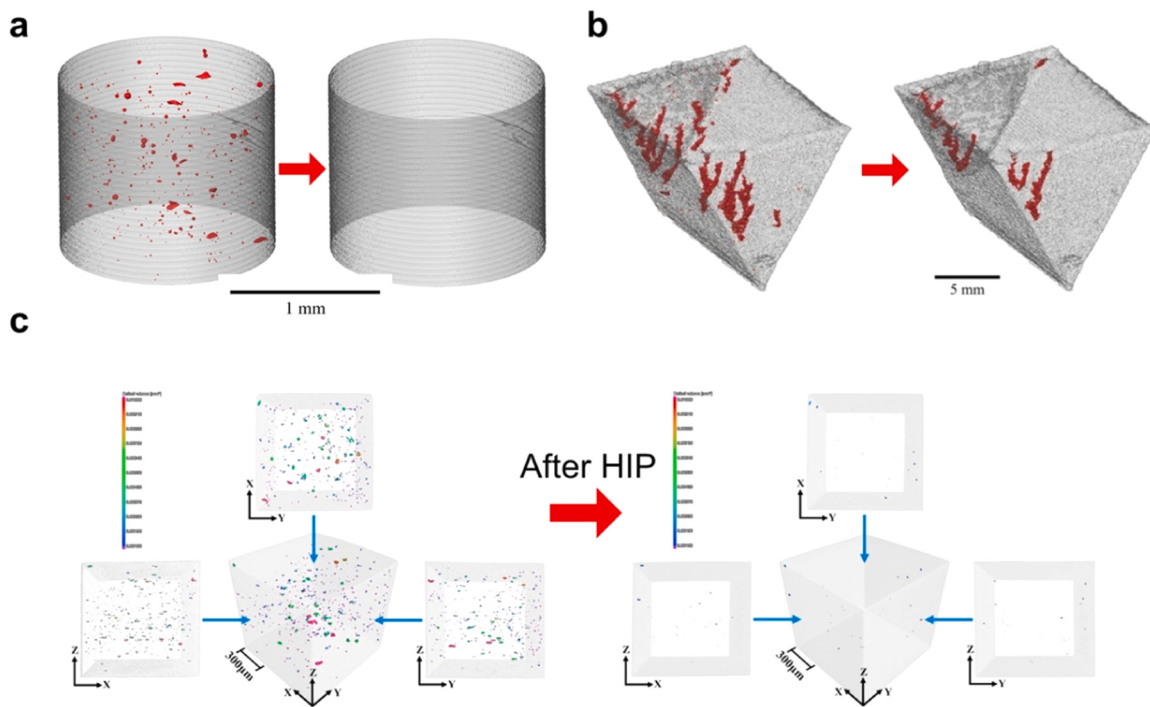


Fig. 15. The effects of the HIP process on the reduction of the pore in AM titanium alloys. (a) LOF defects fully eliminated (below micro CT detection limit) after HIP process in EB-PBF Ti-6Al-4V [296]; (b) Open defects (exposed to the outer surfaces) retained after the HIP process in EB-PBF Ti-6Al-4V [298]; (c) Retained defects identified in L-PBF Ti-6Al-4V after HIP treatment [299].

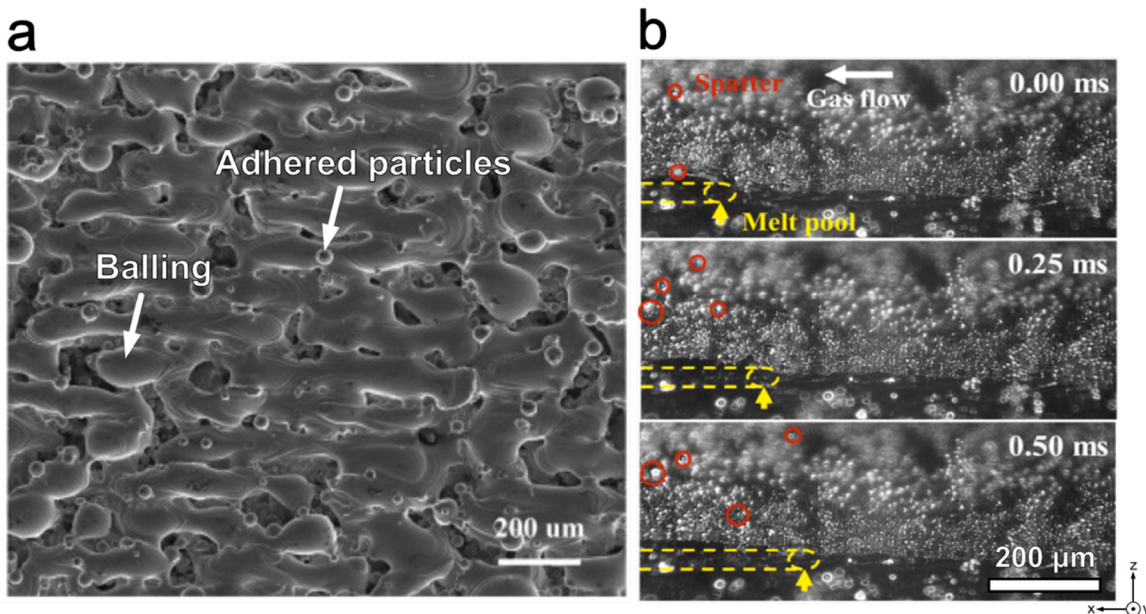


Fig. 16. Typical surface defects in AM Ti alloys: (a) SEM image shows the balling and adhered particles in L-PBF Ti-6Al-4V [303], and (b) high-speed camera images reveal the spatter formation in L-PBF Ti-6Al-4V ELI [304].

polishing strategy has reduced the Ra of L-PBF Ti-6Al-4V from approximately 30 μm to $< 5 \mu\text{m}$ [312]. For geometrically complex components containing internal channels, constrained abrasive-flow machining and plasma-electrolytic polishing can reduce surface roughness by more than 60 % [313–315]. Their material-removal mechanisms are, respectively, abrasive shear-rolling and pulsed stripping of a charged passive film. Similarly, electrochemical jet machining also relies on a localized anodic reaction [316]. A controlled electrolyte jet dissolves only the protrusions of the surface, achieving micro-scale flatness

without thermal damage, which makes the process well-suited to thin-walled or weakly supported AM sheets. Additionally, shot peening is a surface quality improvement process that is widely used in industry [148,317]. This method is a mechanical surface-treatment process in which high-velocity metallic or ceramic media bombard a component, plastically deforming the surface layer to reduce the surface defect. It is clear that such plastically deformation process can also introduce significant compressive residual stresses in the near-surface of the sample. As pointed out by 3.2, this could lead to the improvement of fatigue

performance in AM titanium alloys.

4.1.3. Heterogeneously distributed phases and elemental segregation

In addition to printing pores, AM titanium alloys are also susceptible to heterogeneously distributed phases and element segregation, which is associated with the unique thermal history during the AM process (Fig. 17) [20,41,318]. The formation of heterogeneously distributed phases is mainly because the localized reheating/remelting of the AM process leads to in-situ heat treatments, which encourages the decomposition of initially non-equilibrium martensite structure or the phase transformations of metastable β phase into α phase [319–321]. On this basis, the different thermal cycles experienced at varying printing heights influence the reheating/remelting process, causing the formation of heterogeneously distributed phases along the build direction. Specifically, the bottom part close to the substrate undergoes sufficient thermal cycling, leading to most initial phases decomposition or transformation, while the thermal cycling near the top surface becomes limited and even absent, resulting in most initial phases being retained (also schematically illustrated in Fig. 17a). For instance, after the first layer solidifies, L-PBF Ti-6Al-4V undergoes a solid-state phase transformation from BCC- β to HCP- α' martensite owing to the rapid cooling rate [41]. As additional layers are deposited, the initially formed α' martensite decomposes into $\alpha + \beta$ phases during extensive thermal cycles (in-situ heat treatment process), Fig. 17a. L-PBF Ti-6Al-4V eventually exhibits acicular α' martensite on the top surface (without enough new layers, therefore fewer thermal cycles) whereas partially or fully stabilized $\alpha + \beta$ phases in the lower regions (sufficient thermal cycling) [41]. Furthermore, such heterogeneously distributed phases are not only observed in most commonly Ti-6Al-4V. L-PBF Ti-5Al-5Mo-5V-3Cr also exhibits significant heterogeneously distributed phases along the building direction: α phase, which transforms from initial β phases, could be examined in the bottom region, while it almost disappears at the top surface [20].

For β -Ti alloys, a significant concern is the tendency to produce segregation defects, which are commonly called β -flecks (or freckles), as shown in Fig. 17b [323,324,322]. β -flecks can lead to localized variations in phase stability or create regions where α phase is lacking or absent during the heat treatment [325]. When present in high volume

fractions or large sizes, β -flecks dramatically reduce low-cycle fatigue life, tensile ductility, and fracture toughness of titanium alloys (more quantitative data will be given in 4.4) [325–327]. For this reason, β -flecks are regarded as critical defects that must be controlled. The formation of β flecks can be explained by the density-driven downward-forming channel mechanism [328]. More specifically, due to the higher density of β -phase stabilizers (such as Fe, Mo, or Nb), the concentration of the β -phase stabilizers liquid continues to flow downward between the dendritic trunks during the solidification process. Once solidification is complete, β -flecks appear as stripes along the boundaries of the dendrites [329,330]. Although the inherent advantages of the AM process, like rapid cooling rate and thermal cycle, limit the formation of β -flecks, recent publications still reported the β -flecks in AM β -Ti alloys [325,331,332]. For instance, β -flecks are found in the top layer of WAAM Ti-3Al-8V-6Cr-4Mo-4Zr owing to a lack of sufficient thermal cycling [323]. In comparison, due to the extremely rapid cooling rate, β -flecks with small size (around 10 μm) can be examined in L-PBF Ti-1Al-8V-5Fe and Ti-Fe-Co-Mo alloys [333]. During the subsequent heat treatment, such micro-scale β -flecks could still result in the lack of α phase in these areas.

Successful attempts have been made to eliminate unfavorable heterogeneously distributed phases in AM titanium alloys, like in-situ alloying and printing process optimization (Fig. 18). For instance, Ti-6Al-4V with additions of pure titanium powders and Fe_2O_3 nanoparticles [41], and Ti-5Al-5Mo-5V-3Cr (a β titanium alloy) with additions of Mo nanoparticles [20] can suppress the decomposition of α' martensite in L-PBF Ti-6Al-4V, and the transformation of initial β phases in L-PBF Ti-5Al-5Mo-5V-3Cr during the thermal cycling of AM process (Fig. 18a). This is because trace element additions (including Mo and Fe) tend to stabilize the β phase and inhibit solid-state phase transformations. Another efficient approach is to introduce the interlayer pause during the AM process, that is, printing pauses for some time after each layer is completed before proceeding to the next layer (Fig. 18b) [124]. This allows for more heat dissipation from the finished layer, thereby reducing the in-situ heat treatment and heat accumulation during the AM process (beneficial for retaining the initial phase) and eliminating heterogeneously distributed phases throughout the build.

There are also two ways that can eliminate segregation defects of AM

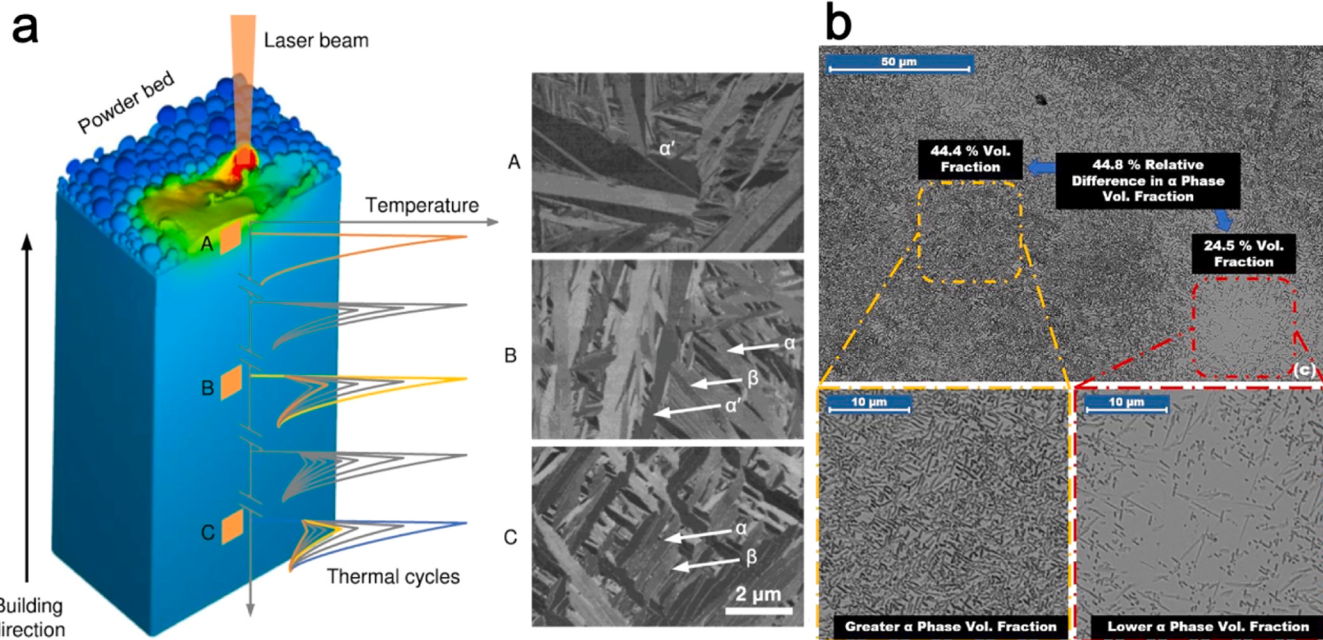


Fig. 17. (a) Heterogeneously distributed phases distribution along the building direction in L-PBF Ti-6Al-4V [41]; The β -flecks in (b)WAAM Ti-3Al-8V-6Cr-4Mo-4Zr [322].

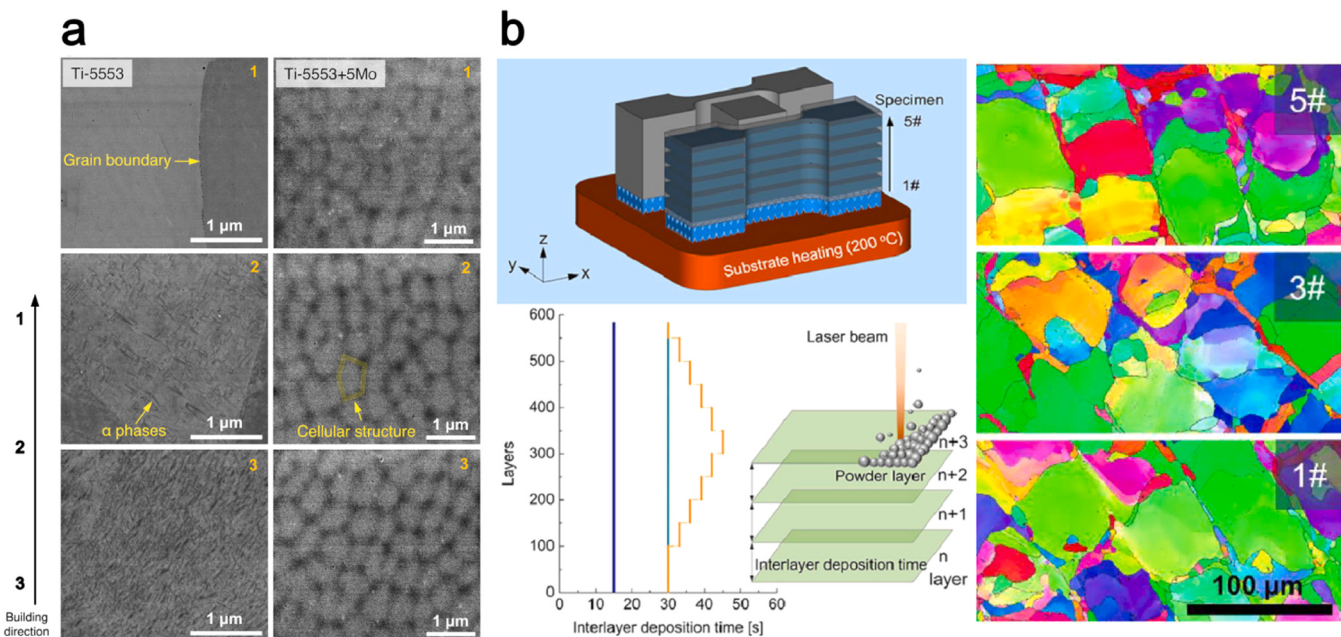


Fig. 18. (a) Back-scattered electron images show heterogeneously distributed phases (near-fully β-phase at the top area and $\alpha + \beta$ at the lower region) along the build direction (BD) in L-PBF Ti-5Al-5Mo-5V-3Cr, in contrast to the homogeneous fully β-phase microstructure of the L-PBF newly developed Ti-5553 + 5Mo alloy [20]; (b) EBSD IPF maps show that gradient interlayer deposition time strategies achieve uniform microstructure in L-PBF Ti-5Al-5Mo-5V-3Cr [124].

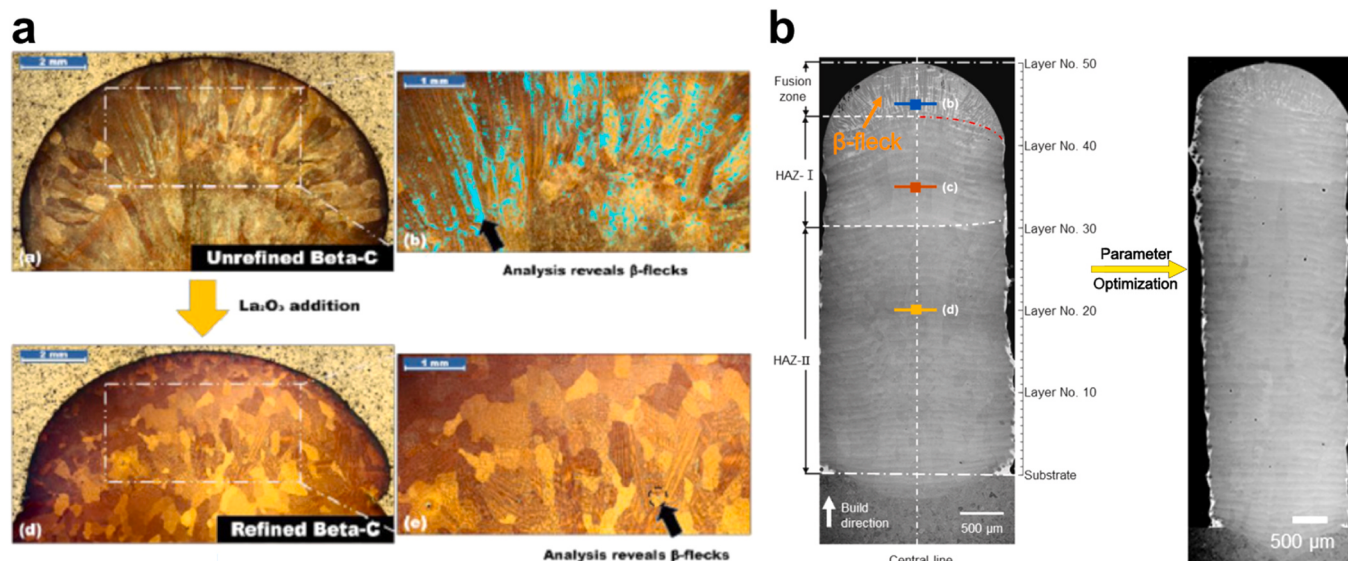


Fig. 19. (a) Adding grain refiner (La_2O_3) to the WAAM Ti-3Al-8V-6Cr-4Mo-4Zr alloy can prevent the formation of segregation defects [322]. (b) Enhanced in-situ heat treatment of AM process by parameter optimization to partially suppress the appearance of segregation defects [324].

titanium alloys (Fig. 19). The first is to introduce trace grain refiner (such as La_2O_3) to β titanium alloys since nucleation events tend to occur on grain refiner sooner during the solidification (Fig. 19a) [322]. This prevents the solute from accumulating locally to the critical level required for β -flecks to form, thereby suppressing the formation of segregation defects. Another approach is that the thermal cycling of the printing process can be enhanced by optimizing the printing parameters (e.g. reduced layer thickness). This allows previously deposited layers to be reheated, promoting solid-state diffusion and the re-distribution of solute elements (Fig. 19b) [323,324]. It should be noted that this approach only results in a partial reduction in solute variation (i.e., element changes between each layer are minimized) [323,324]. However, this reduction is sufficient to facilitate the healing of β -flecks and to

ensure that the alloy's microstructure remains consistent during subsequent aging treatments.

4.1.4. Residual stress and distortion

In most cases, including the AM process, residual stresses are generated from three sources, that is mechanical stress (caused by shrinkage of material), thermal stress (due to thermal gradient), and structural stress (because of solid-state phase transformation) [335, 336]. Specifically, during the AM process, the large temperature gradient and the rapid cooling within the melt pools, coupled with the 'bottom-up' characteristics (point-by-point, line-by-line, and layer-by-layer) and the phase transformation during the complex thermal cycles process, contribute to the non-uniform thermal expansion

and contraction of solidified material [337–339]. Therefore, AM metallic components (not limited to titanium alloys) mostly have significant residual stress in the as-built state. Such high residual stresses often lead to ‘build failure’ (distortion/delamination/cracking) in the parts (Fig. 20a-b) and unexpected mechanical performance like low ductility and poor fatigue performance [340–342]. In particular, high residual stresses generated during the L-PBF process can lead to the distortion of the part, which may be sufficiently severe to prevent the recoater from depositing a new layer of powder across the powder bed (Fig. 20a). This directly leads to build failures and even safety issues that damage the L-PBF system. For these reasons, residual stress is among the most crucial concerns in the field of AM, and needs to be properly controlled in most cases.

It is commonly acknowledged that the tuning of processing parameters, like energy input, scan speed, and layer thickness, influences the thermal history of the AM process and therefore affects the residual stress formation [345,346]. Excessive energy inputs, which is achieved by increased heat source power and slower scan speed, are commonly considered a pathway to reduce residual stress in AM fabricated components [317,347]. This is because the higher heat inputs can induce a larger melt pool, and therefore reduce the cooling rate of the AM process. For instance, increasing laser power from 100 W to 300 W (other parameters consistent) can decrease the residual stress from 600 MPa to 350 MPa in L-PBF Ti-6Al-4V [348]. Moreover, further studies also show that introducing a remelting strategy (laser scanning twice with the same slice data) effectively reduces residual stress, which is achieved by lowering the temperature gradient [349].

The substrate temperature used during the AM process is another critical process parameter that affects the residual stress formation, as higher substrate temperature certainly reduces the thermal gradient between the deposited layer and lower the cooling rates [153,317]. This results in the residual stress in components processed by EB-PBF—a process capable of maintaining substrate and ambient temperatures at approximately 1100 °C—being significantly lower than that in parts produced using other AM techniques. [153]. However, substrate heat temperatures of most commercial L-PBF systems are limited to 300 °C, since high temperatures pose a challenge to powder oxidation and the machine component, and even lead to safety issues [350]. It is clear that a 300 °C substrate can only relieve the residual stresses of L-PBF metallic with low melting points (like Al alloys), while little success with high melting points alloys, such as Ti alloys and nickel alloys. For instance, platform temperatures of 200 °C effectively prevent distortions in L-PBF AlSi10Mg [351]. In comparison, by increasing the substrate temperature from 100 °C to 300 °C, the residual stresses in L-PBF Ti-6Al-4V remain almost constant [352].

Even though the residual stress formed during the AM process could be detrimental to the mechanical integrity of fabricated components, there are now numerous approaches like adding support structures that properly overcome this issue [353,354]. The purpose of the support is to mitigate distortion caused by residual stresses and to enhance the stiffness of components, thereby ensuring stability throughout the AM. Nevertheless, reliance on support structures is only a temporary solution, which results in longer production and post-processing times, as well as materials waste with their removal [355]. Meanwhile, for parts with internal structures, the support cannot be physically accessed during post-AM processing. Such support structure may therefore remain within the part, adversely affecting its performance in service.

Proper post-AM heat treatment is also an effective post-processing method that can eliminate the residual stress of the L-PBF part [356, 357]. For instance, after post-heat treatment at 650 °C for 4 h, the residual stress in L-PBF Ti-6Al-4V can be decreased from 143.6 MPa to 21.5 MPa [352]. Yet, heat treatments are useless for cracking or distortions that have already happened during the L-PBF process. In the meanwhile, the relief of residual stress during the heat treatments may lead to deformation of the part and thus reduce accuracy.

4.2. Effects of porosities

As mentioned in Section 3, the presence of printing pores, especially the lack-of-fusion (LOF) pore and keyhole pore, could be detrimental to both room and elevated temperature mechanical performance, including the tensile ductility and high-cycle fatigue performance that are critical for load-bearing component design [2,153,262,358]. In contrast, for damage tolerance performance, it is generally accepted that the presence of printing pores does not have a significant effect unless porosity is large enough to interrupt fatigue crack propagation (pores size is larger than the plastic zone) [210,359].

The pore physical characteristic parameters, including porosity, size, distribution, orientation, and location, all have influences on the tensile behavior [360,361]. High porosity levels (exceeding 1.0 %) are particularly detrimental, since they can promote brittle-type fractures (Fig. 21), significantly reducing tensile ductility [96,97,55]. Similarly, the pores size is also crucial, as the large pores in AM Ti alloys are the crack initiation sites and also lead to very low ductility [362–364]. The alignment of the pore elongation direction (i.e. the longest axis) regarding the loading axis is another important porosity characteristic parameter, which introduces tensile property anisotropy [158,365]. To be specific, porosity with the elongation direction perpendicular to the loading axis is the most detrimental due to the opening loading mode, which refers to the stress pulling of the pores and causing the easy

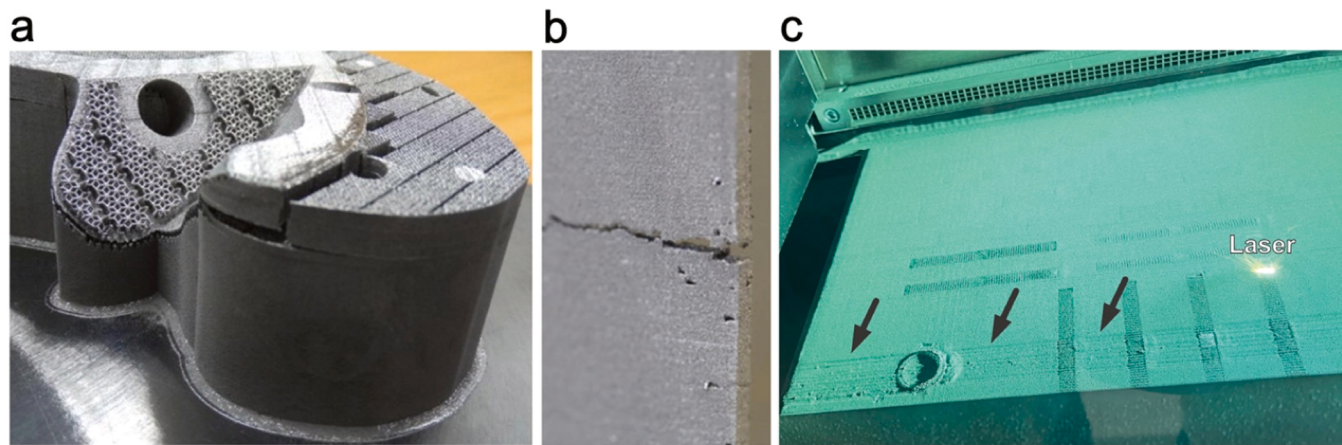


Fig. 20. ‘Build failure’ caused by residual stress: (a) delamination of L-PBF Ti-6Al-4V part [343], (b) cracking in the L-PBF Ti-6Al-4V thin-structure [344], and (c) warping of parts prevents even spreading of powder during the L-PBF process, the image was captured at the EOS M290 located at Monash Centre for Additive Manufacturing.

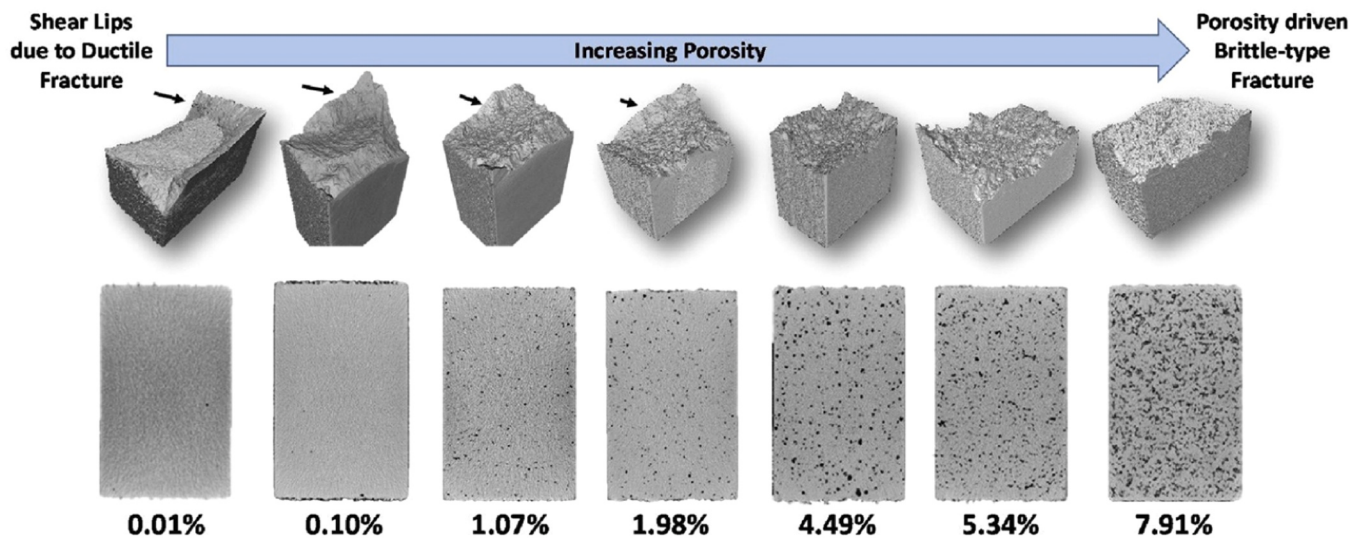


Fig. 21. Detailed μ -CT characterization of the tensile failed L-PBF Ti-6Al-4V [93]. The samples are arranged from left to right in order of increasing porosity. The number below the figure represents the corresponding porosity.

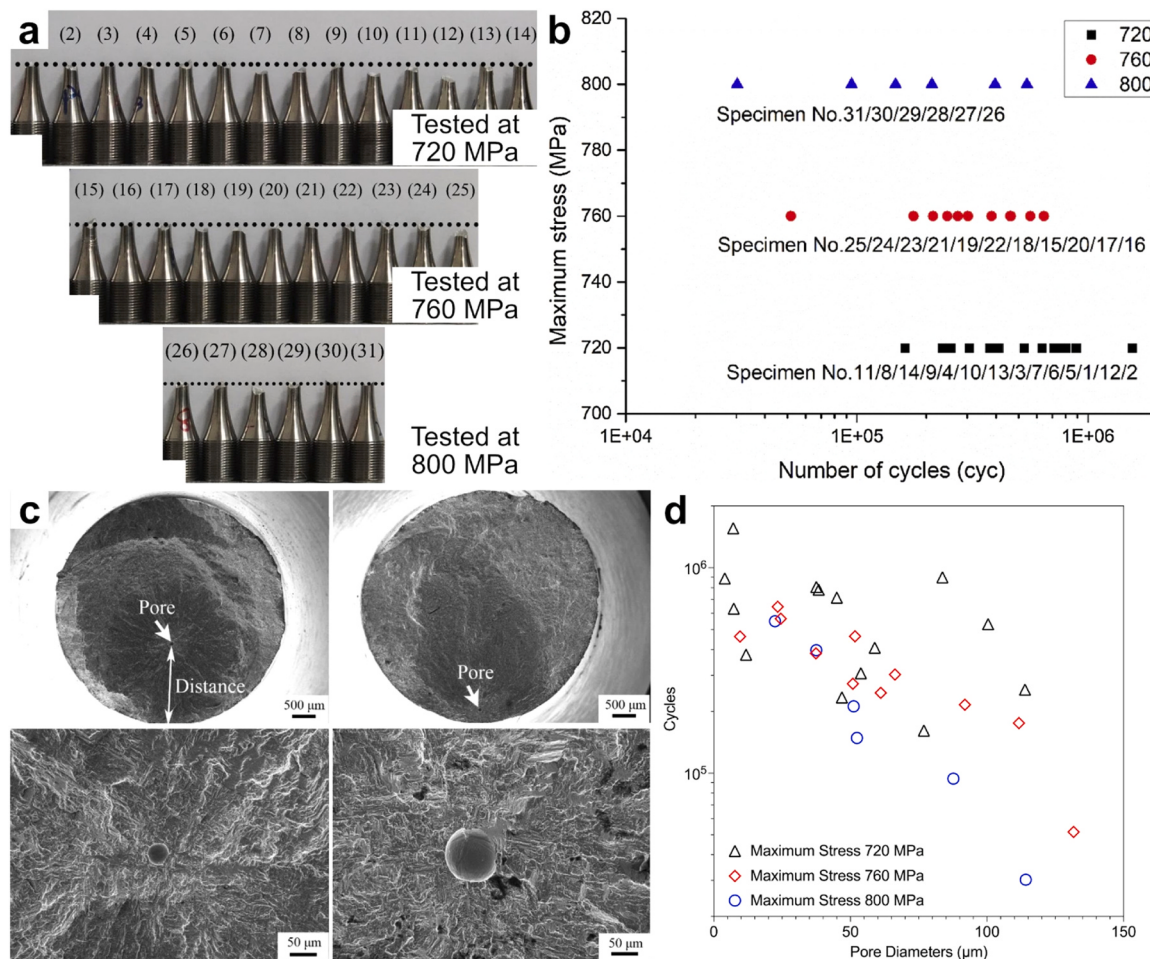


Fig. 22. Fatigue properties and fracture surface characterization of L-DED Ti-6.5Al-2Zr-Mo-V showing that the presence of random defects in different samples cause the inconsistent fatigue performance with the stress ratio 0.06 [172]. (a) Failed fatigue samples of L-DED Ti-6.5Al-2Zr-Mo-V tested at three stress levels (720 MPa, 760 MPa, and 800 MPa). (b) Stress versus cycles plotting of L-DED Ti-6.5Al-2Zr-Mo-V. (c) Fracture surface characterization shows the varied pore sizes and locations in different fatigue-failed samples. (d) Inconsistent pore sizes cause different fatigue properties of L-DED Ti-6.5Al-2Zr-Mo-V with the same processing parameters.

delamination [93,365]. Furthermore, short interspacing between the neighbored pores makes it easier to coalesce during the tensile necking process, which leads to rapid failure.

Compared to the tensile performance, the high-cycle fatigue property of AM titanium alloys is considered very sensitive to the presence of pores (as summarized in Section 3) [22,172,277,366,367]. The random and unpredictable occurrence of the pores in the testing samples, even in the AM titanium alloys from the same build batch with optimal processing parameters, contributes to the large scatters in high-cycle fatigue properties, which easily reach an order of magnitude difference (Fig. 22a) [145,147,149,151,172,174]. Since fatigue performance is one of the most critical mechanical properties of titanium alloys, numerous attempts to fully quantify the effects of pores on the fatigue performance of AM titanium alloys are made. The effects of porosity on the fatigue life of AM titanium alloys largely depend on the different pore characteristic parameters (like pore size, location, morphology, and distribution), which are complex and still difficult to make a property clarification based on the up-to-date published works [21].

Effective pore defect size is one of the primary parameters commonly used to attempt quantifying the effects of pore defects on the high-cycle fatigue performance and is commonly calculated from the square root of the pore defect projected area on the plane perpendicular to the loading axis [172,368,369]. Methods of quantifying the effective size on defects with different characteristics, i.e. pores with different morphologies and neighbored pores with different distances, are proposed in the literature and could be used for different types of pores in AM titanium alloys (Fig. 23a and b) [370].

However, correlating effective defect size with the fatigue life of AM titanium alloys is difficult with great uncertainties [172,368]. The pore location, especially the distance between the defect and the free surface, affect the high-cycle fatigue performance as well [172,283]. The surface

pores are found more detrimental to the mechanical behavior since they generate higher stress intensity [368,371]. The correlation of the pore depth (defined as the average distance of the pore top and bottom ends to the sample surface) and high-cycle fatigue performance further shows that the surface and sub-surface (with the distance to the surface $\leq 300 \text{ mm}$) pores are more detrimental to the fatigue performance comparing with the internal pores (Fig. 23c) [372]. These findings indicate that the random pore location cause larger fatigue property scatter, along with the varied pore sizes and morphologies.

Furthermore, the pore type (or shape as more commonly used in the published literature) is another important factor that influences the fatigue performance [369,372]. The fatigue performance of samples with elongated pores is obviously lower than that with equiaxed pores [372]. LOF defects, which normally have sharp edges with large aspect ratios, are considered as the most detrimental defects in AM titanium alloys, as strain tends to accumulate on the sharp edges and accelerates the crack initiation process [61,372]. On this basis, through the assumption of considering the pore defects as existing cracks, a modified Murakami's equation (Eq. 1), which could be used to calculate the stress intensity factor of a defect, has been proposed to quantify the effects of pore sizes and locations on the high-cycle fatigue performance [371,372]:

$$\Delta K = C \times \Delta\sigma (\pi \sqrt{\text{area}}) \quad (1)$$

where ΔK is the effective stress intensity, $\Delta\sigma$ is the stress amplitude, $\sqrt{\text{area}}$ is the effective defect area, and C is a constant related to the defect location [372]. Since the pore defects in AM metallic materials are mostly irregular-shaped, the effective defect area is corrected as approximately 1.137 times of the actual pore area, while the pore location related constant C is 0.5 for internal defects and 0.65 for surface defects [370–372]. Effective stress intensity value, ΔK , has been shown to correlate fatigue life well in AM Ti-6Al-4V, for both as-built and

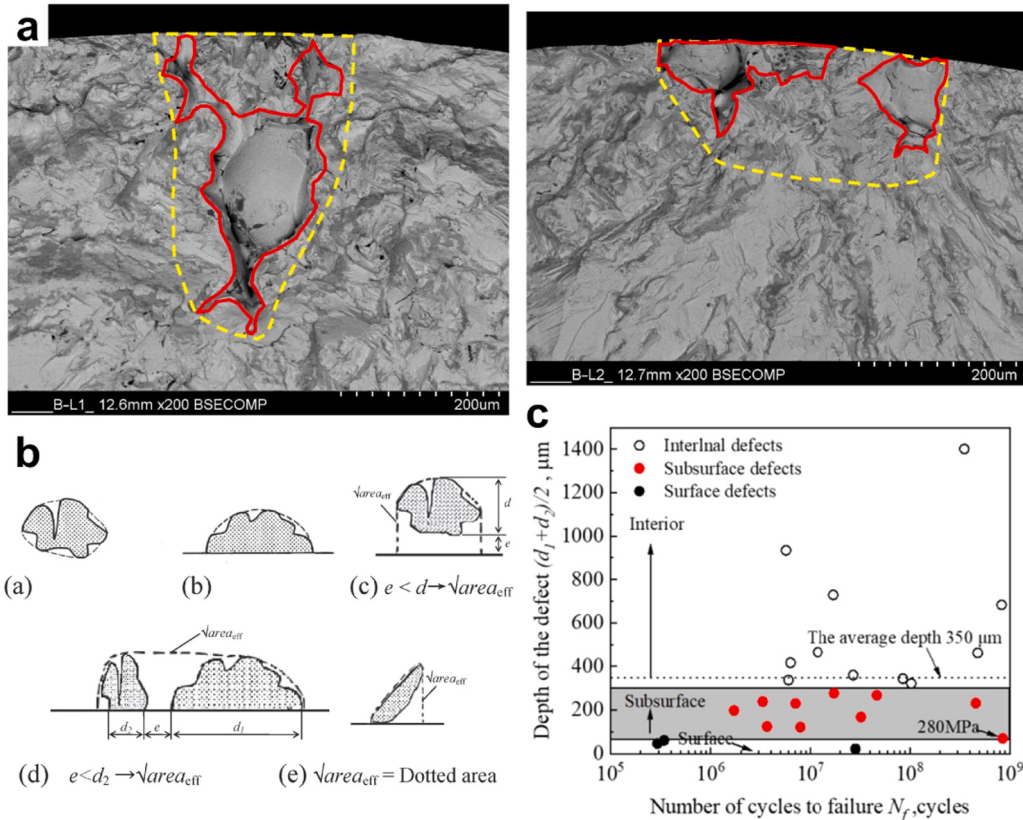


Fig. 23. The detailed characterization of various effective defect area and defect depth. (a) Dashed line marking the effective areas of different pores identified on the fracture surfaces of fatigue failed samples [370]. (b) Proposed effective area calculation methods for the defects with different characteristics [370,371]. (c) The relationship between the defect depth and the fatigue performance of L-PBF Ti-6Al-4V [372].

heat-treated states: as the ΔK value increases, the fatigue life gradually decreases [373].

However, many pores—especially lack-of-fusion (LOF) defects—are elongated with sharp edges and often occur near free surfaces. For such non-spherical and near-surface defects, $\sqrt{\text{area}}$ alone may underestimate severity, and the empirical constants (location-related constant C , 1.137) may require recalibration [374]. To this end, more attempts to correlate more pore parameters, including the pore shape factor and location, with fatigue properties are made. For instance, a new parameter, D value, is proposed to further quantify the interaction between the pore features and the external stress (Eq. 2) [372].

$$D = S\sigma_a(\text{area}_{\text{eff}})^{1/12}L^\beta \quad (2)$$

In this equation, S is the factor defined from the pore volume and area, σ_a is the stress amplitude during the high-cycle fatigue process, area_{eff} is an EI-Haddad constant that represent the effective crack lengths of different pores with different locations, L is the location parameter (value between 0 and 1, with surface pore higher than 0.9), β is the index indicating the high-cycle fatigue life of the material itself [372]. The correlation between the D value and fatigue life of L-PBF Ti-6Al-4V is attempted by using this equation in the same study (Fig. 24). A reasonably good fit between the D value and the fatigue life can be identified: for both internal and subsurface porosity, with the increase of D value, the fatigue performance of AM Ti alloys decreases significantly. In the meantime, the introduction of D value enhances the accuracy of assessing the influence of defects on fatigue performance [372,374]. For example, for two defects with comparable $\sqrt{\text{area}} \approx 45 \mu\text{m}$, applying Eq. (1) with $C=0.5$ for an internal equiaxed pore and $C=0.65$ for a near-surface elongated LOF defect gives $\Delta K \approx 22.3$ vs 29.2 (ratio ≈ 1.3), implying only a modest severity difference [372]. In comparison, when morphology and location are introduced via Eq. (2) with representative values $S=1.0$, $L=0.20$ (internal) and $S=2.5$, $L=0.95$ (LOF), the corresponding severity ratio becomes ~ 5.5 , matching the markedly shorter life of elongated, near-surface defects.

In addition, a stress state sensitive parameter (Σ), formulated by using location factors, projected area along the load direction, circularity of pores, and peak stress, was introduced to enhance the precision of the fatigue performance prediction model [374]:

$$\Sigma = \sigma' \max \times \sqrt{\delta} \quad (3)$$

Where $\sigma' \max$ is the nominal peak stress on the section containing the pore, and δ is geometry-sensitive parameter that can be described by:

$$\delta = \sqrt{\text{area}} \times f^\beta \times \omega^{-c} \quad (4)$$

In this equation, $\sqrt{\text{area}}$ is the effective defect area, f is a location factor that scales with the normalized distance to the sample surface and

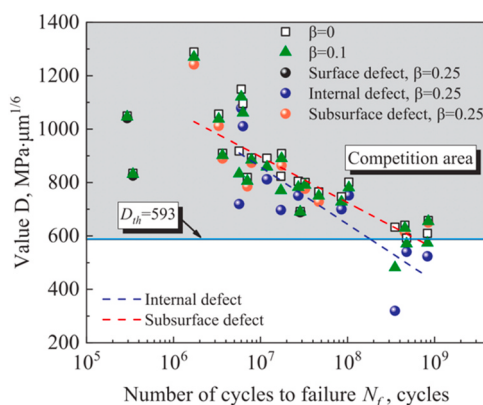


Fig. 24. The correlation between pore defect parameter D value and the high-cycle fatigue life cycles [372].

rises sharply as the distance close to 0 [374], and ω is a shape descriptor, circularity. The exponents b and c are constant. In L-DED Ti-6Al-4V alloy, using Σ in a log-log regression of fatigue life versus Σ , all data fall within a factor-of-three error band with a correlation coefficient of 0.912, clearly outperforming a Murakami-type ΔK formulation (correlation coefficient of 0.614) [374]. This indicates that this criterion can accurately establish the relationship between pores and fatigue life of AM titanium alloys, addressing the limitations of Murakami equation for irregular defects.

4.3. Effects of surface defects

Similar to internal pores, surface defects also have an extremely adverse effect on the fatigue performance of AM titanium alloys, yet do not have a significant impact on damage tolerance performance of AM titanium alloys. For instance, whether in the as-built state, heat-treated state, or after HIP state, LPBF Ti-6Al-4V exhibits similar plane-stress fracture toughness and FCG rate before and after machining [375]. In contrast, at the same stress amplitude, the high-cycle fatigue strength of L-PBF and EB-PBF Ti-6Al-4V with rough surfaces could only reach 40 % of that of machined samples with smooth surfaces [156,375,376]. This is because surface defects could act as micro-notches that locally amplify cyclic loading, causing crack initiation, as shown in Fig. 25a. On this basis, if the surface roughness is used as the radius of a semi-circle (r) to determine the effective defect area ($\sqrt{\text{area}}$), the effective stress intensity (as described in Eq. 1) can also be developed to correlate surface roughness with HCF performance [377]. The fitting results in L-PBF Ti-6Al-4V indicate that using the total roughness profile height to calculate the effective defect area ($\sqrt{\text{area}}$) can correlate ΔK with high-cycle fatigue results: lower ΔK value corresponds to better HCF performance.

Due to the obvious impact of surface defects on HCF performance, surface quality improvement methods, like chemical polishing [194], shot peening [379], laser polishing [380], and abrasive fluidized Bed [381], can also lead to corresponding HCF performance enhancement by suppressing fatigue crack initiation from notch-like surface defects. For instance, HF-HNO₃ chemical polishing can optimize surface roughness of LPBF Ti-6Al-4V to $2-3 \mu\text{m}$, thereby increasing the HCF fatigue strength by roughly 30 % [194]. Another example is that laser peening and shot peening can increase the fatigue strength of LPBF Ti-6Al-4V from less than 250 MPa in as-built state to 450 MPa and 550 MPa, respectively [379]. In addition to reducing the impact of surface defects, shot peening can also introduce compressive residual stress and increased hardness close to the surface by plastic deformation, which further reduces fatigue initiation from sample surface.

4.4. Effects of heterogeneously distributed phases and elemental segregation

It is clear that heterogeneously distributed phases lead to nonuniform (building height-dependent) mechanical performance. However, as mentioned in 4.2, non-uniformly distributed porosity also leads to the highly scattered mechanical performance of AM Ti alloys, and hence the influence of porosity should be excluded before considering the effect of heterogeneously distributed phases. On this basis, limited studies only focus on the impact of heterogeneously distributed phases on hardness and tensile performance in AM Ti-alloys (these studies employed micro-CT to ensure that the built samples were dense) [20,41,382]. For instance, the hardness distribution map of L-PBF Ti-5Al-5Mo-5 V-3Cr shows that the hardness in the middle region ($> 285 \text{ HV}$) is higher compared to the top surface and bottom areas ($< 280 \text{ HV}$), Fig. 26(a) [124]. Such a hardness variation is in line with the microstructure examination, that is, a higher volume fraction of the hard ω phase and/or α phase in the middle region. Furthermore, in the common L-PBF Ti-6Al-4V, the elongation in the horizontal direction

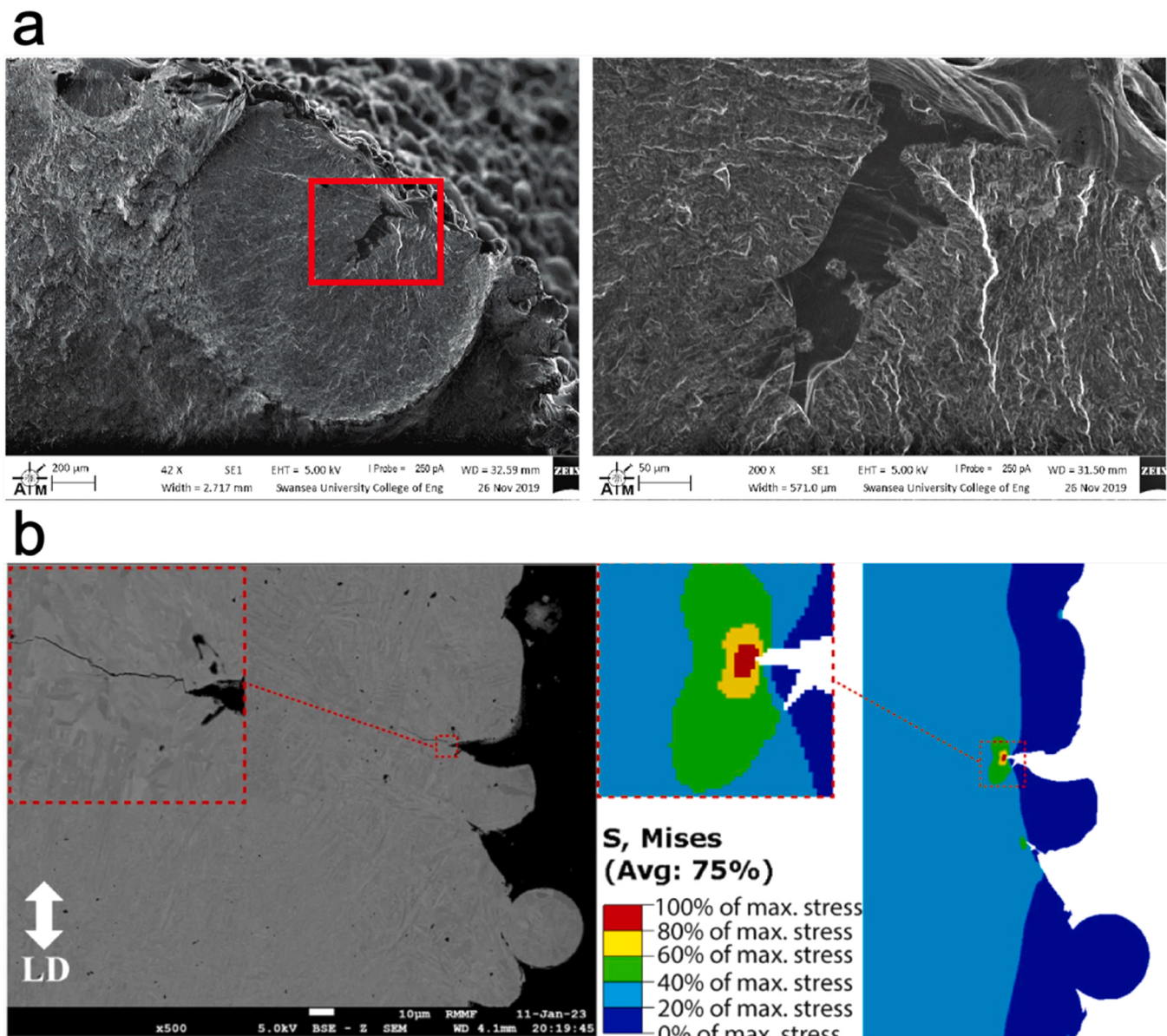


Fig. 25. (a) SEM images reveal fracture surface of EB-PBF Ti-6Al-4V at as-built state [378]. (b) SEM images of fatigue cracks initiating from surface defect, and the corresponding FE analysis results showing high stress concentration at the surface defect [377].

exhibits a significant variation, ranging from 9.4 % to 17.6 %, with the lowest value recorded at the top surface, Fig. 26(b). This trend is also consistent with the non-uniform phase distribution along the building direction (brittle α' martensite at the bottom, and lamellar $\alpha + \beta$ phase at the top region) [41].

In contrast to the well-documented effects of heterogeneously distributed phases, there are currently no published reports on the effect of β -flecks on the in-service performance of AM β -Ti alloys. This gap is mainly because the inherent thermal cycling during the printing process causes β -flecks in AM Ti alloys to occur only near the top layer, thereby limiting both their detectability and their statistical sampling needed for mechanical testing. However, this absence of reports does not mean that the volume/size fraction of β -fleck in AM titanium alloys is negligible for in-service performances. Outside the AM context, a classic study on conventionally manufactured Ti-10V-2Fe-3Al shows that even a volume fraction of β -fleck as low as 0.7 % can cause a pronounced reduction in low-cycle fatigue performance [327,383]. At a stress level of 800 MPa, the fatigue life of conventionally manufactured Ti-10V-2Fe-3Al decreases from 6.3×10^6 cycles (no β -fleck) to 8.1×10^5 cycles (0.7 %

β -fleck) [327]. By comparison, in the top region of the WAAM Ti-3Al-8V-6Cr-4Mo-4Zr alloy, the volume fraction of β -flecks was measured to be ~ 7 % [328,384], exceeding 0.7 %. Thus, the presence of β -fleck in AM titanium alloys could potentially affect the mechanical performance of AM β -Ti alloys.

4.5. Effects of residual stress and distortion

High residual stresses can pose significant challenges both during printing and in service. Cracking, distortion, and delamination (as mentioned in 4.1.3) are formed during the printing process due to the build-up of high residual stress, which directly affects the structural integrity of the part. In most cases, residual stress can be further divided into two types, i.e., compressive and tensile, which exert different influences on in-service properties [385,386]. Tensile residual stress provides an additional crack driving force, and therefore leads to lower crack growth resistance [335,346]. In contrast, compressive residual stress reduces the likelihood of crack initiation (close the crack opening) and inhibit the propagation of fatigue cracks. However, due to the

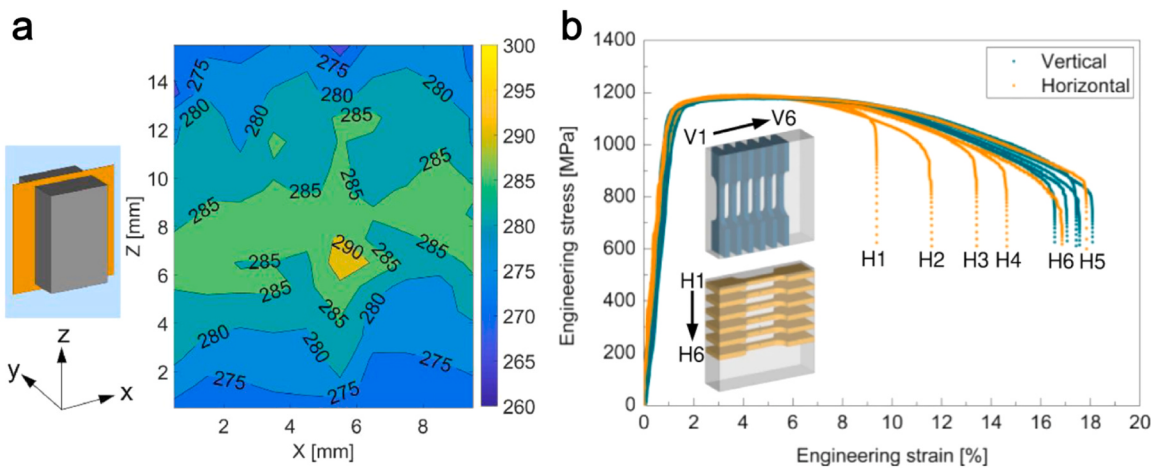


Fig. 26. (a) Hardness distribution across the xz-plane of the L-PBF Ti-5Al-5Mo-5V-3Cr (Ti-5553) part [382], and (b) Tensile curves of L-PBF Ti-6Al-4V. The inset exhibits how the tensile samples were machined from the built part [41].

localized nature of thermal cycle (heating and cooling) during the AM process, the residual stress of AM built part exhibits a highly non-uniform, which makes it difficult to evaluate the effect of individual tensile or compressive residual stress on the mechanical performance of AM Ti alloys. Thus, in this section, only the influence of the overall residual stress state has been considered.

The study of AM Ti-6Al-4V alloy shows that residual stresses play a minimal role in determining the tensile and high-cycle fatigue, while significantly influencing the damage tolerance performance (i.e., fatigue crack growth and fracture toughness). For instance, in L-PBF Ti-6Al-4V, there is no noticeable improvement in the HCF strength after stress-relief

(SR) heat treatment (the fatigue limit before and after SR heat treatment both falls within the range of 450–500 MPa) [149,197]. In contrast, high and nonuniform residual stresses in L-PBF Ti-6Al-4V cause a shift in the mean applied load during FCG testing, and lead to a highly variable FCG behavior at a low stress ratio ($R < 0.3$) (Fig. 27) [198]. This suggests that, at the low stress ratio, residual stress is sufficient to affect the driving force for crack propagation, thereby impacting the FCG behavior. Meanwhile, it is observed that the fatigue crack growth rate for both edge and vertical directions becomes largely consistent after SR heat treatment, contrasting with the significant differences present in the as-built state (Fig. 27). This reveals that residual stress is also a key

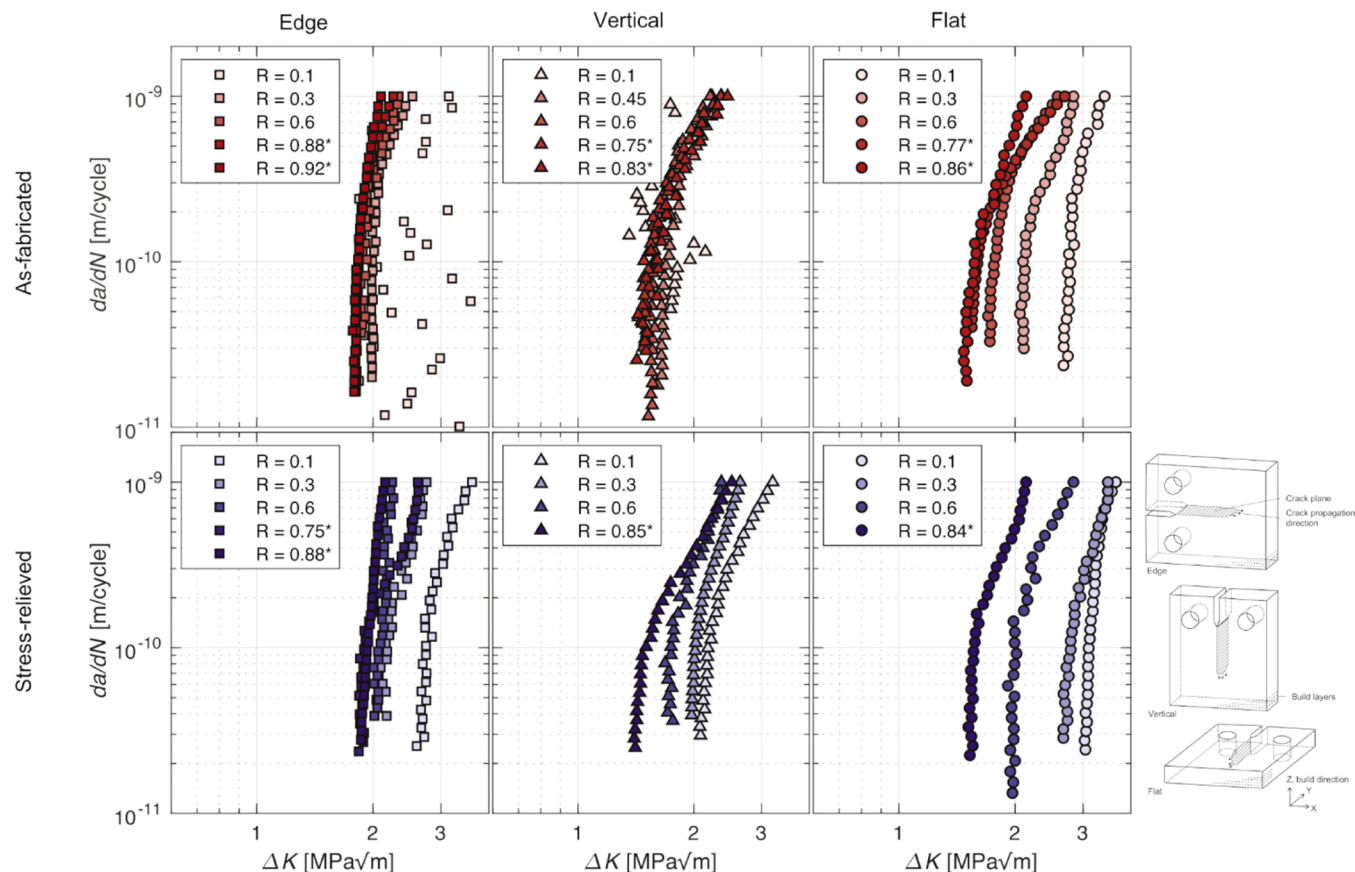


Fig. 27. Fatigue crack propagation rates of L-PBF Ti-6Al-4V in as-built and stress-relief states, tested at edge, vertical, and flat directions [198].

factor influencing the anisotropic mechanical behavior of AM Ti alloys. Similarly, another study focused on the fracture toughness of L-PBF Ti-6Al-4V found that an inverse relationship exists between residual stress and anisotropy in K_{IC} [208]. Specifically, in the as-built state with substantial residual stress, there are significant differences in K_{IC} among samples oriented in different directions (K_{IC} is $16 \text{ MPa}\sqrt{\text{m}}$ in vertical sample and $28 \text{ MPa}\sqrt{\text{m}}$ in flat sample; the definition of sample direction can be seen in Fig. 27); however, after undergoing SR heat treatment, the K_{IC} values become nearly uniform and increase substantially (K_{IC} is $41 \text{ MPa}\sqrt{\text{m}}$ in vertical sample and $49 \text{ MPa}\sqrt{\text{m}}$ in flat sample). This highlights the detrimental effect of residual stress on fracture toughness and further confirms its impact on the anisotropic behavior of AM Ti alloys.

5. Microstructure characteristics and their influence on mechanical performances

5.1. Microstructure features in AM titanium alloys

5.1.1. Grains and phases

Due to the unique thermal history during the AM process, the resulting microstructures are significantly different from those in conventionally manufactured titanium alloys, which require further investigations [2,93,387]. One typical example is columnar prior- β grains with the lengths along the building direction varying from approximately $50 \mu\text{m}$ to more than 1 cm , as shown in Fig. 28a-d [99,100,388]. Their formation is primarily attributed to the extremely high thermal gradient aligned with the build direction during the AM process [152,281]. It is commonly accepted that the presence of large columnar prior- β grains causes severe issues in nearly full-dense AM titanium alloys like strong mechanical property anisotropy and poor high-cycle fatigue performance [99,100,144], which lead to numerous researches into the microstructure refinement studies.

The additions of potential grain nucleating agents like La_2O_3 that forms ahead of titanium alloy solidification can refine the grains and

facilitate the columnar to equiaxed transition (CET). This has been confirmed in a metastable titanium alloy Ti-3Al-8V-6Cr-4Mo-4Zr processed by WAAM (Fig. 28b and c). The additions of other trace elements, like boron and silicon, have proved very effective for the prior- β grain size refinement [99,339,388]. A very small amount of boron, like 0.05 wt%, achieves CET and a very significant microstructure refinement by reducing the prior- β grain size from more than $500 \mu\text{m}$ to less than $90 \mu\text{m}$ in length by providing both sufficient constitutional supercooling and small-sized grain nucleation sites TiB particles [99].

However, end users working in fields that require extensive certification, like energy industries, hardly use the chemical composition manipulation approach for microstructure refinement in AM titanium alloys since it brings up some new issues in obtaining certifications. Thus, other approaches like high-intensity ultrasound have been developed to achieve effective microstructure refinement in titanium alloys processed by using DED (Fig. 28) [68,109,342,390,389]. High-intensity ultrasound stimulates sufficient cavitation as the grain nucleation sites due to the relatively small melt pool (compared with the ones in conventionally manufacturing), which easily achieves CET along with the refinement in the grain sizes [342]. Co-axial EB-DED, with the electron beam source and the feeding wire properly aligned with the same axis, is another newly developed AM approach that can fabricate titanium components with equiaxed prior- β grains by reducing the thermal gradient [391].

Running a roller through the top of a deposited layer (interpass rolling) by using large forces up to 75 kN , which is originally developed for reducing the residual stress during the WAAM process [68], has been shown to effectively refine prior- β grain. This is achieved by introducing plastic strains to the formed $\alpha + \beta$ microstructure below the β transus temperature, promoting recrystallization during the fabrication process [68,389]. Additionally, an in-situ rolling process, where a roller deforms the deposited laser track by following the laser nozzle, has been developed to achieve prior- β grain refinement by introducing plastic strain above the β transus temperature [109]. Both kinds of rolling processes (interpass or in-situ) effectively interrupt the epitaxial grain growth by

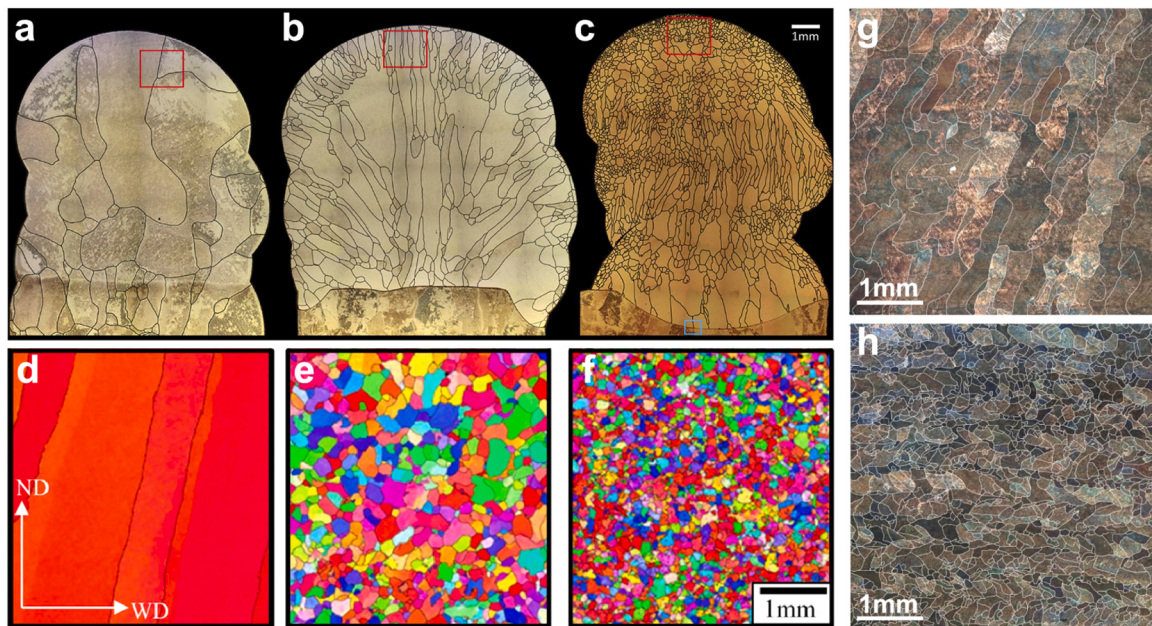


Fig. 28. Micrographs revealing the prior- β morphologies in AM titanium alloys by using different grain refinement approaches. (a)-(c) Prior- β microstructure refinement achieved through chemical composition manipulation with the optical micrographs showing the prior- β grain morphologies in (a) WAAAM Ti-6Al-4V, (b) WAAAM Ti-3Al-8V-6Cr-4Mo-4Zr and (c) WAAAM Ti-3Al-8V-6Cr-4Mo-4Zr + La_2O_3 [388]. (d)-(f) Interpass rolling for microstructure refinement in WAAAM Ti-6Al-4V as revealed from reconstructed β inverse pole figure orientation maps by using (d) no rolling, (e) 50 kN rolling force and (f) 75 kN rolling force [68,389]. (g) and (h) Microstructure refinement achieved by using high-intensity ultrasounds with the optical micrographs showing the prior- β grain morphologies (g) without and (h) with high-intensity ultrasounds [342].

introducing new orientations for new β grain growth through additional deformation [68].

The manipulation of processing parameters, including the laser power and scanning strategy, is another proposed feasible approach to achieve the columnar to equiaxed transition in L-PBF titanium alloys [22,338,392]. Alternating the laser scan directions between each deposited layer with 67° interrupt the melt pool overlap and prior- β grain boundary alignment through the mismatch of laser tracks with successive deposited layers, leading to the formation of equiaxed prior- β grains [22].

In addition to prior β grain, α laths/precipitation within prior- β grains and grain boundary α -phases along the prior- β grain boundary are also crucial microstructural characteristics that can significantly influence the mechanical properties of AM titanium alloys. Due to the rapid cooling rates (typically $10^5\text{--}10^6\text{ }^\circ\text{C/s}$ for the L-PBF process) that lead to the non-equilibrium solidification [2], the formed microstructures in AM α and $\alpha+\beta$ titanium alloys are mostly non-equilibrium, which are different from those in conventionally manufactured titanium alloys. Acicular hierarchical HCP- α' martensite with high dislocation densities and internal twins are the most commonly reported microstructures in both L-PBF α and $\alpha+\beta$ titanium alloys in the as-built state (Fig. 29a) [105,281], while α -phase and β -phase can be identified in some L-DED, WAAM and EB-PBF α and $\alpha+\beta$ titanium alloys (Fig. 29 b-d) [62,151,393–397]. Similarly, grain boundary α -phase (GB- α) is normally absent on the prior β grain boundaries in as-built L-PBF α and $\alpha+\beta$ titanium alloys, however, continuous GB- α could be examined in L-DED/WAAM α and $\alpha+\beta$ titanium alloys [67,99,398,399]. This is mainly because, for the AM process that has lower cooling rates (like L-DED and WAAM), the excessive energy inputs with thermal fluctuations introduced by the repeated heating and deposition process provide an equivalent annealing heat treatment with a short dwell time, which decompose the martensitic microstructure and lead to the formation of GB- α [400].

The presence of α phase along with the α' martensite in as-built L-PBF Ti-6Al-4V is also reported in some studies, which indicates that α' martensite could be decomposed into α phase during the L-PBF process with different thermal histories [22,402]. Detailed studies show that proper control of the L-PBF processing parameters including increasing the substrate temperature, changing the laser focal offset distance, and tuning other commonly adjustable L-PBF process parameters (like scanning speed, laser power, and layer thickness) leads to the in-situ α'

martensite decomposition and the formation of $\alpha+\beta$ microstructure [320,395]. Post-AM annealing process, which is essential for the manipulation of microstructure and commonly used at $800\text{ }^\circ\text{C}$ (or even higher) for more than 2 h [55,91], effectively decomposes the martensite into the equilibrium α -phase and β -phase [320,395]. The thickness of transformed α lath, which can be directly related to tensile strength through the Hall-Petch relationship, is determined by the applied heat treatment temperature and dwell time (Fig. 30). Specifically, high heat treatment temperature with long dwell time promotes the growth of α lath [55,91]. Theoretically, the static coarsening behavior of α lath in AM Ti alloys follows the classical Lifshitz, Slyozov, and Wagner (LSW) model [403], which provides insights into microstructure predictions in AM Ti alloys. Furthermore, since α laths with low aspect ratio enhance the tensile ductility and high-cycle fatigue performance of AM titanium alloys, numerous studies have been undertaken to achieve equiaxed α lath through post-AM heat treatment [404–406]. Generally, equiaxed α lath can be achieved by using HT with a temperature close to the β -transus and a long dwell time [67,407]. In this case, the break-up of α lath is attributed to the boundary splitting and termination migration [408–410]. Both mechanisms are based on elemental diffusion, with the former occurring rapidly at sub-boundary or shear bands within α lath and the latter happening slowly at the groove and termination tips of α lath interface. Although heat treatment close to the β -transus can effectively facilitate the break-up of α lath and thus lead to the formation of equiaxed α lath, HT at high temperatures inevitably results in rapid coarsening of the microstructure, which compromises mechanical properties (especially yield strength). To this end, cyclic heat treatment has been proposed [405,411,412]. Cyclic heat treatment schedule consists of repeated thermal cycling (generally more than ten cycles) close to, but below, the β -transus. In this process, the globalization of α is achieved through epitaxial growth, which is a more rapid break-up mechanism of α lath compared to boundary splitting and termination migration [412]. A recent study shows that cyclic heat treatment results in the reduction in the aspect ratio of α lath to approximately 2 within 10 min [405].

Grain boundary α -phase, which could be hardly noticed in an as-fabricated state, could also be easily observed in L-PBF Ti alloys after post-AM heat treatments (even if the heat treatment temperature is below the β -transus temperature). Due to the lower nucleation barrier at the prior- β grain boundaries, GB- α is considered to form before the α lath

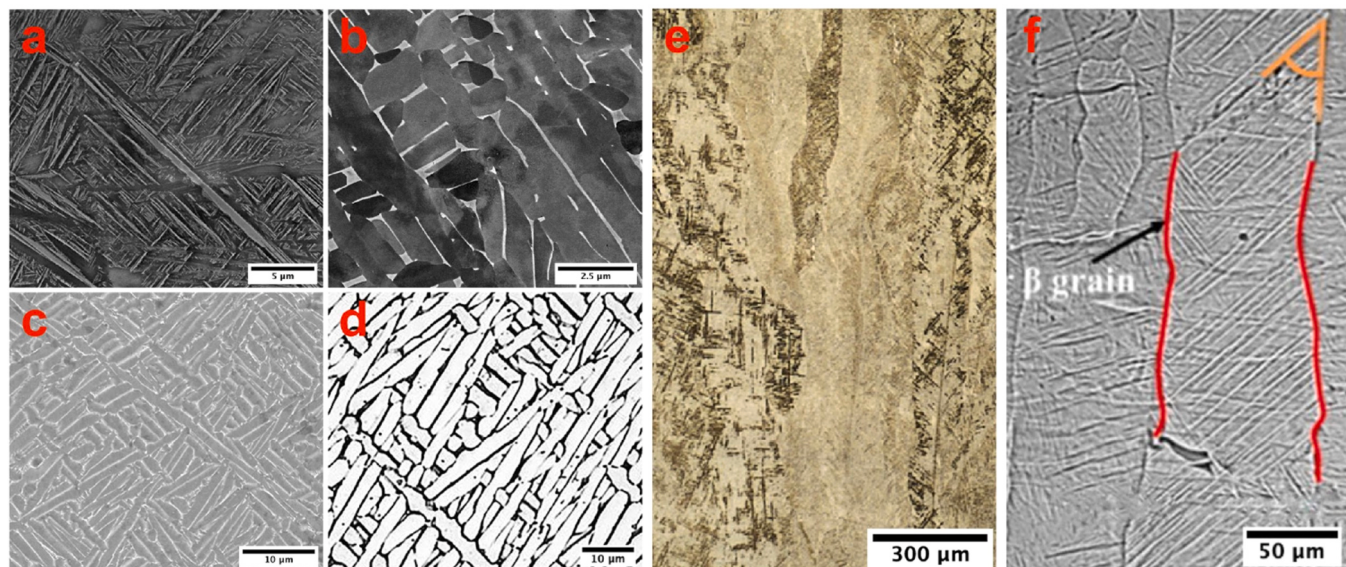


Fig. 29. SEM images of as-built Ti-6Al-4V showing (a) α' martensitic or α lath microstructure manufactured by L-PBF, $\alpha+\beta$ microstructures manufactured by (b) EB-PBF, (c) L-DED and (d) WAAM [149,394–396]. Optical micrographs show the columnar prior- β grain morphologies in Ti-6Al-4V processed by (e) EB-PBF and (f) L-PBF [396,401].

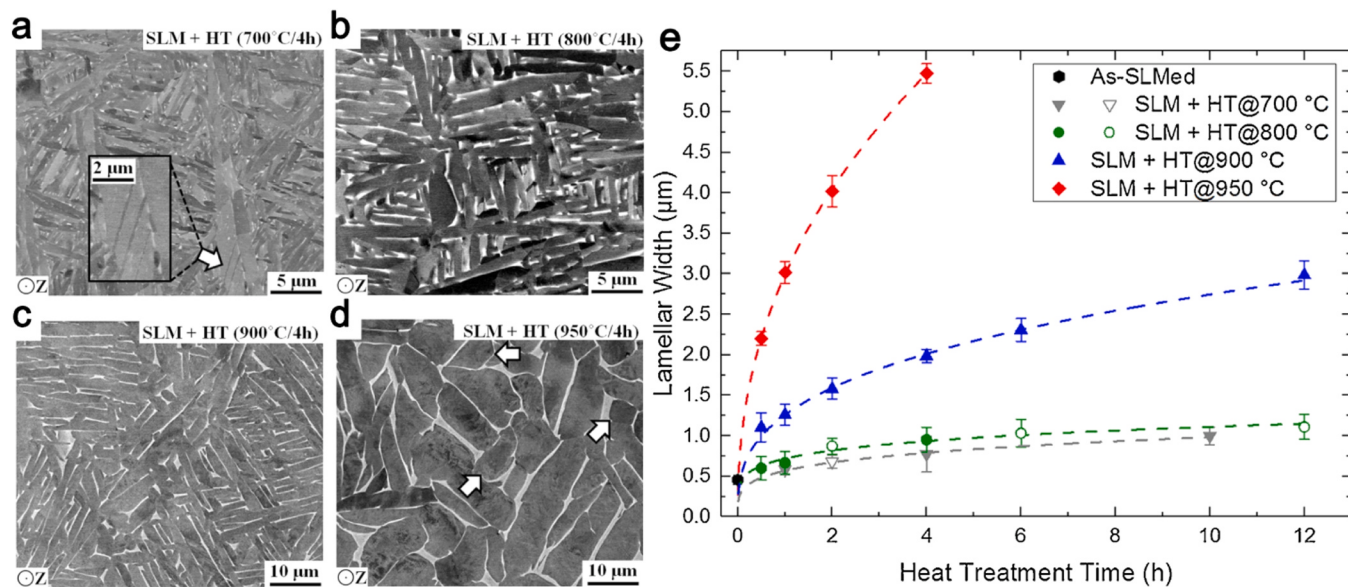


Fig. 30. SEM images of L-PBF Ti-6Al-4V after heat treated at (a) 700 °C for 4 h, (b) 800 °C for 4 h, (c) 900 °C for 4 h, and (d) 950 °C for 4 h [403]. (e) Measured thickness of α lath of various heat treated L-PBF Ti-6Al-4V [403].

precipitation [413,414]. To be specific, GB- α firstly precipitates at the triple junction locations of the high angle grain boundaries due to the high interfacial energy and deformation energy at these sites, and decorates the β grain boundaries progressively [414,415]. In the view of crystallography, GB- α commonly follows the Burgers Orientation Relationship (BOR) with one of the prior- β grains nearby. This result in more strain incompatibility between GB- α with the surrounding grains during the loading process and thus determine the mechanical performance of AM Ti alloys [416,417]. Moreover, similar to α lath, the coarsening behavior of GB- α in L-PBF Ti alloys is also influenced by the post-AM heat treatment temperature. The study on L-PBF Ti-6Al-4V shows that the coarsening behavior of GB- α is governed by bulk diffusion at the HT temperature of 750 °C, while the GB- α growth behavior transitions to the interface reaction coarsening as the HT temperature increased to 850 °C and 950 °C [416]. Meanwhile, post-AM heat treatment temperature also influences the morphology of GB- α , which is a critical parameter affecting the tensile anisotropy of the AM Ti alloys [399,418]. Continuous GB- α is normally observed in L-PBF Ti-6Al-4V after post-AM HT at the temperate between 700°C to 850°C [105,419]. In comparison, discontinuous GB- α potentially forms after HT at the temperature close to the β -transus (like 950°C for L-PBF Ti-6Al-4V), which is attributed to the fact that more transformed β phase at higher annealing temperature results in more GB- α nucleation sites [91,418].

As compared to AM α or $\alpha+\beta$ Ti alloys, due to the sufficient β stabilizers in the Ti matrix, the rapid cooling during the AM process leads to the β phase being retained as the only phase in most AM metastable- β titanium alloys like Ti-3Al-8V-6Cr-4Mo-4Zr processed by both WAAM and L-PBF, Ti-5Al-5Mo-5V-3Cr and Ti-5Al-5Mo-5V-3Cr-1Zr processed by L-PBF (Fig. 31a) [126,128,420,421]. The exception is AM near- β titanium alloys with a Mo equivalent of more than 4 wt% and less than 10 wt% (such as Ti-Nb, Ti-25Nb-3Zr-3Mo-2Sn, and Ti-6Al-2Sn-4Zr-6Mo), showing α'' martensite phases in the as-built states (Fig. 31b) [422,423]. Furthermore, varying the printing parameters also affects the microstructure of AM metastable β titanium alloys in the as-built state. For instance, with the increase of the substrate temperature (like 700 °C used in the reported study) that reduces the cooling rate, the formation of α precipitations could be identified in as-built L-PBF Ti-5Al-5Mo-5V-3Cr-1Zr (Fig. 31c-d) [128]. Precipitation of the isothermal ω phase, which was suspected to form during low-temperature heating (i.e. AM thermal cycles), could be examined in as-fabricated Ti-10V-2Fe-3Al processed by L-PBF equipped with a

modulated pulsed laser mode [338]. Moreover, GB- α can not be observed in prior β -grain boundaries of as-built L-PBF β titanium alloys, but can be observed in as-built WAAM and L-DED β titanium alloys (Fig. 31e-f). This is mainly because the faster cooling of L-PBF favors the retention of the parent β phase and thus inhibits the GB- α formation, while slower cooling rates and prolonged heat accumulation of WAAM and L-DED promote the transformation of α -phase at the prior- β grain boundaries [130,416,424].

Post-AM heat treatments are essential for the microstructure and mechanical property manipulation of β titanium alloys since the precipitated α phase, which is formed in the aging process, determines the mechanical performance [12]. Given that the single-phase β state can be retained after the rapid cooling process, efforts have been made to manipulate the microstructure of AM β titanium alloys through direct aging. Direct aging ranged from 400 to 800 °C in L-PBF Ti-5Al-5Mo-5V-3Cr shows that ω phase is suspected to form during the low-temperature aging of 400 °C with only 1 h dwell time (Fig. 32a-b) [123]. Such ω phase, which is normally formed during low-temperature heat treatments of conventionally manufactured β titanium alloys, could be used as the potential nucleation sites for the subsequent α precipitation [426,427]. With the increase of the aging temperature, the presence of α precipitation could be identified. The increase of aging dwell time leads to the coarsening of precipitated α laths and GB- α (Fig. 32a-b). Moreover, the unique thermal history and rapid cooling rate of L-PBF can impart high-density dislocations with a dominant screw character in the microstructure of as-built Ti-3Al-8V-6Cr-4Mo-4Zr alloy (Fig. 32c), which also acts as the nucleation sites for α precipitations [138]. This is attributed to the fact the local strain around the dislocation cores can significantly reduce the energy barrier for the nucleation of α precipitation [428]. For this reason, direct aging can directly introduce the dense, stable, and internally twinned α nano-precipitates into L-PBF Ti-3Al-8V-6Cr-4Mo-4Zr alloy (Fig. 32d-e). Meanwhile, because the formation of dense α -precipitates has consumed most of the α -phase stabilizer (Al and O in this alloy) in the β matrix during aging, GB- α (often formed in other AM titanium after heat treatment) is absent [138].

Similar to the conventionally manufactured high-strength β titanium alloys, the post-AM heat treatment process with multi-steps including the solution treatment (defined as recrystallization in some studies), and aging (including pre-aging) is more commonly used for the α precipitation manipulation and inhomogeneity elimination in AM β titanium

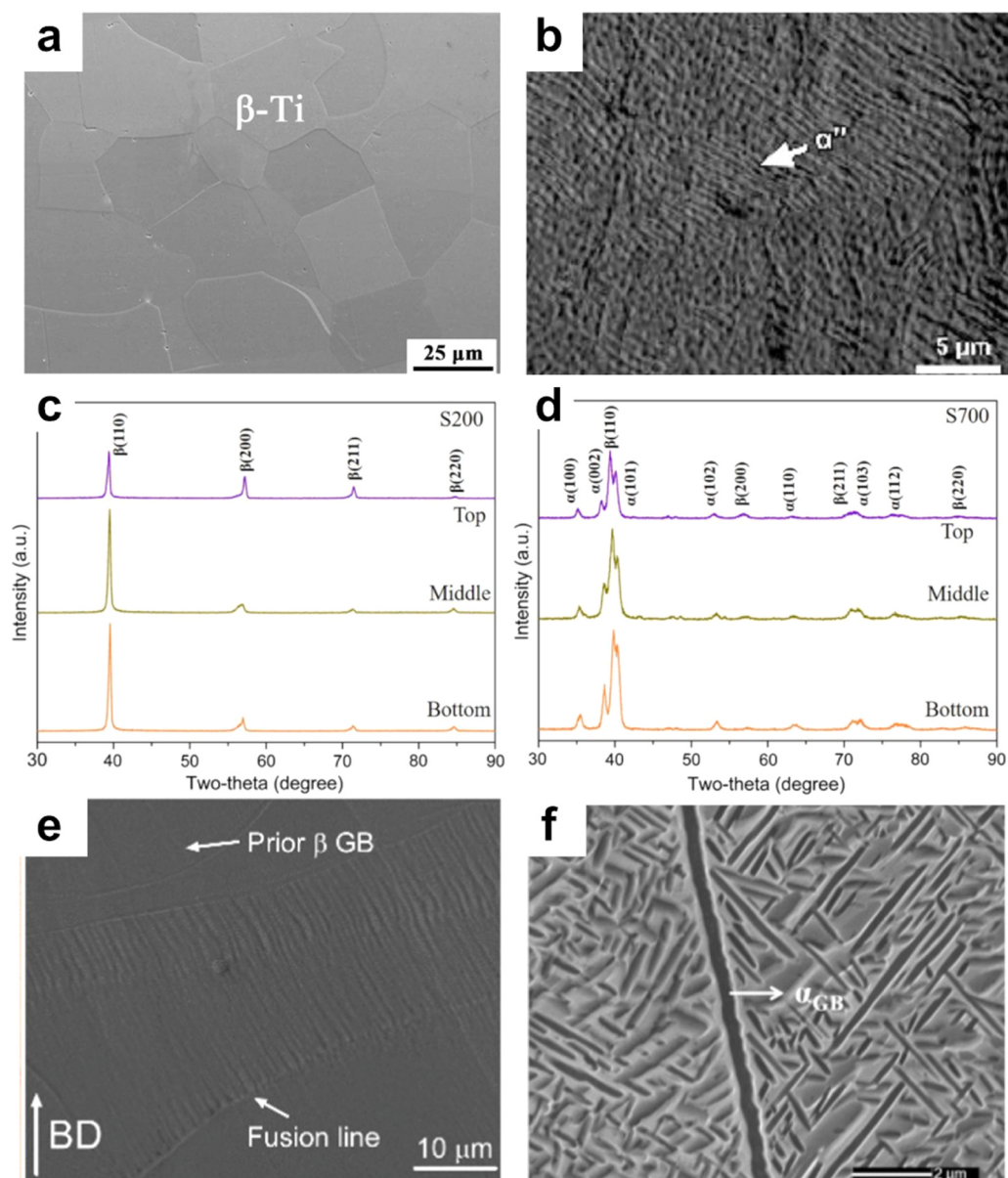


Fig. 31. SEM images showing (a) the fully β phase in L-PBF Ti-35Nb-7Zr-5Ta alloy [36] and (b) α'' martensite in L-PBF Ti-25Nb-3Zr-3Mo-2Sn [423]. XRD characterization of L-PBF Ti-5Al-5Mo-5V-3Cr-1Zr showing (c) the single β phase with 200 °C substrate preheating, and (d) the presence of both α and β phases with 700 °C substrate preheating [128]. SEM micrographs showing (e) the absence of GB- α e along the prior β -grain boundary in L-PBF Ti-5Al-5Mo-5V-3Cr-1Zr [129] and (f) continuous GB- α in L-DED Ti-5Al-5Mo-5V-1Cr-1Fe alloy [425].

alloys [12,130,134,429]. The inhomogeneous microstructure (such as α -phase or ω -phase in the as-built state) could be re-solutionized and homogenized into the matrix, preparing it for subsequent aging processes [12,429]. The solution treatment above the β transus temperature fully dissolves the metastable phases formed during the AM process, while the dwell time should be carefully controlled for the prior- β grain morphology control (Fig. 33a-c) [429,430]. A short solution treatment above β transus temperature (like 10 mins reported in [431]) leads to morphology transformation of β grains from columnar to equiaxed driven by the low-angle grain boundaries. However, the β grain growth is very rapid, so a long dwell time should be avoided to prevent excessive β grain growth. In contrast, solution treatment below the β transus temperature retains the prior- β grain morphology [430].

Triplet heat treatment (first step above the β transus temperature with short dwell time, second step below β transus temperature with slow cooling, and third step aging process) is found effective in breaking the continuous GB- α that is detrimental to the ductility, high cycle

fatigue performance, and fracture resistance [134,142]. However, the coarsening of the precipitated α laths occurs simultaneously and reduces the strength [142]. Pre-aging for the purpose of homogenizing α precipitation is also used for AM β titanium alloys, like pre-aging at 300°C for WAAM Ti-3Al-8V-6Cr-4Mo-4Zr for solute redistribution and the homogeneously distributed refined α precipitation (Fig. 33d-f) [427,429]. In this case, the precipitated α lath thickness is mostly controlled by the temperature used for the aging process [137].

5.1.2. Textures

Besides the optical microstructure parameters that include the prior- β grains, α laths/precipitation, and grain boundary α -phases in AM titanium alloys, the texture is another well-concerned microstructure parameter (Fig. 34), which is considered as another potential cause for the mechanical property anisotropy [432,433]. However, fewer research efforts have been made into the texture and microtexture in AM titanium alloys.

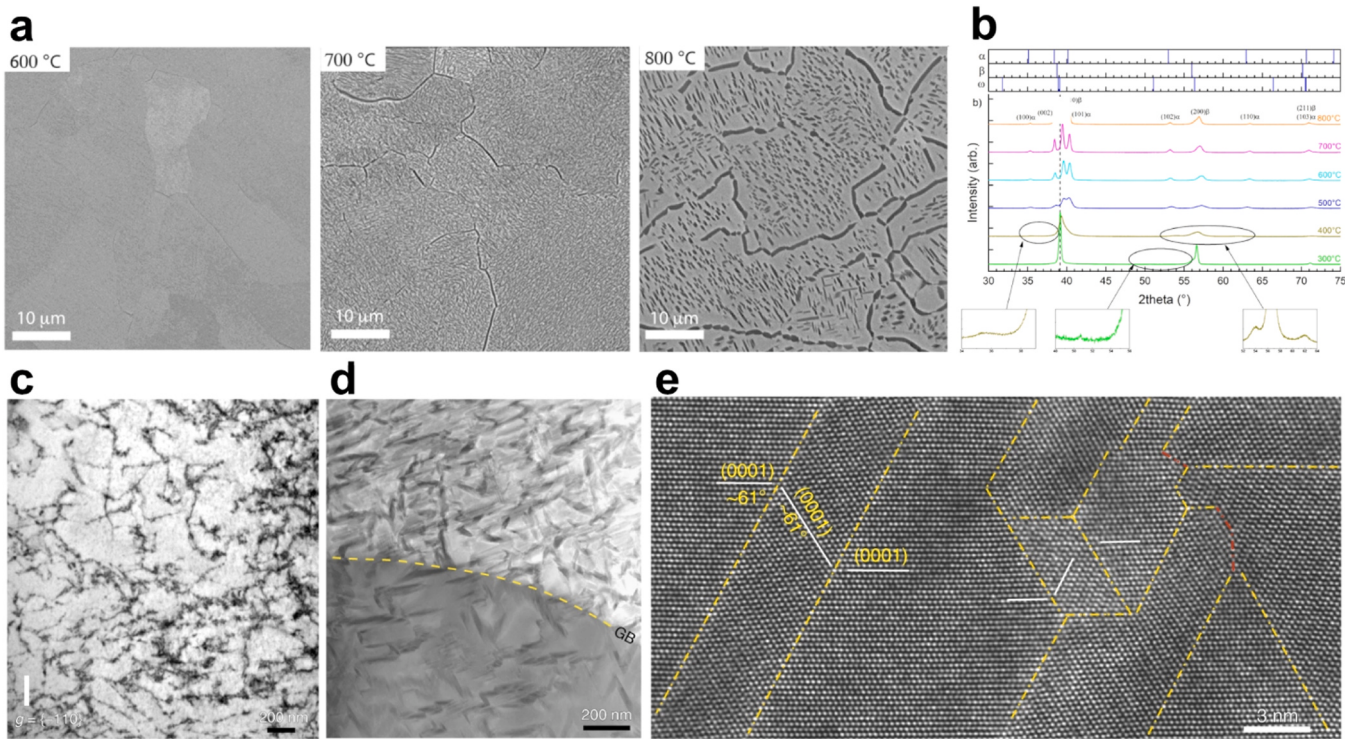


Fig. 32. (a) BSE images showing the different α precipitations in L-PBF Ti-5Al-5Mo-5V-3Cr alloy after different heat treatments of 1 h at 600 °C, 700 °C and 800 °C respectively [123]. (b) XRD characterization of L-PBF Ti-5Al-5Mo-5V-3Cr alloy after different heat treatments shows the formation of ω phase after 300 °C and 400 °C heat treatment. (c) Two-beam bright-field (BF) TEM image of L-PBF Ti-3Al-8V-6Cr-4Mo-4Zr alloy showing the high-density dislocation. (d) High-angle annular dark-field scanning transmission electron microscopy (HAADF-STEM) image shows the nanosized α -precipitates in L-PBF Ti-3Al-8V-6Cr-4Mo-4Zr alloy after 480 °C/6 h. (e) Atomic-scale HAADF-STEM image reveals internally twinned nanoprecipitates in L-PBF Ti-3Al-8V-6Cr-4Mo-4Zr alloy after 480 °C/6 h.

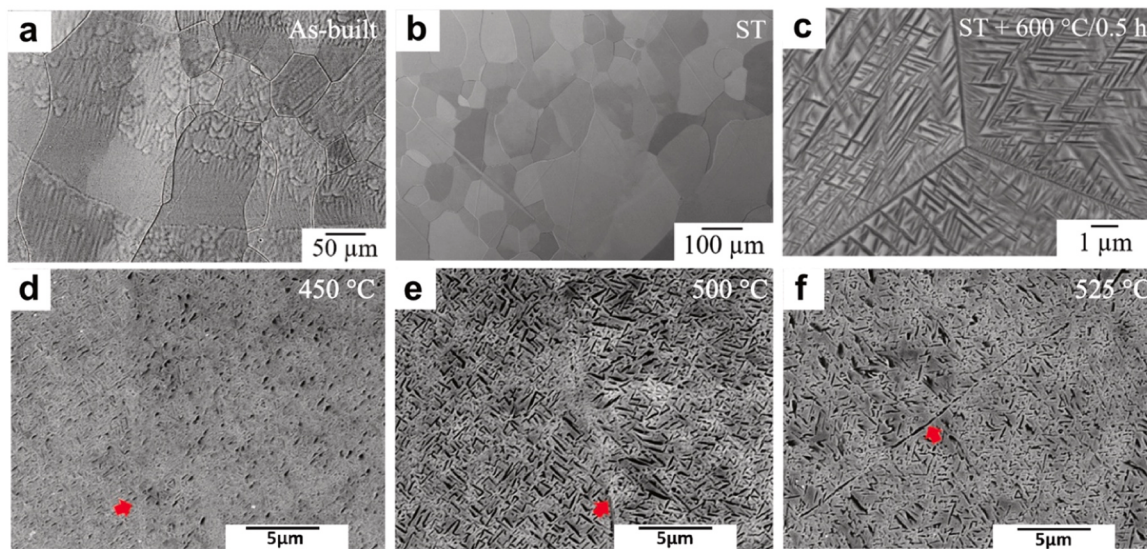


Fig. 33. SEM images showing the microstructure of L-DED Ti-5Al-5Mo-5V-3Cr in the condition of (a) as-built state, (b) solution treatment (900 °C/0.5 h), and (c) solution treatment + aging treatment (900 °C/0.5 h + 600 °C/0.5 h) [334]. (d-f) SEM images displaying characteristic microstructures of WAAM Ti-3Al-8V-6Cr-4Mo-4Zr after solution treatment of 850 °C, pre-aging of 300 °C, and aging of (d) 450 °C, (e) 500 °C, and (f) 525 °C (GB- α is marked by red arrow) [429].

Through the optical microstructure and inverse pole figure (IPF) characterization of the reconstructed β phase, it could be confirmed in the titanium alloys fabricated by EB-PBF, L-DED, and WAAM that the β phases have columnar morphologies with strong $<001>_{\beta}/N_Z$ texture (Fig. 34 and Fig. 35) [431]. As another outcome of the epitaxial grain growth, the strong solidification $<001>_{\beta}/N_Z$ figure texture commonly

forms during the cooling process with the (001) crystallographic planes of the solidified β grains aligned with the thermal direction, which is the building direction for most of the AM titanium alloys [99,431]. However, the solidification texture in L-PBF titanium alloys is weaker, which can be attributed to the faster cooling during the L-PBF process leading to less variant selection during the solidification and smaller prior- β

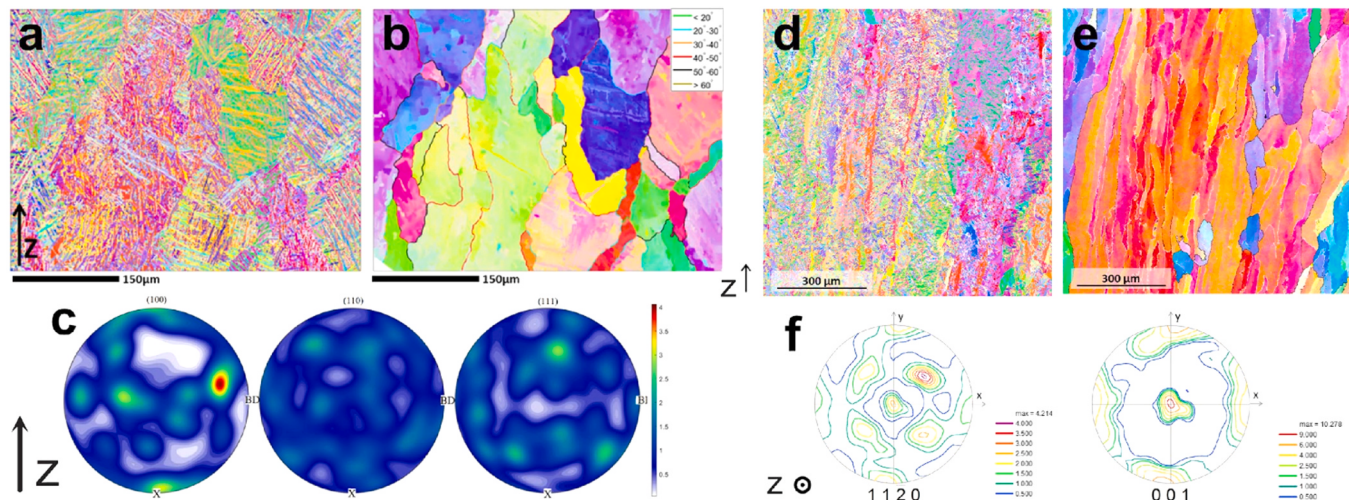


Fig. 34. Detailed microstructure and texture characterization through the EBSD examinations on (a-c) L-PBF and (d-e) EB-PBF Ti-6Al-4V [419,434]. (a) and (d) IPF orientation map of α phase, (b) and (e) IPF orientation map of reconstructed β phase, (c) pole figures of reconstructed β phase in L-PBF Ti-6Al-4V, and (f) pole figures of α phase in EB-PBF Ti-6Al-4V.

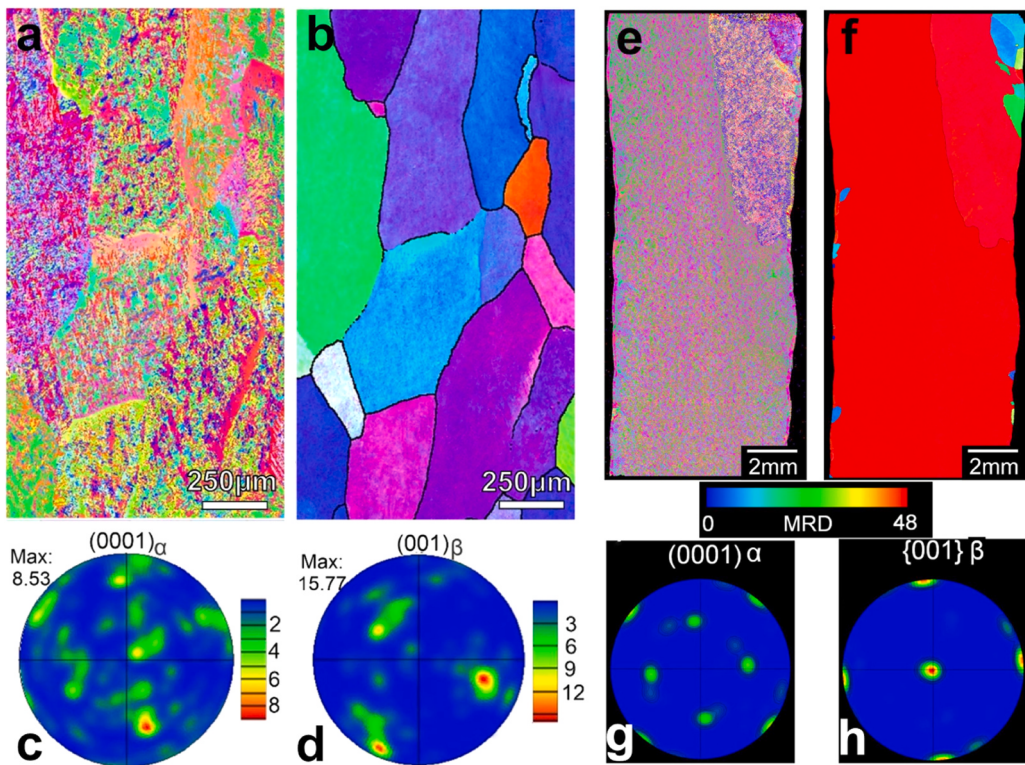


Fig. 35. EBSD characterizations revealing the microstructures and textures of (a)-(d) L-DED Ti-6Al-4V and (e)-(h) WAAM Ti-6Al-4V [109,437]. (a) and (e) IPF orientation map of α phase, (b) and (f) IPF orientation map of reconstructed β phase, (c) and (g) pole figures of α phase, (d) and (h) pole figures of reconstructed β phase.

grains leading to shorter α laths [417]. Furthermore, restricted epitaxial growth due to less remelting of the previously deposited layer from smaller energy inputs leads to smaller prior- β grains, which also leads to a weaker texture in L-PBF titanium alloys [435,436].

Process parameter manipulation, like scanning strategy optimization, influences the texture evolution and reduces the texture intensity of the AM titanium alloys [2,435]. For instance, a weak cubic texture along the scanning and build directions replaces the strong fiber $<100>$ texture by using the chessboard scanning strategy [438,439]. This is achieved by disrupting consistent thermal gradients and the

epitaxial growth of columnar prior- β grains along the building direction. Furthermore, the microstructure refinement approaches, which mainly reduce the prior- β grain sizes and achieve the columnar to equiaxed transitions, also reduce the strong solidification texture [99,109,342].

5.2. Impacts on mechanical properties

5.2.1. Tensile performances

Fatigue and damage tolerance performances are determined by the damage accumulated in each load cycle, and therefore, their deforma-

tion mechanisms are closely related to the tensile behavior under monotonic loading. Here, how specific microstructural features affect tensile behavior is discussed first, which could provide the knowledge to better understand the subsequent dynamic-loading behavior of AM titanium alloys. Both prior- β grain size and α lath thickness are the two microstructural parameters in numerous studies showing dominant influences on the tensile properties, specifically tensile strength, of AM titanium alloys [105,408,424,440,441]. Linear correlations between the inverse of square root of prior- β grain sizes against the yield stress (Fig. 36a), and between the inverse of square root of α lath thicknesses against the yield stress (Fig. 36b) are reported in AM Ti-6Al-4V, respectively [95,105,158,320,408,424,440–442]. Both these correlations were established based on the well-known Hall-Petch relationship:

$$\sigma_y = \sigma_0 + kd^{-1/2} \quad (5)$$

where, σ_y is the yield stress, σ_0 is a material-specific constant, k is the Hall-Petch strengthening coefficient, d is the grain size. It is reasonable to conclude that both prior- β grain size and α lath thickness determine the yield stress of AM Ti-6Al-4V, while the relationship that considers how much contribution from each of the prior- β grain and α lath to the yield stress remains unknown (to the authors' knowledge).

As mentioned in the previous section, large columnar β -grains with the growth direction along the building direction are very common in AM Ti-6Al-4V [99,100,388], which leads to the strong anisotropic mechanical properties in AM titanium alloys (as seen by the large difference between the engineering stress-strain curves of L-DED Ti-6Al-4V in

Fig. 36c) [99,100,109,424,443]. This is mainly because, with the tensile loading perpendicular to the building direction, the long axis of prior- β grain boundaries is subject to the Mode I opening tension (Fig. 36d), which easily cause the delamination of the prior- β grains and lead to the lower ductility. In comparison, the ductility could be reasonably higher with the tensile loading axis parallel to the building direction (the tension is applied parallel to the long axis of prior- β grain boundaries, and thus the prior- β grain boundaries are not subjected to Mode I opening failure).

The spatial orientations and the crystallographic orientations of the α laths should be considered as another factor that affects the tensile properties [109,176,212]. During the tensile loading process, the slip lines preferentially emerge along the α lath with certain crystallographic orientations that have higher Schmid factor for easy deformation modes like prismatic and basal slips [444,445]. In the meantime, a large shear stress that leads to relatively easy crack initiation and propagation could be generated in the α laths with their interfaces approximately 45° off the loading axis [445]. In AM titanium alloys, the accumulations of both spatial orientations and the crystallographic orientations of the α laths are common, which could further contribute to the tensile property anisotropy [444,445].

Compared with the AM α and $\alpha+\beta$ titanium alloys, β titanium alloys have much higher tensile strength after the aging process, which can be attributed to the presence of fine α precipitation [141]. According to the Orowan strengthening mechanism, fine α precipitation could increase the Orowan stress required for dislocations to bypass the precipitate, and thereby enhancing tensile strength [446]. In addition, interparticle

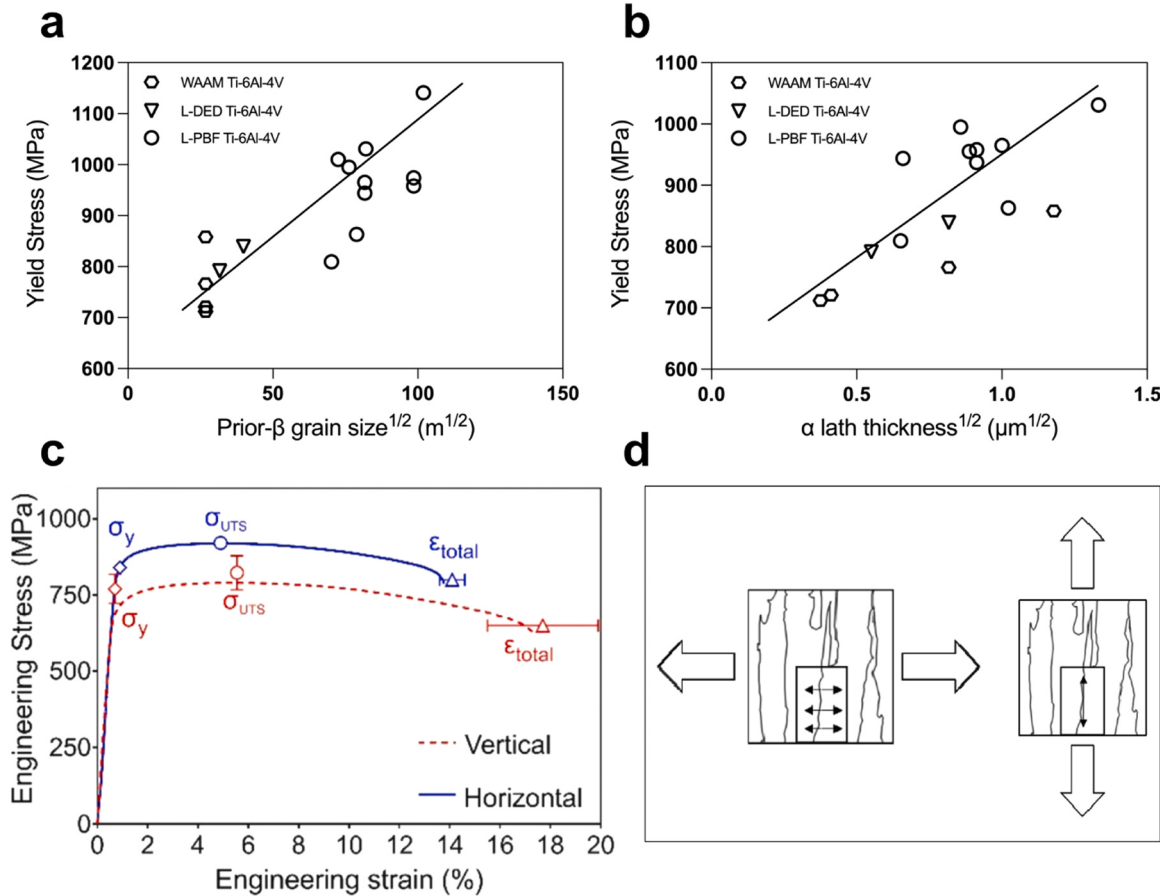


Fig. 36. Effects of microstructures on the tensile performance of AM Ti-6Al-4V: (a) the correlation between the inverse of the square root of prior- β grain sizes and the yield stress of AM Ti-6Al-4V from the literature [105,158,408,424,440,441]. (b) The correlation between the inverse of the square root of α lath thicknesses and the yield stress of AM Ti-6Al-4V [105,408,424,440,442]. The literature values used for both (a) and (b) are derived from those of heat-treated samples to ensure the removal of residual stress. (c) Engineering stress-strain curves of L-DED Ti-6Al-4V at both transverse and longitudinal directions show strong tensile property anisotropy. (d) Schematic drawings show how the presence of columnar grains affects the tensile properties, especially the ductility [100].

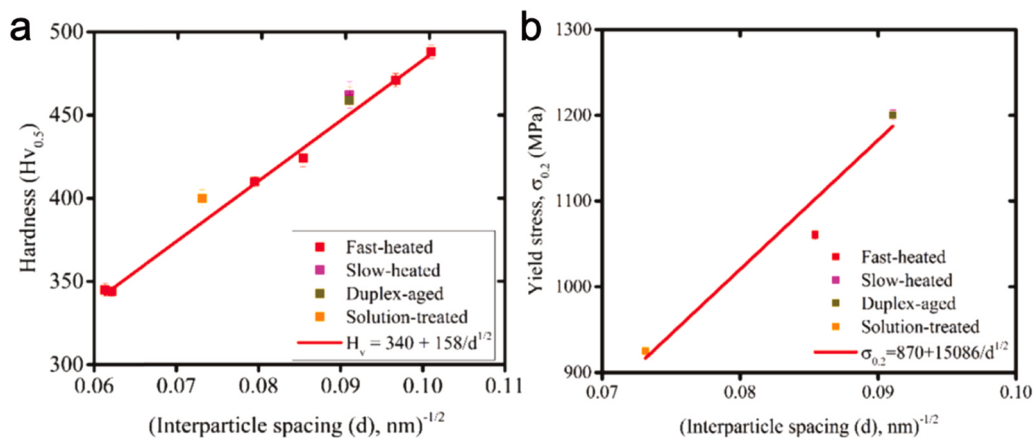


Fig. 37. The summarized linear correlation between (a) the hardness values and (b) the yield strength ($\sigma_{0.2}$) and the interparticle spacing between α precipitates in L-DED Ti-5Al-5Mo-5V-3Cr [334].

spacing of the α phases, which is defined as the distances between the two neighboring α precipitates, is also reported as a microstructural parameter that correlate with the strength of AM β titanium alloys: the strength (including hardness and yield stress) is in the linear relationship with the inverse square root of interparticle spacing (Fig. 37) [125,447].

Grain boundary α -phase (GB- α) is a commonly seen microstructure feature in titanium alloys, which delineates the columnar prior β -grains boundaries [12]. Numerous studies have found that the presence of GB- α is the origin of the low ductility of AM β titanium alloys (even $\alpha+\beta$ titanium alloys), because GB- α could be the dislocation motion barrier, resulting in the strain/stress concentration during the deformation process, which further lead to the intergranular fracture (Fig. 38a-b) [12,134,448,449]. Furthermore, in β -titanium alloys, the GB- α

formation consumes most of the α stabilizers, which might result in the formation of precipitate-free zones (PFZs) [450]. The strength difference between the PFZs and GB- α at β -grain boundaries also lead to the intercrystalline fracture, and thereby causes poor ductility. For instance, the total elongation in L-DED Ti-5Al-5Mo-5V-1Cr-1Fe with continuous GB- α is even below 2 % [358,451]. With the morphology of GB- α becoming discontinuous by heat treatment manipulation, the fracture resistance of AM titanium alloys could be enhanced (the ductility in L-DED Ti-5Al-5Mo-5V-1Cr-1Fe with discontinuous GB- α is above 11 %) [135]. This is mainly because the discontinuous GB- α inhibits the crack propagation along the prior β grain boundaries, leading to transgranular ductile fracture (Fig. 38c-d) [135,418]. Moreover, it was found that the elimination of continuous segments of GB- α eliminate the ductility

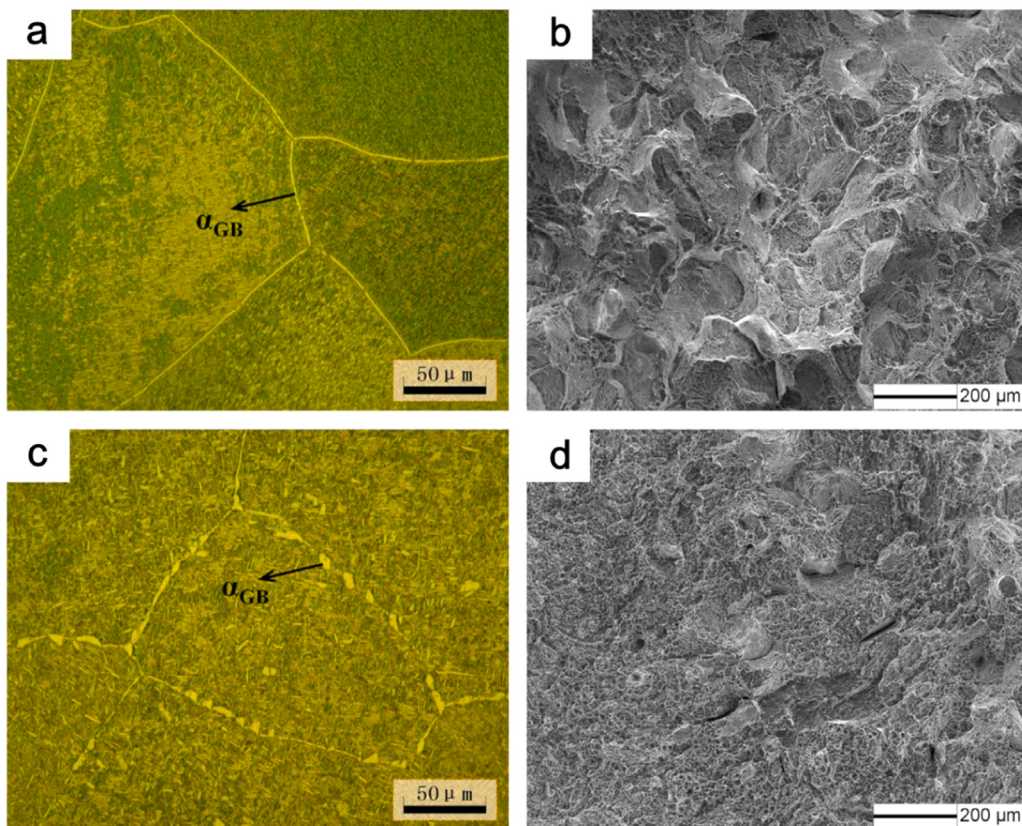


Fig. 38. (a-b) Continuous GB- α in L-DED Ti-5Al-5Mo-5V-1Cr-1Fe and the resulting intercrystalline fracture surface, (c-d) discontinuous GB- α in L-DED Ti-5Al-5Mo-5V-1Cr-1Fe and the resulting transgranular ductile fractography [135].

anisotropy of AM titanium alloys. For instance, the studies on AM Ti-6Al-4V show that the anisotropic ductility reduces significantly with the discontinuous ratio (defined by the total length of discontinuous GB- α segments within a certain prior- β grain boundary length) larger than 0.6 [418,452,453]. This can be attributed to the fact that discontinuous GB- α can uniformly accommodate the deformation with the surrounding grains, as evidenced by in-situ EBSD and corresponding TEM characterization (Fig. 39). Discontinuous GB- α sample shows uniformly distributed dislocations during the loading (while, in the sample with continuous GB- α , higher dislocation density can be found within the continuous GB- α). This disparity shifts the failure mechanism in transverse samples from a brittle opening mode to a more accommodating sliding mode, which increases their ductility significantly and reduces the anisotropy [418].

Texture in AM is another important microstructural parameter (mostly considered a secondary parameter), besides the prior- β grain size and α lath thickness, affecting the mechanical performance of AM titanium alloys [454]. Due to the fact that the room-temperature α phase, which has the hexagonal close-packed (HCP) crystallographic structure, has limited deformation modes of basal, prismatic, and pyramid slip systems with different critical resolved shear stress (CRSS) values, the deformation behavior of a strong textured titanium alloy could be varied at different loading axis (the activation of slip systems varies depending on the loading direction) [455]. Meanwhile, the CRSS values of basal and prismatic slip systems are considered the lowest in the published works, while those of pyramid $\langle a \rangle$ and $\langle c+a \rangle$ are considered higher [456]. Thus, the formation of strong texture in most AM titanium alloys, which certainly transform into a strong α texture by following the variant selection mechanisms during the cooling process [436], can contribute to the mechanical property anisotropy. For instance, L-DED Ti-6Al-4V with strong $\langle 001 \rangle_{\beta}/N_Z$ β solidification

texture could lead to $\sim 14\%$ total elongation difference between transverse and longitudinal samples [99]. In comparison, with trace boron addition (0.05 wt%), the texture can be weakened, which significantly improves the ductility anisotropy (only $\sim 4\%$ difference between transverse and longitudinal samples). Furthermore, the easy slip transmission between grains with similar orientations (corresponds to strong texture), which provides a longer effective slip length, could reduce both the strength and the fracture resistance [456–458].

In addition, other AM-specific microstructure features in titanium alloys have also been reported to influence tensile behavior, which are expected to affect fatigue performance as well. For instance, in L-DED Ti-O-Fe alloy, a unique nano-heteromicrostructure with high Oxygen content can be observed near the interface of α -lath (Fig. 40a) [459]. This feature can impede dislocation motion and blunt crack tips during the loading (Fig. 40b), which could further enhance the tensile ductility. In addition, L-PBF CP-Ti printed in an Ar-3% N₂ atmosphere exhibits nano-scale dislocation tangles and cells within the interior of the α -grains (Fig. 40c-d) [460]. During the deformation, such dislocation cells are stretched and glide past one another, ultimately coalescing into dislocation walls that further impede dislocation motion and, in turn, lead to exceptional elongation (Fig. 40e-f). Furthermore, through the concept of in-situ design, L-PBF Ti-6Al-4V with the addition of a small amount of 316 L stainless steel produces a $\beta + \alpha'$ dual-phase modulated microstructure that shows a progressive transformation-induced plasticity effect (TRIP), which results in excellent work-hardening capacity (Fig. 40g-h) [51].

5.2.2. Fatigue and damage tolerance

The published research up to this time is mostly about the dominant effects of defects on the fatigue and damage mechanisms of AM titanium alloys [28,118,367,461,462], while a limited number of publications

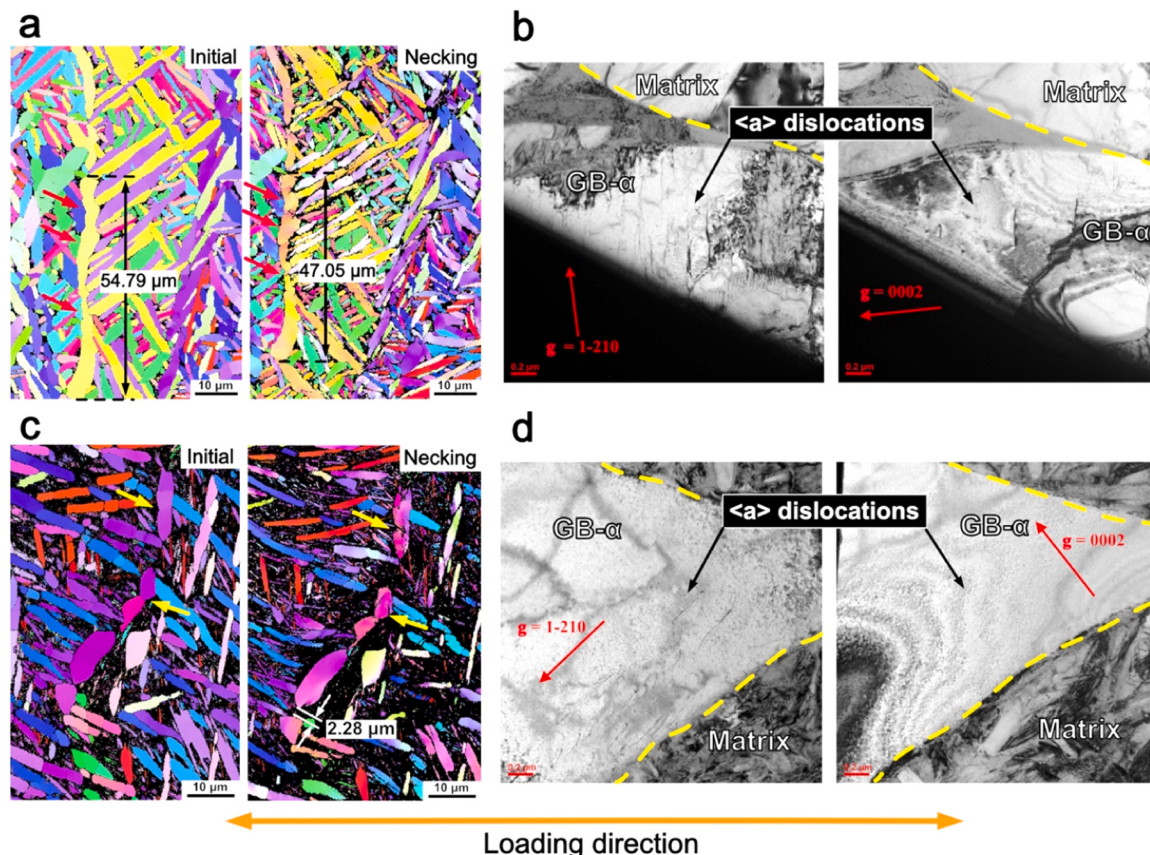


Fig. 39. In-situ SEM-EBSD characterization combined with TEM demonstrated the deformation behavior of GB- α in LPBF Ti-6Al-4V with (a-b) continuous and (c-d) discontinuous morphologies [418].

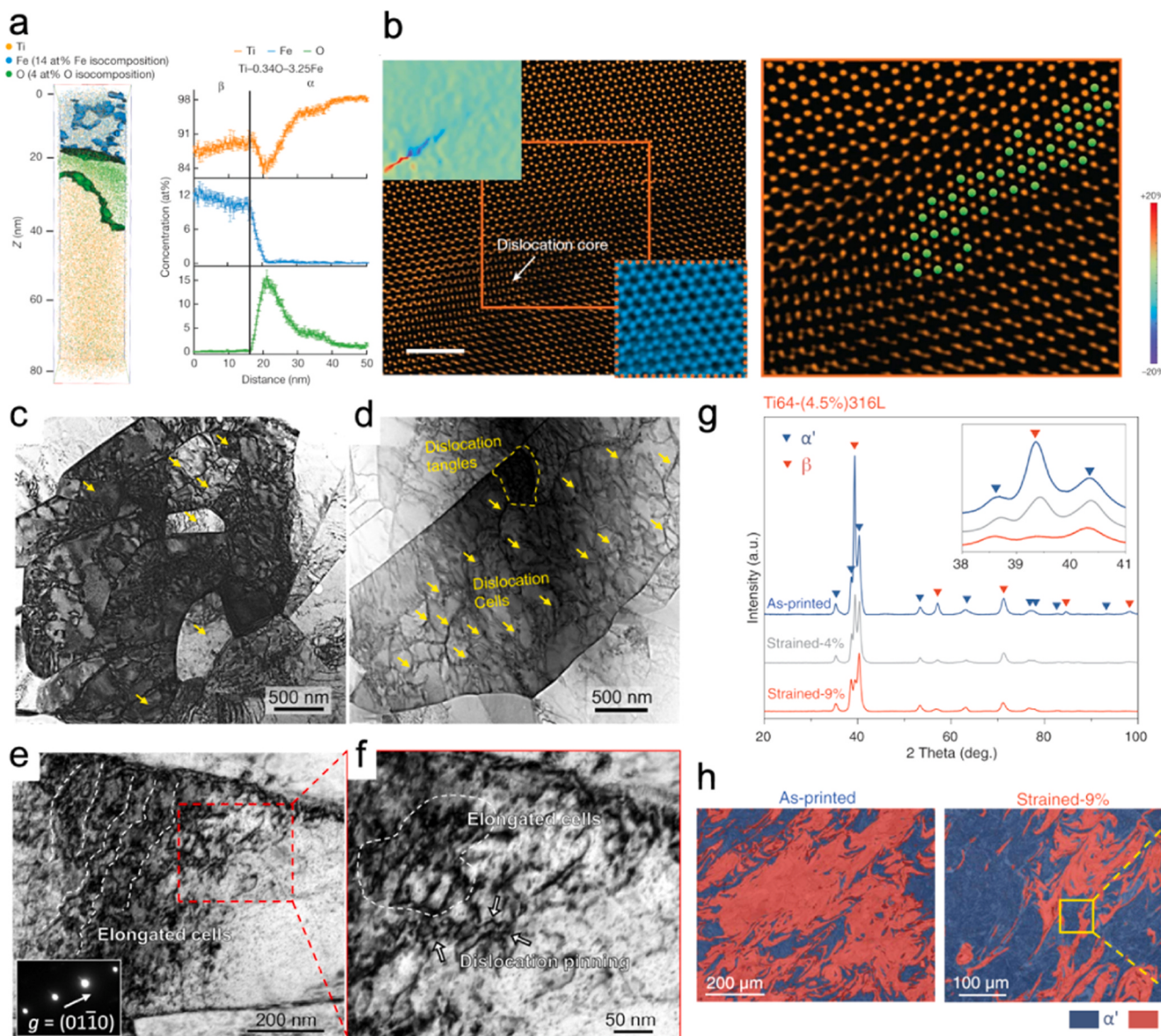


Fig. 40. (a) APT characterizations from L-Ded Ti-0.34O-3.25Fe show the tendency of O atoms to segregate near the α/β interfaces, and (b) Atomic-scale STEM-HAADF images indicate a dislocation inhibited by an O interstitial array [459]. (c-d) STEM-BF images of dislocation cells and tangles in L-PBF CP-Ti, and (e-f) Two-beam BF-TEM images illustrate the dislocation distribution of a 5 % strained samples [460]. (g-h) XRD and EBSD characterizations of the L-PBF Ti64-(4.5 %) 316 L alloy exhibiting the β to α' phase transformation process during tensile test [51].

discussed how the microstructures affect the fatigue crack initiation and growth behavior. These limited published works show strong evidence that the microstructure could affect the fatigue and fracture properties as well. In the meantime, a very recent study successfully predicted the fatigue performance of AM Ti-6Al-4V based on atomistic bonding energetics, further demonstrating that the microstructure (even for atomic-scale features) is closely related to fatigue and damage tolerance performance [463]. Therefore, evaluating meso- and microstructure characteristics such as prior β grain size, grain orientation (texture), α grain morphology, and colony size is crucial for optimizing the fatigue resistance and overall mechanical reliability of titanium components produced through additive manufacturing.

Prior- β grain morphologies in AM Ti alloys are considered as influential for fatigue and damage tolerance performances in most cases. In L-PBF Ti-6Al-4V, it is found that the size of prior- β grains affected the macroscopic fracture morphology (the larger prior- β grains lead to a rougher macroscopic fracture surface) [464]. Some detailed characterization of the fracture surfaces and crack side profiles in different studies

indicate that only long fatigue cracks could easily propagate into the prior- β grains across their boundaries, while short fatigue cracks (with its lengths similar or smaller than the effective microstructural unit) might be arrested in the prior- β grain boundaries [199,461,465]. Meanwhile, since prior- β grain in AM Ti alloys exhibit a columnar morphology aligned along the building direction, there are differences in the fatigue behavior of samples under different loading directions, which eventually leads to fatigue performance anisotropy [165,199, 201]. In detail, sample along the building direction (longitudinal sample) contained more columnar prior- β grains in the plane perpendicular to the loading direction (same as building direction) [466]. In this case, the fatigue crack propagation encounters greater resistance, because the crack needs to interact with several grains. In contrast, in the transverse sample (loading perpendicular to the building direction), the fatigue crack propagated within fewer columnar grains, therefore resulting in a higher crack growth rate. For instance, the study of WAAM Ti-6Al-4V shows more tortuous crack profiles of longitudinal FCG testing failed samples, which indicate the higher fatigue crack propagation resistance

and further support the above viewpoint (smooth crack geometries for transverse sample) [201].

Along with the morphology, the crystallographic texture of the parent β -phase also plays a crucial role in determining the fatigue crack propagation behavior of AM Ti alloys [145,467,468]. The similarly oriented prior- β grains, indicative of the strong β -phase texture, increase the effective slip lengths across adjacent prior- β grains. The larger effective slip lengths facilitate deformation during cyclic loading, potentially leading to more strain accumulation around porosity, thereby reducing fatigue crack initiation resistance. In the meantime, the lower misorientation between neighboring prior- β grains can lead to smooth crack propagation across different grains, resulting in minimal fatigue crack growth resistance [469]. In contrast, the weak β -phase texture (corresponding to a large misorientation between neighboring prior- β grains) increases the difficulties of slip transfer between adjacent prior- β grains, which causes more crack deviation and leads to high fracture crack growth resistance [470,471]. Furthermore, since the crystallographic texture of the parent β -phase could be directly linked to α -phase texture (according to the variant selection mechanisms), strong β -phase texture also corresponds to strong α -phase texture [99,342]. Strong α -phase texture could also lead to easier slip transmission within the prior- β grain, and eventually induce the occurrence of intensive slip bands. This is directly related to the low fatigue crack initiation resistance.

Furthermore, GB- α that decorates the prior- β grain boundaries also has strong implications for the fatigue performance of AM Ti alloys [218, 472,473]. Similar to the effects on tensile properties, continuous GB- α is also the vulnerable site for fatigue crack initiation and leads to low fatigue performance of AM Ti alloys. For instance, L-DED Ti-5Al-5Mo-5V-3Cr-1Zr with continuous GB- α shows relatively poor fracture toughness (K_q values is $51.6 \text{ MPa}\sqrt{\text{m}}$), which is significantly lower than that of the state containing discontinuous GB- α (K_q values is $81.7 \text{ MPa}\sqrt{\text{m}}$) [234]. This is mainly because the difference in the crystallographic orientation and geometry of adjacent prior β -grains could inevitably lead to strain incompatibility, causing the stress concentration at the GB- α [399]. Meanwhile, continuous GB- α with almost identical crystallography orientation can serve as a preferred pathway for fatigue crack growth, particularly in the GB- α layers oriented perpendicular to the loading axis (Fig. 41) [474]. In comparison, discontinuous GB- α accommodates the deformation with prior β -grains during the loading, making it not a potential site for fatigue crack initiation [399]. In addition, adjacent discontinuous GB- α grains on the same prior- β grain boundary normally exhibit relatively larger crystallography orientation differences, which can inhibit the fatigue crack propagation along it [473]. Therefore, the prior- β grain boundary with discontinuous GB- α is regarded as not detrimental to the fatigue performance in AM Ti alloys.

α colonies could be another meso-scale factor influencing the fatigue crack propagation behavior in Ti alloys processed by AM (particularly for L-DED and WAAM, in which the cooling rate is comparatively slower) [475]. Most α laths within the same colony share similar crystallographic orientations, which leads to easy slip transmission across the lath interface and forms continuous slip bands across the whole α colony. The continuous slip bands and aligned close-packed crystallographic planes due to the similar orientations are the favorite fatigue crack pathways [457]. For these reasons, some studies suggest that the increased colony size results in a reduction in the fatigue life due to an increase in slip length [474,476]. However, due to the high misorientation angle between adjacent α colonies, crack transmission between colonies is significantly difficult, eventually resulting in complicated and multi-branched fatigue crack pathways [205,475]. As revealed in Fig. 42, the fatigue crack path in L-DED Ti-6Al-2Sn-4Zr-2Mo-0.1Si alloy is deflected at the α colony boundaries [477]. This results in a tortuous crack path and improves fatigue crack propagation resistance (Paris constant $m = 1.2$ in this case, which is significantly lower than that of the as-built state with a martensitic structure ($m = 2.1$) and the annealed state with a basket-wave structure ($m = 2.5$)). Meanwhile, since dislocations move more easily within the colony, the large α colony leads to an increase in the plastic zone at the crack tip. Thus, another understanding is that increasing the α colony size improves the fatigue crack propagation resistance.

Furthermore, the studies on the L-PBF Ti-6Al-4V showed that the morphology of the α phase within the prior β grain affected the crack growth path and the FCG rate [61,464,478]. Fine α' martensite in the as-built state leads to smooth crack propagation geometries, resulting in a fast fatigue crack growth rate, low HCF performance, and poor fracture toughness (can also be evidenced by the brittle facet fracture in Fig. 43a)

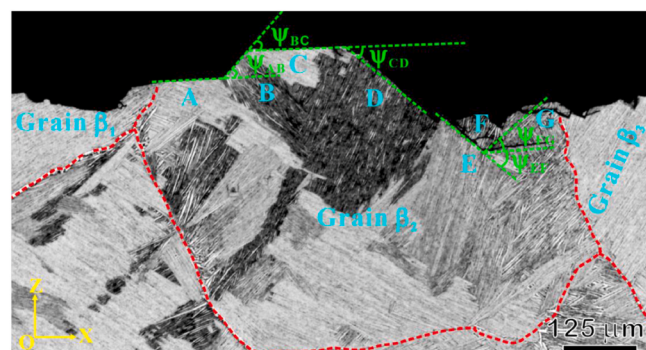


Fig. 42. SEM image of the fatigue crack path in L-DED Ti-6Al-2Sn-4Zr-2Mo-0.1Si after solution treated at 1030 °C for 1 h + aged at 595 °C for 8 h [477].

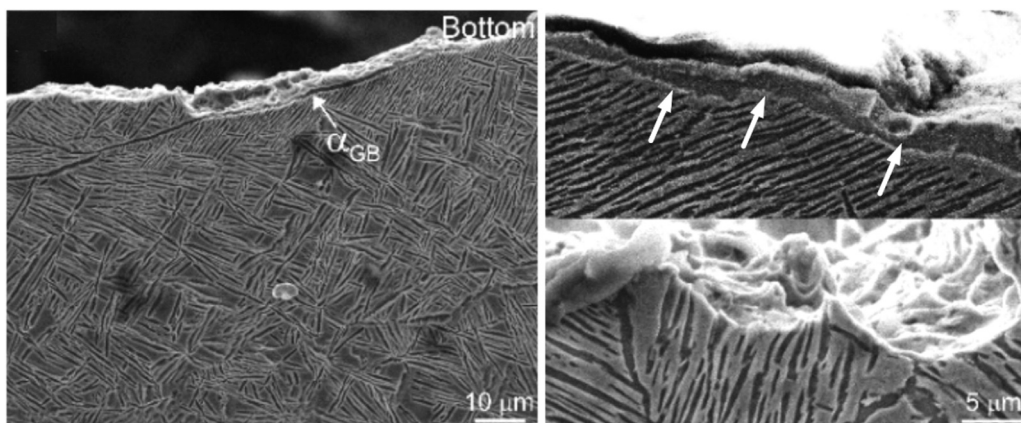


Fig. 41. SEM image shows the cross profile of K_{IC} fractured L-PBF Ti-5Al-5Mo-5V-3Cr-1Zr, exhibiting cracks propagation along continuous GB- α [233].

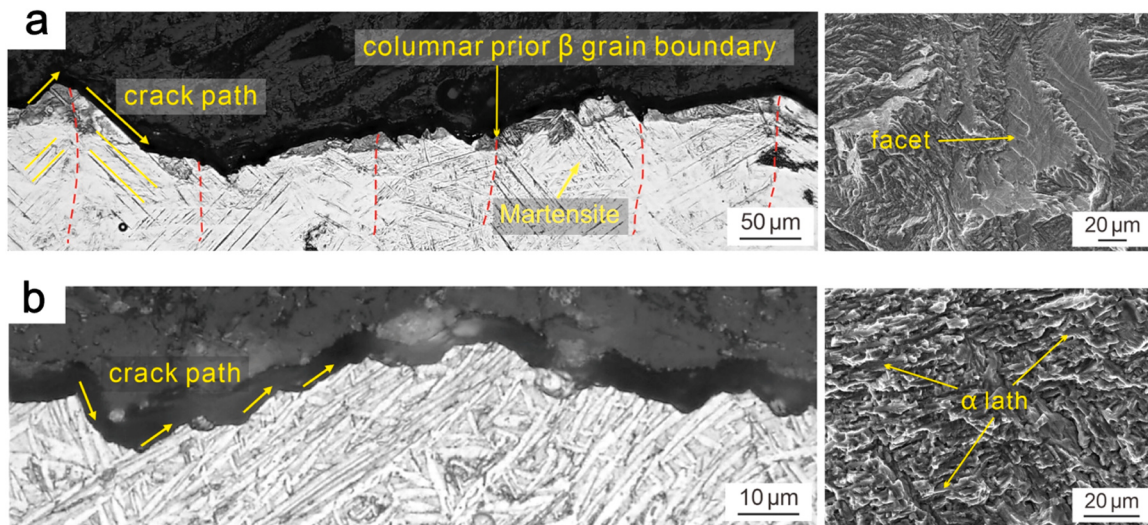


Fig. 43. (a) Fatigue crack growth path and fracture surface of L-PBF Ti-6Al-4V in the as-built state, showing the flat facet caused by martensites [464]. (b) Fatigue crack growth path and fracture surface of L-PBF Ti-6Al-4V after solution at 900°C for 1 h + aging at 500°C for 4 h, exhibiting the jagged crack pathway and dimples indicative of ductile failure [464].

[464]. Microstructure optimization and residual stress elimination by using post-AM heat treatments significantly improve the fatigue crack propagation resistance (including the small fatigue crack propagation resistance) and fracture toughness properties [74,202,205]. During the post-AM heat treatments, very fine martensite could be decomposed into coarser α laths, which can lead to a tortuous crack path and improve fatigue crack propagation resistance (Fig. 43b) [198,475]. A detailed investigation into the in-situ fatigue testing characterization shows that the α lath is the favorable path for the short fatigue crack propagation along their boundaries and forms the intergranular fracture features on the fracture surface [461]. This further indicates that coarse microstructure in AM titanium alloys could be favorable for the fatigue crack propagation resistance, which is consistent with that in conventionally manufactured titanium alloys.

The α grain sizes in both L-PBF Ti-6Al-4V and CP-Ti after different post-AM treatments, including the HIP process, could be fully correlated with the fatigue crack propagation (Fig. 44) [74,206]. In detail, it is found that fatigue crack propagation thresholds (ΔK_{th}) could be proportional to the yield stress (σ_{YS}) and the measured grain sizes (or α lath thickness, d), Fig. 44a:

$$\Delta K_{th} = k \cdot \sigma_{YS} \sqrt{d} \quad (6)$$

where k is a constant. The further correction of converting ΔK_{th} into the effective fatigue crack propagation thresholds ($\Delta K_{eff,th}$) with the fatigue crack closure effects removed shows an even better linear proportionality, as shown in Fig. 44b [74,206]. This indicates that the α grains in AM titanium alloys could be the effective microstructural unit that restricts the dislocation motion to the grain boundaries in a very low-stress intensity range during the cyclic loading. The α lath elongation directions are another factor that determines the crack propagation direction deviation and deflection for both transgranular and intergranular crack propagations [198]. Specifically, the α laths with elongation directions approximately perpendicular to the crack propagation direction are more likely to deflect the cracks from the maximum driving force direction, which results in more tortuous cracks [198,479]. Furthermore, the aspect ratio of α lath is linked to the fatigue crack initiation threshold, thereby affecting the fatigue-related performance of AM Ti alloys [67,441,473]. Based on crystal plasticity finite element model analysis [480], with the aspect ratio of grain decreases to 1 (equiaxial shape), the effect of interface on fracture resistance diminishes, resulting in a reduction of dislocations accumulation on the lath boundaries during deformation. Therefore, α lath with a small thickness and large aspect ratio leads to increased strain accumulation at the interfaces between adjacent α laths. This high strain accumulation

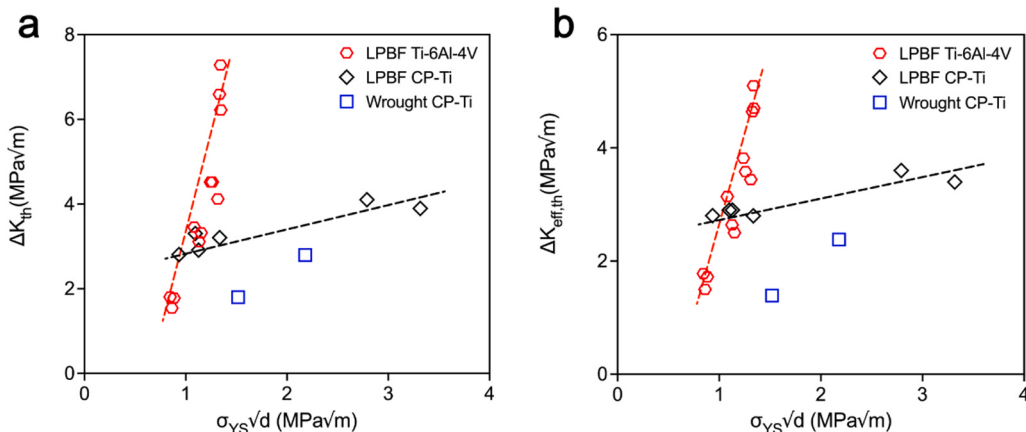


Fig. 44. The correlations between (a) the fatigue crack propagation thresholds (ΔK_{th}) and (b) the effective fatigue thresholds ($\Delta K_{eff,th}$) with crack closure effects removed, against the α grain sizes and yield stresses in L-PBF Ti-6Al-4V and CP-Ti with the trend lines labeled [74,206].

may initiate fatigue crack from the lath interface, contributing to fast FCG rates and poor HCF properties.

As compared to α or $\alpha + \beta$ Ti alloys, AM β -titanium alloys typically exhibit distinct α -phase morphologies, as described in 5.1.1. These microstructures, in turn, influence the fatigue and damage mechanisms of alloys. L-DED Ti-5Al-5Mo-5V-1Cr-1Fe exhibits a hierarchical α -phase structure composed of coarse primary α -laths and fine secondary α -precipitates [220]. Microstructure examination along the fatigue crack path shows that cracks preferentially nucleate and propagate along the primary α -laths, as shown in Fig. 45a-b. This is caused by the strain incompatibility between the coarse primary α -laths (relatively soft) and fine secondary α -precipitates (relatively hard) [481]. To this end, by controlling the size, volume fraction, and spatial distribution of the hierarchical structure, the fatigue crack growth behavior of AM β -titanium alloys could be changed [220,481,482]. When the angle between the crack and coarse primary α -laths is not too large, the fatigue crack path can globally deflect along the primary α -laths, as shown in Fig. 45c. As the angle increases further, the fatigue crack could directly pass through the primary α -laths (Fig. 45d). Fatigue model based on peridynamic framework confirm that the fatigue crack propagation rate of AM β -titanium alloys slows down significantly in this case [481]. In addition, recent studies on EB-PBF Ti-5Al-5Mo-5V-3Cr-1Zr [483], L-DED Ti-5Al-3Mo-3V-2Zr-2Cr-1Nb-1Fe [221], and L-PBF Ti-5Al-5Mo-5V-1Cr-1Fe [232] found that increasing the volume and size of the primary α -laths can also significantly hinder crack growth. This is because coarser α -laths act as barriers that repeatedly deflect or branch the crack growth, increase path tortuosity, and thereby raise the energy-release rate required for further propagation.

5.3. Effects of microstructures on tensile, fatigue and damage tolerance performances at extreme temperatures

5.3.1. Elevated temperatures

Mechanical performance at elevated temperatures is highly sensitive to the microstructure of the AM Ti alloy. Due to the activation of grain boundary sliding as a deformation mode at elevated temperatures (Fig. 46a), the prior- β grain boundary is consistently identified as a

preferential site for damage nucleation [237,484]. In this case, clean prior- β grain boundaries (i.e., in the as-built state) or those decorated with continuous GB- α serve as pathways for crack growth, and thus lead to low ductility (Fig. 46b) [228,485]. In contrast, discontinuous GB- α can accommodate the deformation and inhibit crack propagation along the prior- β grain boundaries, thereby enhancing the fracture resistance of AM Ti alloys [485].

Within the prior- β grain, α' martensite in as-built state L-PBF near- α or $\alpha + \beta$ Ti alloys exhibit relatively high strength but poor ductility at elevated temperatures. For instance, L-PBF Ti-6.5Al-2Zr-1Mo-1V alloy shows 950 MPa UTS with a limited elongation of 10 % at 500 °C [228]. This is mainly because the formation of α' martensite is commonly accompanied by prevalent lattice defects, which increases the difficulty of further activating the slip at elevated temperatures. In this case, the deformation of α' martensites is dominated by the microscale shear bands (MSBs) at the interfaces [484], as shown in Fig. 47a-c. In addition, due to the poor thermal stability of α' martensite, excessively high testing temperatures can cause α' martensites to decompose into $\alpha + \beta$ phases (and even lead to brittle γ (TiAl) or α_2 (Ti₃Al) phase formation in high-Al content titanium alloys, as shown in Fig. 47g-h) during the deformation process [240]. This causes most of the dislocations stored in the α' martensites to recover, resulting in a significant decrease in strength, as mentioned in 3.4.1. In comparison, after the decomposition of α' martensite into $\alpha + \beta$ phase through heat treatment at 800 °C for 4 h, the ductility of L-PBF Ti-6.5Al-2Zr-1Mo-1V alloy increases to 16 % at 500 °C [485], which can be attributed to the activation of multiple slip systems during elevated temperature deformation [484]. This is evidenced by the high density of dislocations found in the TEM characterization of L-PBF Ti-6.5Al-2Zr-1Mo-1V after high-temperature tensile deformation [484], as shown in Fig. 47d. In the case of the negligible volume fraction of the prior β ligament (fine β phase located within α lath or between adjacent α laths), strain primarily concentrates in the interface between α phase and β ligament, and eventually leads to the formation of voids. However, a recent study in L-PBF Ti-6Al-3Mo-1Zr found that nano-scale and uniformly distributed β ligaments accommodate the strain and prevent strain localization along the prior- β grain boundaries, which provides superior elongation and fracture toughness

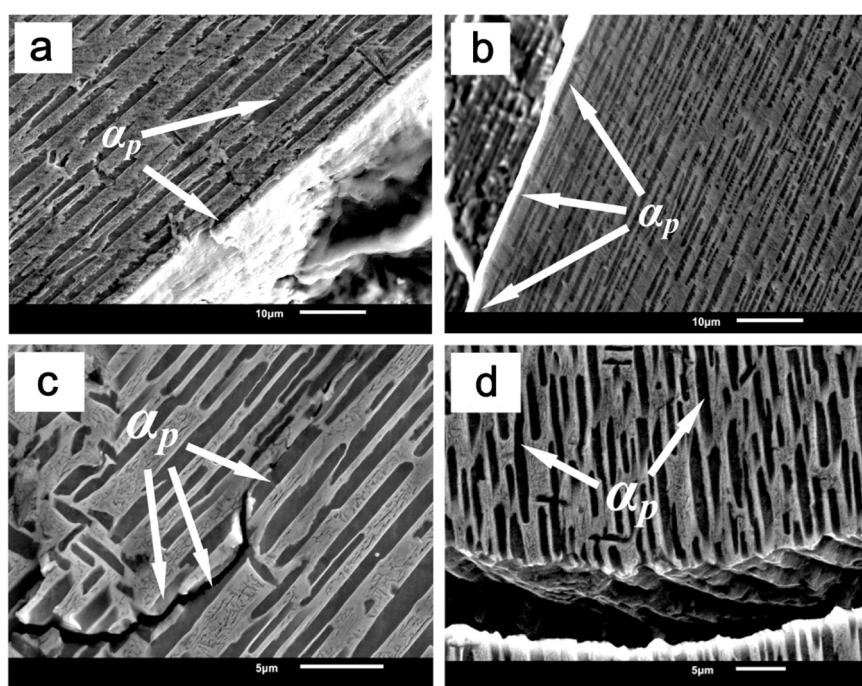


Fig. 45. SEM images of the fatigue crack path of L-DED Ti-5Al-5Mo-5V-1Cr-1Fe [220]: (a-b) crack growth along the primary α -laths, (c) crack path deflects along primary α -lath boundaries, and (d) crack directly passes through primary α -laths.

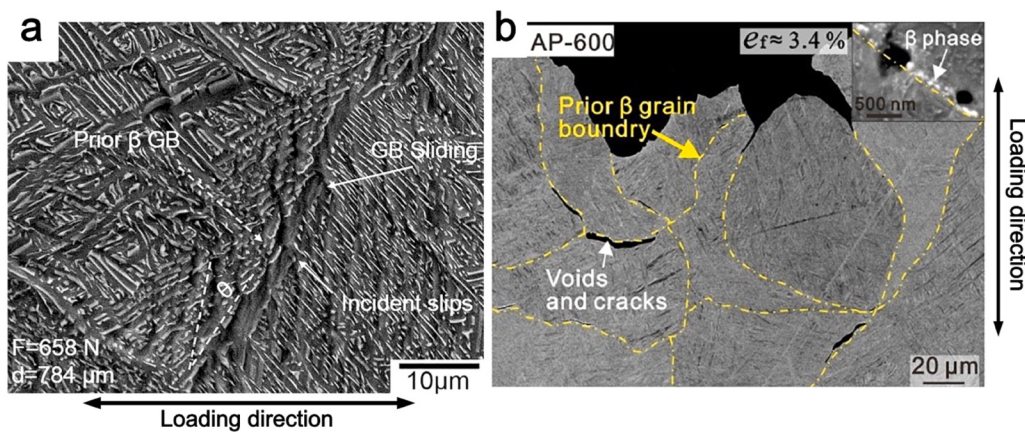


Fig. 46. (a) In-situ tensile test of L-DED Ti-6.5Al-2Zr-1Mo-1V at 500 °C, showing the grain boundary sliding along the prior- β grain boundary [237]. (b) The cross-sectional characterization of the tensile failed sample of L-PBF Ti-6Al-3Mo-1Zr at 600 °C reveals the crack growth along the prior- β grain boundary [228].

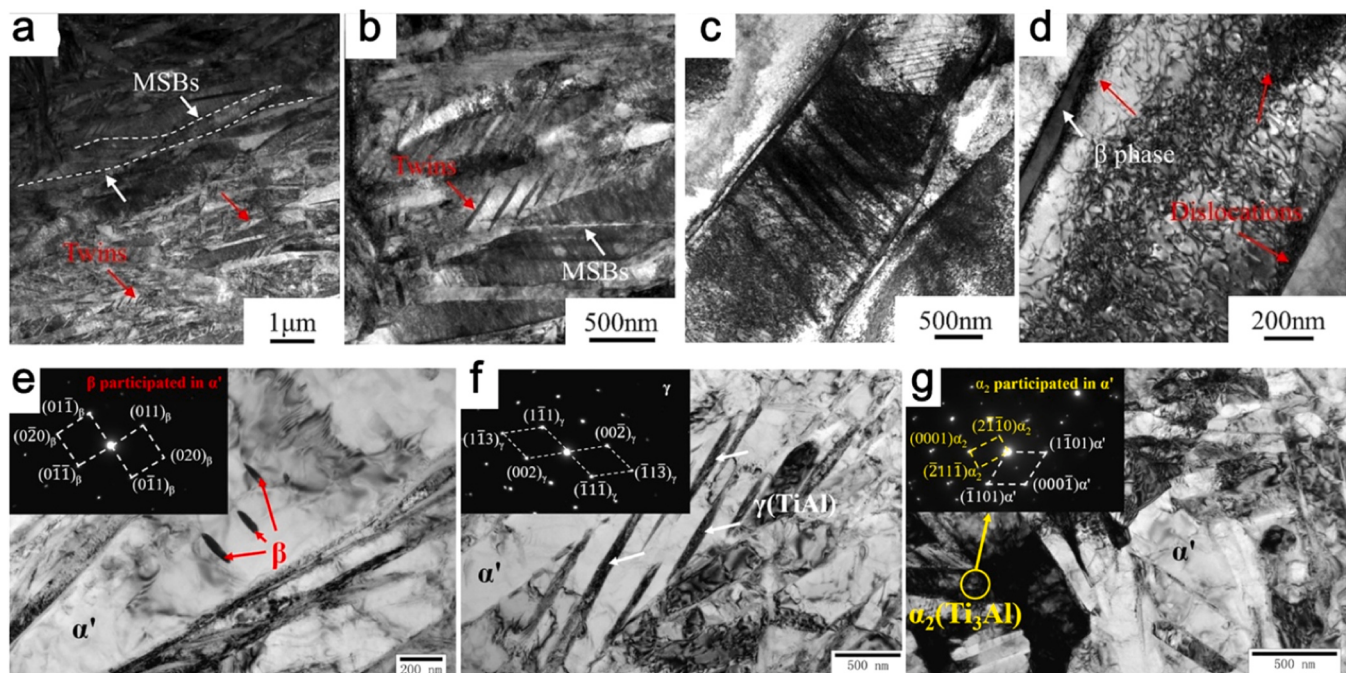


Fig. 47. (a-d) TEM images of L-PBF Ti-6.5Al-2Zr-1Mo-1V in (a-b) the as-built and (c-d) heat-treated states after 500 °C tensile testing [484]. (e-g) TEM images of L-PBF Ti-6Al-4V after 550 °C tensile testing, showing the formations of (e) β , (f) γ (TiAl) and (g) α_2 (Ti₃Al) during the deformation process [240].

at elevated temperatures [228]. Thus, achieving a uniform distribution of nanoscale β ligament while ensuring discontinuous GB- α is a pathway to enhance the in-service properties of AM Ti alloys at extreme temperatures.

5.3.2. Cryogenic temperatures

With the testing temperature dropping into cryogenic, the critical resolved shear stresses (CRSS) for most slips increase, while CRSS for twining decreases [486]. As a result, the plastic deformation of AM Ti mainly depends on twinning, which is distinct from the room temperature. Consequently, AM Ti alloy deformed at cryogenic temperatures shows the serrated tensile curve and multiple necking at the failed tensile sample (as described in 3.4.2). This phenomenon is mainly due to the highly localized characteristics of the twinning. In detail, during the deformation process, the activation of twinning could instantly relieve the local high stress, leading to localized strain softening and decreased flow stress [17]. Meanwhile, the local temperature rise caused by localized plastic deformation also promotes the dislocation motion,

which further contributes to strain softening [487,488]. However, since the formation of twinning is limited within one microstructure unit, the expansion of plastic deformation zones is restricted as deformation progresses, resulting in localized work hardening and increased flow stress [272]. This periodic interplay between softening and hardening ultimately results in serrated flow stress.

For the above reasons, it is evident that the effect of microstructural characteristics on mechanical performance at cryogenic temperatures differs from that at room temperature. It is well documented that α colony is a more favorable microstructure feature that achieves the desirable mechanical performance of AM Ti alloys, compared to equiaxed microstructures [271] or basketweave structures [47,488]. For instance, EB-PBF Ti-3Al-3Mo-3Zr-0.2Y alloy with α colony structures can achieve a superior elongation being up to 20 % with acceptable UTS exceeding 1450 MPa at 20 K [17]. In contrast, EB-PBF Ti-3Al-3Mo-3Zr-0.2Y alloy with a basketweave microstructure only lead to ductility of around 11 % at 20 K [17]. This difference is primarily attributed to the activation of long-distance slip bands and α -Ti twinning

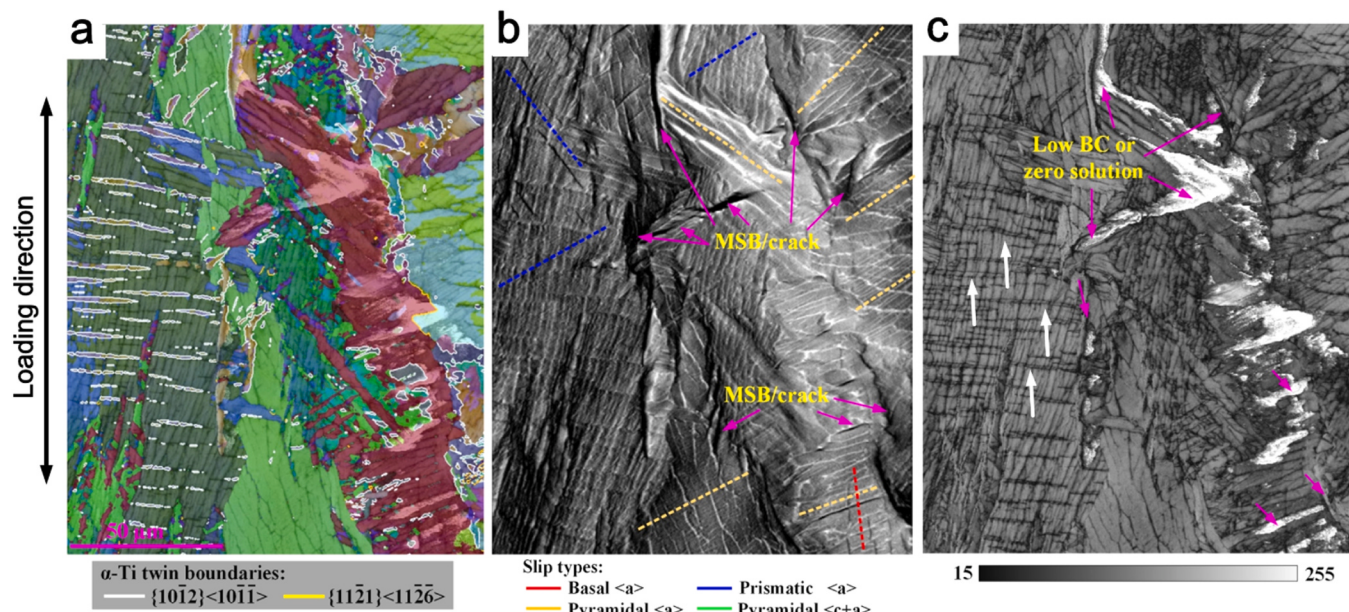


Fig. 48. Longitudinal sectional characterization of the EB-PBF Ti-3Al-3Mo-3Zr-0.2Y tensile samples strained to 10.0 % at 20 K: (a) EBSD-Euler maps with the highlighted twin boundary, (b) SEM-BSE image with the identified slip traces, and (c) band contrast map [272].

within α colonies during the cryogenic deformation, which are sufficiently extended to traverse the colony (as shown in Fig. 48). In comparison, in AM Ti alloy with basketweave structures, the active α -Ti twins and slip bands are challenging to expand over long distances, in particular, the motion of the twin is consistently confined within individual α -Ti grains [47]. Furthermore, α' martensite, commonly found in as-built L-PBF near- α Ti alloys, has been reported to provide exceptionally high tensile strength at cryogenic temperature (> 1750 MPa UTS in as-built L-PBF Ti-6.5Al-2Zr-Mo-V at 77 K), which could be attributed to the activation of pyramidal $\langle c+a \rangle$ slip and nano-twins (including triple twins) [271]. This meets the demands of high-strength applications at cryogenic temperatures. However, with the development of next-generation liquid hydrogen-powered vehicles, more study is required to understand the role of the microstructure generated by AM on the in-service properties of Ti alloys, especially for more concerned fatigue and damage tolerance performance.

6. Conclusions and outlook

6.1. Conclusions

The present review provides an overview of the fatigue and damage tolerance properties of various Ti alloys produced by AM techniques, with a focus on their correlation with diverse defects, unique grains and phases, and process-related attributes. The main conclusions are provided below:

Currently, optimized AM processing parameters can achieve high relative density for various titanium alloys, with static mechanical properties, such as tensile strength, comparable to—or sometimes even exceeding—those of wrought products, even under extreme environmental conditions. However, retained defects, including printing pores, heterogeneously distributed phases, and residual stress can lead to premature fracture, and degrade dynamic performances, such as fatigue and damage tolerance. One of the outstanding features of fatigue performance in AM Ti alloys is the significant variability, which results from the printing pores. Even in the AM titanium alloys from the same build batch with optimal processing parameters, the random and unpredictable occurrence of the pores contributes to an order of magnitude difference in high-cycle fatigue properties. Numerous models—like stress intensity factor—have been proposed to evaluate the effects of pores,

but predictive fidelity remains limited because fatigue life depends on coupled pore characteristics (size, morphology, distribution, and proximity to surfaces).

In terms of damage tolerance performance, printing pores do not have a significant effect unless their scale approaches or exceeds plastic zones and interrupts fatigue crack propagation. In contrast, residual stress is considered as the primary factor that deteriorates the damage tolerance performance of AM Ti alloys. High and non-uniform residual stresses in AM Ti alloys influence fatigue crack opening and closure during cyclic loading, causing a shift in the mean applied load during FCG testing. This results in highly variable FCG behavior and contributes to anisotropy in the fracture toughness of AM Ti alloys.

The unique thermal history of AM process produces microstructure characteristics unlike those of wrought Ti, with competing consequences on fatigue and damage tolerance performances. Owing to the strong directional solidification, epitaxial grain growth is favored in most AM Ti alloys, with the grain elongation directions along the thermal gradient direction, which could reduce high-cycle fatigue and damage tolerance performance. In contrast, rapid cooling of AM process can lead to weak α'/α variant selection and clean prior- β -grain boundaries in AM Ti alloys, which enhance the FCG resistance. Therefore, it is necessary to consider all the above-mentioned microstructure features for the improvement of the mechanical properties of AM Ti alloys.

The fatigue and damage tolerance performances of AM Ti alloys can be enhanced through defect reduction and microstructure optimization. Hot isostatic pressing (HIP) is currently considered the most effective in reducing pore defects, enhancing high-cycle fatigue properties (beyond wrought Ti in some cases), while stress-relief treatments can reduce residual stress and markedly improve fracture toughness and FCG behavior toward conventional benchmarks. Meanwhile, proper post-AM heat treatments, such as solution treatment and cyclic thermal cycling, are also critical for decomposing martensitic phases, promoting the precipitation of fine α -phase, and disrupting continuous grain boundary α -phases, which could further enhance tensile, fatigue, and damage tolerance performances. However, most post-AM heat treatment schedules could also lead to undesirable grain coarsening, potentially degrading tensile and fatigue properties. To mitigate this, strategies such as scan-path optimization (e.g., $\sim 67^\circ$ rotations/interrupts), grain-refiner additions (La_2O_3 , B, Si), and field-assisted methods (like ultrasound field and mechanical deformation field) promote columnar-to-

equiaxed transition and texture weakening, thereby improving the overall mechanical performances of AM titanium alloys.

6.2. Opportunities, challenges, and outlook

Despite sustained progress that brings the tensile—and in some cases fatigue—properties of AM titanium alloys to parity with, or beyond, conventionally manufactured products, the inherent performance potential of AM Ti alloys, particularly in damage tolerance, has not yet been fully realized. There have been several scientific challenges in achieving target performances. First, defects are not yet controlled at source with the reliability and cost efficiency required for certification. Post-processing (like HIP) can reduce variability but cannot remove lack-of-fusion porosity, keyhole cavities, and surface-connected notches. In addition, the interactions among non-equilibrium phase, α/β phase and texture, residual stresses, surface condition, and defect statistics remain only partially resolved across scales, so that process windows optimized for porosity may simultaneously alter martensite, α/β phase, texture, and residual stress, which could sometimes deteriorate the fatigue and damage tolerance performances. Finally, the evaluations of damage tolerance performances predominantly focused on $\alpha+\beta$ titanium alloys to date, while research on high-strength and high-toughness β titanium alloys, which have already been validated for applications, remains relatively scarce. Moreover, AM has been largely limited to high-cost fusion-based technologies, the fatigue and damage-tolerance performance of titanium alloys produced via emerging low-cost AM approaches (like binder jet printing) has yet to be systematically assessed. To this end, several topics for future research that could further enhance the fatigue and damage tolerance of AM Ti alloys, thereby facilitating broader adoption in critical applications.

One of the key points is to improve the internal build quality by moving from post-AM defect cure to in-process prevention. Although defect elimination with additional post-processing step like HIP shows great potential for improving quality control, these methods significantly increase the cost of AM Ti parts. Thus, the ideal solution is to eliminate defects during the printing process. The recent developed Hybrid AM technology has shown great potential in alleviating the printed defects and undesired columnar grains of AM products [109, 342], achieving by external aids (like rolling). Furthermore, in-situ monitoring combined with closed-loop printing parameter optimization is also a promising approach. This method can reduce the likelihood of pore defect formation by continuously tracking the AM process to detect defects and dynamically adjust parameters like laser power and speed. Recently, in-situ monitoring has already been included in the strategic guidelines for AM and is expected to achieve pore-free AM in the future [489].

Another closely ranked priority is to further understand and predict how across-scaled AM-specific microstructures influence fatigue and damage tolerance performances. Micromechanics have long served as the standard approaches. For instances, crystal-plasticity finite-element modeling (CPFEM) connects α/β morphologies, α' martensites, and crystallographic textures to fatigue life by resolving slip activation, mean-stress relaxation, and residual-stress fields [490]. However, there are several major challenges for micromechanics, that is microstructural parameter identification, computational cost and transfer from representative-volume elements to components. Currently, machine learning presents a promising solution [491,492]. For instance, Bayesian calibration, that can regularize illposed inverse problems with priors and allows sequential updating, is expected to cut the number of high-fidelity solves while stabilizing parameter posteriors for CPFEM and cohesive models. In addition, physics-informed surrogates (graph neural networks or Gaussian-process models) can be directly coupled to CPFEM and phase-simulation, which is expected to further enhance model reliability and thereby deepen the understanding of fatigue behavior in AM titanium alloys.

On this basis, machine learning can also assist in tailoring

microstructures by deploying physics-informed surrogates—trained on compact datasets that link process vectors and in-situ signals to thermal descriptors—to predict, with calibrated uncertainty, prior- β grain size, α -lath thickness, texture, and defect risk while embedding mechanistic features such as G/R and transformation kinetics. Embedded within multi-objective Bayesian-optimization/digital-twin loops, these surrogates can prescribe printing parameters (e.g., scan-path rotation, inter-layer dwell/preheat) and targeted post-AM heat treatments that deliver balanced, damage-tolerant AM Ti microstructures.

An additional priority is to develop additional AM titanium alloys that exhibit high fatigue resistance and damage tolerance to enable broader industrial adoption. On one hand, it is important to evaluate the in-service performance of conventionally high-toughness β titanium alloys already qualified for load-bearing use (e.g., Ti-10V-2Fe-3Al, Ti-8Al-1Mo-1V) when fabricated by AM, and demonstrate compliance with safety-critical component design standards to enable broader industrial adoption. On the other hand, alloys development will extend beyond just commercial alloys. Alloy design should explicitly leverage AM's unique thermal history-steep solidification gradient, rapid cooling, and cyclic reheating/remelting-to tune phase stability and kinetics. Through composition design, the target alloys should exhibit robust AM printability (low volatility/segregation and low hot-cracking/porosity susceptibility), optimized lattice parameters (near-ideal lattice constants that reduce the Peierls barrier and facilitate dislocation activation), microstructural stability under cyclic reheating (suppressed ω/α , equiaxed β -grain with controllable α -lath thickness), which thereby achieve high damage tolerance performances. CALPHAD/DICTRA calculations combined with the multiphase flow models that covering molten pool dynamics, phase field and cellular automaton models, and crystal plasticity models are expected to achieve this goal. In addition, multi-laser and multi-materials AM technologies [493–495], might be possible hardware tools at present, which can unlock new possibilities for creating advanced Ti alloys with heterostructure at the mesoscopic (melt-pool) scale. Microstructures engineered at this scale can be designed to enhance complementary properties (such as strain hardening and fracture toughness) and to lower the FCG rate, all of which increase the damage tolerance of AM titanium alloys [496].

In addition to alloy development, other emerging AM technologies also warrant further exploration. Lower-cost AM technologies—binder jet printing, area-printing (e.g., pixelated/multibeam exposure)—promise step changes in throughput and part cost, yet their readiness for fatigue- and damage-tolerance-critical Ti components remains limited. Key pending challenges include defect and raw material impurity (like C/N/O) control, post-AM heat treatment design, sintering-shrinkage/warpage management, and pixel-level energy-distribution control (for area printing). To address these concerns, several research directions merit priority. For instance, for binder jetting AM, it is pivotal to develop powder/binder qualification, coupled with mechanistic-statistical models that relate impurity uptake during debinding and sintering to densification and mechanical performances in titanium alloys. In addition, for area printing, establishing how areal energy distribution and pulse structure manipulate microstructure (like prior- β morphology, α -lath thickness, and crystallographic texture) is recommended. Since the exposure paradigm differs from conventional point/line-scanned fusion AM processes, such understanding would enable pixel-/region-level microstructure control and, in turn, could lead to development of AM titanium alloys with high fatigue and damage tolerance performances.

CRediT authorship contribution statement

Hamish L. Fraser: Validation, Resources. **Peter Hodgson:** Resources, Investigation. **Martin Heilmaier:** Resources, Conceptualization. **Alberto Boretti:** Writing – review & editing. **Yuman Zhu:** Writing – review & editing, Validation, Supervision, Project administration, Conceptualization. **Aijun Huang:** Writing – review & editing,

Supervision, Project administration, Funding acquisition. **Jianwen Liu:** Writing – review & editing, Writing – original draft, Validation, Methodology, Investigation, Conceptualization. **Kai Zhang:** Writing – review & editing, Writing – original draft, Methodology, Investigation, Funding acquisition. **Michael J. Bermingham:** Writing – review & editing, Investigation.

Declaration of Generative AI and AI-assisted technologies in the writing process

Generative AI and AI-assisted technologies have been used to improve the language and readability of the paper.

Declaration of Competing Interest

The author declares no known competing financial interests or personal relationships that could have appeared to influence the work reported in this paper.

Acknowledgments

The authors are very grateful to Australia Research Council (ARC) Discovery Project (DP230100995), ARC Linkage Projects (LP220100400), and National Natural Science Foundation of China (No. 52405396 and No. U24A2036) program for funding support.

Data availability

Data will be made available on request.

References

- [1] C. Zhang, S. Wang, J. Li, Y. Zhu, T. Peng, H. Yang, *Addit. Manuf.* 36 (2020) 101490.
- [2] T. DebRoy, H.L. Wei, J.S. Zuback, T. Mukherjee, J.W. Elmer, J.O. Milewski, A.M. Beese, A. Wilson-Heid, A. De, W. Zhang, *Prog. Mater. Sci.* 92 (2018) 112–224.
- [3] T. DebRoy, T. Mukherjee, H.L. Wei, J.W. Elmer, J.O. Milewski, *Nat. Rev. Mater.* 6 (2021) 48–68.
- [4] D. Gu, X. Shi, R. Poprawe, D.L. Bourell, R. Setchi, *Science* 372 (2021).
- [5] S.M. Yusuf, S. Cutler, N. Gao, *Metals* 9 (2019).
- [6] A. Gisario, M. Kazarian, F. Martina, M. Mehrpouya, *J. Manuf. Syst.* 53 (2019) 124–149.
- [7] L. Mearian, *Comput. World* (2017).
- [8] Y. Zhu, K. Zhang, Z. Meng, K. Zhang, P. Hodgson, N. Birbilis, M. Weyland, H. L. Fraser, S.C.V. Lim, H. Peng, R. Yang, H. Wang, A. Huang, *Nat. Mater.* 21 (2022) 1258–1262.
- [9] T.M. Smith, C.A. Kantzios, N.A. Zarkevich, B.J. Harder, M. Heczko, P.R. Gradi, A. C. Thompson, M.J. Mills, T.P. Gabb, J.W. Lawson, *Nature* 617 (2023) 513–518.
- [10] J.H. Martin, B.D. Yahata, J.M. Hundley, J.A. Mayer, T.A. Schaeder, T.M. Pollock, *Nature* 549 (2017) 365–369.
- [11] Y.M. Wang, T. Voisin, J.T. McKeown, J. Ye, N.P. Calta, Z. Li, Z. Zeng, Y. Zhang, W. Chen, T.T. Roehling, R.T. Ott, M.K. Santala, P.J. Depond, M.J. Matthews, A. V. Hamza, T. Zhu, *Nat. Mater.* 17 (2018) 63–70.
- [12] G. Lütjering, J.C. Williams, *Titanium*, 2nd Edition, Springer Berlin Heidelberg, 2007.
- [13] X. Wu, *Mater. Sci. Technol.* 23 (2007) 631–640.
- [14] K. Sertoglu, *3D Print. Ind.* (2022).
- [15] B. Jackson, *3D Print. Ind.* (2019).
- [16] L. Wang, Y. Li, L. Zhou, Y. Lou, S. Liu, D. Zheng, M. Yi, *Mater. Res. Lett.* 11 (2023) 973–1012.
- [17] M.C. Zang, H.Z. Niu, S. Liu, R.Q. Guo, D.L. Zhang, *Addit. Manuf.* 65 (2023) 103444.
- [18] Q. Pan, L. Lu, *Nat. Mater.* (2025).
- [19] Q. Tan, M. Zhang, *Mater. Sci. Eng. R. Rep.* 158 (2024) 100773.
- [20] J. Zhang, M.J. Bermingham, J. Otte, Y. Liu, Z. Hou, N. Yang, Y. Yin, M. Bayat, W. Lin, X. Huang, D.H. Stjohn, M.S. Dargusch, *Science* 645 (2024) 639–645.
- [21] N. Sanaei, A. Fatemi, *Prog. Mater. Sci.* (2020) 100724.
- [22] P. Kumar, O. Prakash, U. Ramamurty, *Acta Mater.* 154 (2018) 246–260.
- [23] R. Gandhi, L. Macchioni, F. Concl, *Appl. Sci.* 12 (2022).
- [24] S.J. Findlay, N.D. Harrison, *Mater. Today* 5 (2002) 18–25.
- [25] K. Lu, *Science* (80.) 328 (2010) 319–320.
- [26] U. Zerbst, G. Bruno, J.Y. Buffière, T. Wegener, T. Niendorf, T. Wu, X. Zhang, N. Kashaei, G. Meneghetti, N. Hrabe, M. Madia, T. Werner, K. Hilgenberg, M. Koukolíková, R. Procházka, J. Džugan, B. Möller, S. Beretta, A. Evans, R. Wagener, K. Schnabel, *Prog. Mater. Sci.* 121 (2021) 1–73.
- [27] M.J. Paul, J.J. Kruzic, U. Ramamurty, B. Gludovatz, *Acta Mater.* 276 (2024) 120061.
- [28] T.H. Becker, P. Kumar, U. Ramamurty, *Acta Mater.* (2021) 117240.
- [29] H. Liu, H. Yu, C. Guo, X. Chen, S. Zhong, L. Zhou, A. Osman, J. Lu, *Adv. Mater.* 36 (2024).
- [30] H. Javidrad, B. Koc, H. Bayraktar, U. Simsek, K. Gunaydin, *Virtual Phys. Prototyp.* 19 (2024) 1–48.
- [31] R. Molaei, A. Fatemi, N. Sanaei, J. Pegues, N. Shamsaei, S. Shao, P. Li, D. H. Warner, N. Phan, *Int. J. Fatigue* 132 (2020).
- [32] B. Fotovati, N. Namdari, A. Dehghanhadikolaei, *Mater. Res. Express* 6 (2019).
- [33] A. Fatemi, R. Molaei, J. Simsiriwong, N. Sanaei, J. Pegues, B. Torries, N. Phan, N. Shamsaei, *Fatigue Fract. Eng. Mater. Struct.* 42 (2019) 991–1009.
- [34] A.H. Chern, P. Nandwana, T. Yuan, M.M. Kirk, R.R. Dehoff, P.K. Liaw, C.E. Duty, *Int. J. Fatigue* 119 (2019) 173–184.
- [35] D. Pede, M. Li, L. Virovac, T. Poleske, F. Balle, C. Müller, H. Mozaffari-Jovein, *J. Mater. Res. Technol.* 19 (2022) 4598–4612.
- [36] X. Luo, D.D. Li, C. Yang, A. Gebert, H.Z. Lu, T. Song, H.W. Ma, L.M. Kang, Y. Long, Y.Y. Li, *Addit. Manuf.* 51 (2022).
- [37] W. Wang, C. Chen, R. Zhao, B. Gludovatz, X. Lu, K. Zhang, S. Shuai, T. Hu, S. Xu, J. Wang, Z. Ren, *Mater. Sci. Eng. A* 890 (2024) 145863.
- [38] B. Denkena, J.K. Hufenbach, B. Bergmann, U. Kühn, A. Heckemeyer, S. Worpenberg, C. Kunz, *CIRP J. Manuf. Sci. Technol.* 55 (2024) 42–53.
- [39] Q. Duan, S. Wang, S. Li, Y. Ma, X. Shao, R. Yang, *Nature* 626 (2024).
- [40] M.S. Hosseini, E. Vaghefi, E. Mirkoohi, *J. Manuf. Process* 102 (2023) 549–563.
- [41] J. Zhang, Y. Liu, G. Sha, S. Jin, Z. Hou, M. Bayat, N. Yang, Q. Tan, Y. Yin, S. Liu, J. H. Hattel, M. Dargusch, X. Huang, M. Zhang, *Nat. Commun.* (2022) 1–10.
- [42] K.K. Sankaran, R.S. Mishra, *Metallurgy and Design of Alloys with Hierarchical Microstructures*, Elsevier, 2017, pp. 177–288.
- [43] M.J. Donachie, *Titanium: A Technical Guide*, ASM International, 2000.
- [44] I. Weiss, S.L. Semiatin, *Mater. Sci. Eng. A* 263 (1999) 243–256.
- [45] J.P. Immarigeon, R.T. Holt, A.K. Koul, L. Zhao, W. Wallace, J.C. Beddoes, *Mater. Charact.* 35 (1995) 41–67.
- [46] Q.Y. Sun, H.C. Gu, *Mater. Sci. Eng. A* 316 (2001) 80–86.
- [47] M.C. Zang, H.Z. Niu, J.S. Yu, H.R. Zhang, T.B. Zhang, D.L. Zhang, *Mater. Sci. Eng. A* 840 (2022).
- [48] L.C. Zhang, L.Y. Chen, S. Zhou, Z. Luo, *J. Alloy. Compd.* 936 (2023) 168099.
- [49] R.R. Boyer, *Jom* 46 (1994) 20–23.
- [50] J.D. Cotton, R.D. Briggs, R.R. Boyer, S. Tamirisakandala, P. Russo, N. Shchetnikov, J.C. Fanning, *Jom* 67 (2015) 1281–1303.
- [51] T. Zhang, Z. Huang, T. Yang, H. Kong, J. Luan, A. Wang, *Science* 482 (2021) 478–482.
- [52] Z. Snow, A.R. Nassar, E.W. Reutzel, *Addit. Manuf.* 36 (2020) 101457.
- [53] M. Brandt, *The Role of Lasers in Additive Manufacturing*, Elsevier Ltd, 2017.
- [54] D. Herzog, V. Seyda, E. Wycisk, C. Emmelmann, *Acta Mater.* 117 (2016) 371–392.
- [55] C. Qiu, G. a Ravi, C. Dance, A. Ranson, S. Dilworth, M.M. Attallah, *J. Alloy. Compd.* 629 (2015) 351–361.
- [56] M.E. Smith, *MATEC Web Conf.* (2020) 16–19.
- [57] Z. Chen, X. Wu, D. Tomus, C.H.J. Davies, *Addit. Manuf.* 21 (2018) 91–103.
- [58] G. Del Guercio, M. Galati, A. Saboori, P. Fino, L. Iuliano, *Acta Metall. Sin. (Engl. Lett.)* 33 (2020) 183–203.
- [59] D. Zhang, S. Sun, D. Qiu, M.A. Gibson, M.S. Dargusch, M. Brandt, M. Qian, M. Easton, *Adv. Eng. Mater.* 20 (2018) 1–20.
- [60] M. Galati, L. Iuliano, *Addit. Manuf.* 19 (2018) 1–20.
- [61] P. Li, D.H. Warner, A. Fatemi, N. Phan, *Int. J. Fatigue* 85 (2016) 130–143.
- [62] X. Tan, Y. Kok, Y. Tan, M. Descoings, D. Mangelinck, S.B. Tor, K.F. Leong, C. K. Chua, *Acta Mater.* 97 (2015) 1–16.
- [63] D. Svetilizky, M. Das, B. Zheng, A.L. Vyatskikh, S. Bose, A. Bandyopadhyay, J. M. Schoenung, E.J. Lavernia, N. Eliaz, *Mater. Today* 49 (2021) 271–295.
- [64] S. Liu, Y.C. Shin, *Mater. Des.* 164 (2019) 107552.
- [65] Z. Lin, K. Song, X. Yu, *J. Manuf. Process* 70 (2021) 24–45.
- [66] R. Li, J. Xiong, Y. Lei, *J. Manuf. Process* 40 (2019) 59–67.
- [67] J. Wang, X. Lin, M. Wang, J. Li, C. Wang, W. Huang, *Mater. Sci. Eng. A* 776 (2020) 139020.
- [68] J. Donoghue, A.A. Antonysamy, F. Martina, P.A. Colegrove, S.W. Williams, P. B. Prangnell, *Mater. Charact.* 114 (2016) 103–114.
- [69] D. Ding, Z. Pan, D. Cuiuri, H. Li, *Robot. Comput. Integr. Manuf.* 34 (2015) 8–19.
- [70] T. Mutharamalingam, K. Moiduddin, R. Akash, S. Krishnan, S. Hammad Mian, W. Ameen, H. Alkhalefah, *Opt. Laser Technol.* 132 (2020) 2017–2020.
- [71] A. Simchi, F. Petzoldt, T. Hartwig, S.B. Hein, B. Barthel, L. Reineke, *Int. J. Adv. Manuf. Technol.* 127 (2023) 1541–1558.
- [72] E. Stevens, S. Schloeder, E. Bono, D. Schmidt, M. Chmielus, *Addit. Manuf.* 22 (2018) 746–752.
- [73] M. Li, W. Du, A. Elwany, Z. Pei, C. Ma, *J. Manuf. Sci. Eng. Trans. ASME* 142 (2020) 1–7.
- [74] M.T. Hasib, H.E. Ostergaard, Q. Liu, X. Li, J.J. Kruzic, *Addit. Manuf.* 45 (2021) 102027.
- [75] S. Huang, B. Sun, S. Guo, *Opt. Laser Technol.* 144 (2021) 107422.
- [76] K. Wei, Z. Wang, X. Zeng, *Mater. Sci. Eng. A* 709 (2018) 301–311.
- [77] H. Fan, S. Yang, *Mater. Sci. Eng. A* 788 (2020) 139533.
- [78] Z. Zhu, F.L. Ng, H.L. Seet, S.M.L. Nai, *J. Alloy. Compd.* 895 (2022) 162648.
- [79] S. Sui, Y. Chew, Z. Hao, F. Weng, C. Tan, Z. Du, G. Bi, *Adv. Powder Mater.* (2021) 100002.
- [80] M. Galati, S. Defanti, A. Saboori, G. Rizza, E. Tognoli, N. Vincenzi, A. Gatto, L. Iuliano, *Addit. Manuf.* 50 (2022).
- [81] C. Fleißner-Rieger, T. Pfeifer, C. Turk, H. Clemens, *Materials* 15 (2022).

- [82] S.J. Han, G.B. Bang, W.R. Kim, G.H. Kim, H.S. Kang, H.S. Han, T.W. Lee, H. G. Kim, J. Mater. Res. Technol. 27 (2023) 200–208.
- [83] R.D. Fischer, G.C. Harvill, R. Zhao, H. Talebinezhad, B.C. Prorok, Mater. Sci. Eng. A 892 (2024) 146088.
- [84] S. Zhang, Y. Zhang, Z. Zou, Y. Shi, Y. Zang, Mater. Sci. Eng. A 831 (2022) 142241.
- [85] H. Fan, Y. Liu, S. Yang, J. Micromech. Mol. Phys. 6 (2021).
- [86] H.K. Park, T.W. Na, J.M. Park, Y. Kim, G.H. Kim, B.S. Lee, H.G. Kim, J. Alloy. Compd. 796 (2019) 300–306.
- [87] C. Cai, X. Wu, W. Liu, W. Zhu, H. Chen, J.C.D. Qiu, C.N. Sun, J. Liu, Q. Wei, Y. Shi, J. Mater. Sci. Technol. 57 (2020) 51–64.
- [88] R. Li, H. Wang, B. He, Z. Li, Y. Zhu, D. Zheng, X. Tian, S. Zhang, Mater. Sci. Eng. A 824 (2021) 141771.
- [89] L. Zhang, P. Dong, S. Chen, Y. Wang, H. Yao, Y. Zeng, J. Chen, J. Alloy. Compd. 945 (2023) 169292.
- [90] M. Lopez, C. Pickett, E. Arrieta, L.E. Murr, R.B. Wicker, M. Ahlfors, D. Godfrey, F. Medina, Materials 13 (2020).
- [91] S. Cao, R. Chu, X. Zhou, K. Yang, Q. Jia, C.V.S. Lim, A. Huang, X. Wu, J. Alloy. Compd. 744 (2018) 357–363.
- [92] J. Wang, X. Lin, J. Li, Y. Hu, Y. Zhou, C. Wang, Q. Li, W. Huang, Mater. Sci. Eng. A 754 (2019) 735–749.
- [93] T. Voisin, N.P. Calta, S.A. Khairallah, J.B. Forien, L. Balogh, R.W. Cunningham, A. D. Rollett, Y.M. Wang, Mater. Des. 158 (2018) 113–126.
- [94] Q. Yan, B. Chen, N. Kang, X. Lin, S. Lv, K. Kondoh, S. Li, J.S. Li, Mater. Charact. 164 (2020).
- [95] C. Qiu, N.J.E. Adkins, M.M. Attallah, Mater. Sci. Eng. A 578 (2013) 230–239.
- [96] J. Karlsson, T. Sjögren, A. Snis, H. Engqvist, J. Lausmaa, Mater. Sci. Eng. A 618 (2014) 456–461.
- [97] O.L. Rodriguez, P.G. Allison, W.R. Whittington, H. El Kadiri, O.G. Rivera, M. E. Barkey, Mater. Sci. Eng. A 713 (2018) 125–133.
- [98] R. Sepe, S. Franchitti, R. Borrelli, F. Di Caprio, E. Armentani, F. Caputo, Theor. Appl. Fract. Mech. 107 (2020) 102519.
- [99] K. Zhang, X. Tian, M. Bermingham, J. Rao, Q. Jia, Y. Zhu, X. Wu, S. Cao, A. Huang, Mater. Des. 184 (2019).
- [100] B.E. Carroll, T.A. Palmer, A.M. Beese, Acta Mater. 87 (2015) 309–320.
- [101] A. Xue, X. Lin, L. Wang, J. Wang, W. Huang, Mater. Des. 181 (2019) 107943.
- [102] B. Wu, Z. Pan, D. Ding, D. Cuiurl, H. Li, Z. Fei, J. Mater. Process. Technol. 258 (2018) 97–105.
- [103] J. Lin, Y. Lv, D. Guo, X. Wu, Z. Li, C. Liu, B. Guo, G. Xu, B. Xu, Mater. Sci. Eng. A 759 (2019) 288–297.
- [104] Q. Liu, Y. Wang, H. Zheng, K. Tang, L. Ding, H. Li, S. Gong, Mater. Sci. Eng. A 660 (2016) 24–33.
- [105] M. Simionelli, Y.Y. Tse, C. Tuck, Mater. Sci. Eng. A 616 (2014) 1–11.
- [106] R. Schur, S. Ghods, C. Wisdom, R. Pahuja, A. Montelione, D. Arola, M. Ramulu, Mater. Des. 200 (2021) 109450.
- [107] A. Mohammadhoseini, D. Fraser, S.H. Masood, M. Jahedi, Mater. Res. Innov. 17 (2013).
- [108] H. Galarraga, R.J. Warren, D.A. Lados, R.R. Dehoff, M.M. Kirka, P. Nandwana, Mater. Sci. Eng. A 685 (2017) 417–428.
- [109] X. Tian, Y. Zhu, C.V.S. Lim, J. Williams, R. Boyer, X. Wu, K. Zhang, A. Huang, Addit. Manuf. 46 (2021) 102151.
- [110] Y. Cai, Z. Peng, J. Chen, H. Chen, J. Xiong, Mater. Sci. Eng. A 893 (2024) 146144.
- [111] J.M. Alegre, Á. Díaz, R. García, L.B. Peral, M. Lorenzo-Bañuelos, I.I. Cuesta, Mater. (Basel) 17 (2024).
- [112] B. Ou, L. Lu, X. Meng, Q. He, Y. Xie, J. Yan, J. Laser Appl. 35 (2023) 0–16.
- [113] Z. Liu, Z.X. Qin, F. Liu, X. Lu, H.M. Wang, Mater. Charact. 97 (2014) 132–139.
- [114] Y. Zhu, X. Tian, J. Li, H. Wang, Mater. Des. 67 (2015) 538–542.
- [115] Y. Xie, R. Zhang, Z. Yan, C. Feng, Z. Luo, X. Liang, J. Ni, Q. Zhou, F. Wang, Mater. Sci. Eng. A 902 (2024) 146021.
- [116] C. Wang, J.Z. Yi, G. Yang, J.X. Wang, J.B. Wu, Z. Zhu, C.X. Wang, Mater. Res. Express 11 (2024).
- [117] Z. Liu, C. Wang, J. Yi, Y. Yu, B. Yu, G. Yang, J. Phys. Conf. Ser. 1965 (2021).
- [118] H. Yu, F. Li, Z. Wang, X. Zeng, Int. J. Fatigue 120 (2019) 175–183.
- [119] S. Zhou, J. Zhang, Y. Wang, B. Li, D. An, S. Zhou, G. Yang, Mater. Charact. 212 (2024).
- [120] J.S. Keist, S. Nayir, T.A. Palmer, Mater. Sci. Eng. A 787 (2020).
- [121] J.S. Keist, T.A. Palmer, Mater. Des. 106 (2016) 482–494.
- [122] D. Li, H. Huang, C. Chen, S. Liu, X. Liu, X. Zhang, K. Zhou, Mater. Sci. Eng. A 814 (2021) 141245.
- [123] H.D. Carlton, K.D. Klein, J.W. Elmer, Sci. Technol. Weld. Join. 24 (2019) 465–473.
- [124] J. Zhang, M. Bermingham, J. Otte, Y. Liu, M. Dargusch, Scr. Mater. 223 (2023).
- [125] D. Sharma, S.R. Kada, D. Fabijanic, D. Parfitt, B. Chen, B. Roebuck, M. E. Fitzpatrick, M.R. Barnett, Addit. Manuf. 48 (2021).
- [126] H. Schwab, F. Palm, U. Kühn, J. Eckert, Mater. Des. 105 (2016) 75–80.
- [127] A. Caballero, A.E. Davis, J.R. Kennedy, J. Fellowes, A. Garner, S. Williams, P. Prangnell, Philos. Mag. (2022).
- [128] H. Deng, W. Qiu, L. Chen, S. Cao, Y. Wei, Z. Hu, X. Cui, J. Tang, Adv. Eng. Mater. 2100265 (2021) 1–7.
- [129] H. Deng, W. Qiu, S. Cao, L. Chen, Z. Hu, Y. Wei, Z. Xia, L. Zhou, X. Cui, J. Tang, J. Alloy. Compd. 858 (2021) 158351.
- [130] H. Deng, L. Chen, W. Qiu, Z. Zheng, Y. Tang, Z. Hu, Y. Wei, Z. Xia, G. Le, J. Tang, X. Cui, J. Alloy. Compd. 810 (2019) 151792.
- [131] H. Deng, S. Cao, J.C. Williams, L. Chen, W. Qiu, L. Zhou, J. Tang, Mater. Sci. Eng. A 825 (2020) 141914.
- [132] T. Zhang, H. Huang, S.R.E. Hosseini, W. Chen, F. Li, C. Chen, K. Zhou, Mater. Sci. Eng. A 835 (2022) 142624.
- [133] H. Huang, T. Zhang, C. Chen, S.R.E. Hosseini, J. Zhang, K. Zhou, Materials (2022) 15.
- [134] C.M. Liu, H.M. Wang, X.J. Tian, H.B. Tang, Mater. Sci. Eng. A 590 (2014) 30–36.
- [135] C.M. Liu, H.M. Wang, X.J. Tian, D. Liu, Mater. Sci. Eng. A 604 (2014) 176–182.
- [136] S. Wang, B. He, H. Tang, Mater. Sci. Eng. A 893 (2024) 146142.
- [137] G. Zhang, H. Xiong, H. Yu, R. Qin, W. Liu, H. Yuan, Mater. Des. 195 (2020) 109063.
- [138] Y. Zhu, K. Zhang, Z. Meng, K. Zhang, P. Hodgson, N. Birbilis, M. Weyland, H. L. Fraser, S.C.V. Lim, H. Peng, R. Yang, H. Wang, A. Huang, Nat. Mater. (2022).
- [139] K. Zhang, W. Hao, Y. Zhu, S. Chao, V. Lim, X. Gao, C. Kit, C. Bai, A. Huang, Mater. Des. 224 (2022) 111325.
- [140] A. Carrozza, A. Aversa, P. Fino, M. Lombardi, Mater. Des. 215 (2022) 110512.
- [141] R. Duan, S. Li, B. Cai, W. Zhu, F. Ren, M.M. Attallah, Addit. Manuf. 37 (2021) 101708.
- [142] P. Li, C. Liu, J. Wang, J. Lu, S. Ma, H. Fan, IOP Conf. Ser. Mater. Sci. Eng. 563 (2019) 022025.
- [143] A. Carrozza, A. Aversa, P. Fino, M. Lombardi, J. Alloy. Compd. 870 (2021) 159329.
- [144] P.A. Kobryn, S.L. Semiatin, Solid Free. Fabr. Proc. (2001) 179–186.
- [145] Y.X. Liu, W. Chen, Z.Q. Li, B. Tang, X.Q. Han, G. Yao, Int. J. Fatigue 97 (2017) 79–87.
- [146] A. Yadollahi, N. Shamsaei, Int. J. Fatigue 98 (2017) 14–31.
- [147] D. Greitemeier, C. Dalle Donne, A. Schoberth, M. Jürgens, J. Eufinger, T. Melz, Appl. Mech. Mater. 807 (2015) 169–180.
- [148] M. Kahlin, H. Ansell, D. Basu, A. Kerwin, L. Newton, B. Smith, J.J. Moverare, Int. J. Fatigue 134 (2020) 105497.
- [149] E. Wycisk, A. Solbach, S. Siddique, D. Herzog, F. Walther, C. Emmelmann, Physics Procedia Elsevier B.V., 2014, pp. 371–378.
- [150] D. Greitemeier, F. Palm, F. Syassen, T. Melz, Int. J. Fatigue 94 (2017) 211–217.
- [151] R. Biswal, X. Zhang, A.K. Syed, M. Awd, J. Ding, F. Walther, S. Williams, Int. J. Fatigue 122 (2019) 208–217.
- [152] A.J. Sterling, B. Torres, N. Shamsaei, S.M. Thompson, D.W. Seely, Mater. Sci. Eng. A 655 (2016) 100–112.
- [153] N. Hrabe, T. Gnäupel-Herold, T. Quinn, Int. J. Fatigue 94 (2017) 202–210.
- [154] A. Baća, R. Konečná, G. Nicoletto, L. Kunz, Mater. Today Proc. 3 (2016) 921–924.
- [155] G. Nicoletto, Int. J. Fatigue 94 (2017) 255–262.
- [156] P. Edwards, M. Ramulu, Mater. Sci. Eng. A 598 (2014) 327–337.
- [157] A. Bandyopadhyay, M. Upadhyayula, K.D. Traxel, B. Onuike, Mater. Lett. 255 (2019) 126541.
- [158] T. Vilaro, C. Colin, J.D. Bartout, Metall. Mater. Trans. A Phys. Metall. Mater. Sci. 42 (2011) 3190–3199.
- [159] W. Sun, Y. Ma, W. Huang, W. Zhang, X. Qian, Int. J. Fatigue 130 (2020).
- [160] K. Chang, E. Liang, W. Huang, X. Zhang, Y. Chen, J. Dong, R. Zhang, Mater. Lett. 267 (2020) 127516.
- [161] V. Chastand, A. Tezenas, Y. Cadoret, P. Quaegebeur, W. Maia, E. Charkaluk, Procedia Struct. Integr. 2 (2016) 3168–3176.
- [162] V.D. Le, E. Pessard, F. Morel, F. Edy, Eng. Fract. Mech. 214 (2019) 410–426.
- [163] C.W. Lin, C.P. Ju, J.H. Chern Lin, Biomaterials 26 (2005) 2899–2907.
- [164] M. Boyer, Atlas of Fatigue Curves, American Society for Metals, 1986.
- [165] H. Lv, Z. Zhang, Y. Chen, Y. Liu, H. Chen, Y. Chen, J. Cheng, J. She, H. He, J. Chen, Mater. Sci. Eng. A 853 (2022) 143745.
- [166] T. Persenot, A. Burr, G. Martin, J.Y. Buffiere, R. Dendievle, E. Maire, Int. J. Fatigue 118 (2019) 65–76.
- [167] A.K. Syed, X. Zhang, A. Caballero, M. Shamir, S. Williams, Int. J. Fatigue 149 (2021) 106268.
- [168] A.H. Chern, P. Nandwana, T. Yuan, M.M. Kirka, R.R. Dehoff, P.K. Liaw, C.E. Duty, Int. J. Fatigue 119 (2019) 173–184.
- [169] Z. Qu, Z. Zhang, R. Liu, Z. Zhang, Sci. Adv. 11 (2025) eady0937.
- [170] J. Zhang, X. Kong, S. Ma, D. Liu, X. Wang, J. Feng, H. Wang, ACTA Aeronaut. Astronaut. Sin. 42 (2021) 525430.
- [171] H. Ruijun, W. Huaming, ACTA Aeronaut. Astronaut. Sin. 31 (2010) 1488–1493.
- [172] X. Wang, X. He, T. Wang, Y. Li, Addit. Manuf. 28 (2019) 373–393.
- [173] Q. Lanyun, W. Jiabao, W. Wei, W. Chao, L. Changfu, Y. Guang, Chin. J. Lasers 47 (2020) 1002008 (in chinese).
- [174] Z. Liu, P. Liu, L. Wang, Y. Lu, X. Lu, Z.X. Qin, H.M. Wang, Mater. Sci. Eng. A 716 (2018) 140–149.
- [175] S. Lu, R. Bao, K. Wang, D. Liu, Y. Wu, B. Fei, Mater. Sci. Eng. A 690 (2017) 378–386.
- [176] X. Wang, X. He, T. Wang, Y. Li, Addit. Manuf. 35 (2020) 101174.
- [177] J. Cao, F. Weng, S. Zhang, H. Wang, J. Zhang, Int. J. Fatigue 195 (2025) 108869.
- [178] J. CAO, F. WENG, S. MA, S. ZHANG, J. ZHANG, Chin. J. Aeronaut. 38 (2025) 103514.
- [179] H.C. Kaushik, K. Dyer, M.H. Korayem, R. Molaei, A. Hadadzadeh, Fatigue Fract. Eng. Mater. Struct. (2025) 3287–3302.
- [180] Z.J. Casias, P. Kumar, J. Pegues, J. Buckner, R. Craig, J.D. Carroll, Mater. Sci. Eng. A 912 (2024) 146932.
- [181] K. Majchrowicz, A. Chmielewska, B. Wysocki, S. Przybysz-Gloc, M. Kulczyk, H. Garbacz, Z. Pakiela, Crystals 13 (2023).
- [182] Y. Gao, R. Guo, M. Cheng, C. Zhang, Y. Zhou, C. Cai, Y. Shi, L. Xu, R. Yang, Z. Wang, SSRN (2025).
- [183] M. Hein, Crystals 12 (2022).
- [184] J. Hendl, A.T. Zeuner, S. Schettler, A. Marquardt, C. Leyens, M. Zimmermann, Prog. Addit. Manuf. 10 (2025) 3615–3627.
- [185] M. Karoluk, K. Kobiela, M. Madeja, R. Dziedzic, G. Ziolkowski, T. Kurzynowski, Materials 16 (2023).
- [186] X. Shi, W. Zeng, S. Xue, Z. Jia, J. Alloy. Compd. 631 (2015) 340–349.

- [187] B. Yu, P. Wang, P. Zhao, X. Song, M.J. SaGong, H.S. Kim, Eng. Fail. Anal. 174 (2025) 109480.
- [188] D. Tang, X. He, B. Wu, L. Dang, H. Xin, Y. Li, Mater. Sci. Eng. A 876 (2023) 145112.
- [189] D. Tang, X. He, B. Wu, X. Wang, T. Wang, Y. Li, Theor. Appl. Fract. Mech. 119 (2022) 103322.
- [190] V. Nesterenkov, S. Akhonin, I. Klochkov, V. Matviichuk, V. Berezos, S. Motrunich, Weld. World 69 (2025) 717–725.
- [191] F. Zakir, A.K. Syed, X. Zhang, A.E. Davis, V.K. Sahu, A.E. Caballero, R. Biswal, P. B. Prangnell, S. Williams, Addit. Manuf. 105 (2025) 104785.
- [192] M.S. Yasin, A. Jam, M. Habibnejad-Korayem, M. Haghshenas, S. Shao, N. Shamsaei, Int. J. Fatigue 187 (2024) 108426.
- [193] B. Wu, J. Huang, G. Yang, Y. Ren, S. Zhou, D. An, Surf. Coat. Technol. 446 (2022).
- [194] M. Bezuidenhout, G. Ter Haar, T. Becker, S. Rudolph, O. Damm, N. Sacks, Mater. Today Commun. 25 (2020) 101396.
- [195] S. Aguado-Montero, C. Navarro, J. Vázquez, F. Lasagni, S. Slawik, J. Domínguez, Int. J. Fatigue 154 (2022).
- [196] H. Soyama, C. Kuji, Surf. Coat. Technol. 451 (2022) 129047.
- [197] W. Eric, E. Claus, S. Shafaqat, W. Frank, Adv. Mater. Res. 816–817 (2013) 134–139.
- [198] T.H. Becker, N.M. Dhansay, G.M. Ter Haar, K. Vanmeensel, Acta Mater. 197 (2020) 269–282.
- [199] Y. Zhai, D.A. Lados, E.J. Brown, G.N. Vigilante, Int. J. Fatigue 93 (2016) 51–63.
- [200] Y. Xie, M. Gong, Q. Zhou, Q. Li, F. Wang, X. Zeng, M. Gao, Mater. Sci. Eng. A 826 (2021) 141942.
- [201] Y. Xie, M. Gao, F. Wang, C. Zhang, K. Hao, H. Wang, X. Zeng, Mater. Sci. Eng. A 709 (2018) 265–269.
- [202] M. Kahlin, H. Ansell, J. Moverare, Int. J. Fatigue 155 (2022) 106608.
- [203] B.L. Boyce, R.O. Ritchie, Eng. Fract. Mech. 68 (2001) 129–147.
- [204] Z.H. Jiao, R.D. Xu, H.C. Yu, X.R. Wu, Procedia Struct. Integr. 7 (2017) 124–132.
- [205] P. Kumar, U. Ramamurty, Acta Mater. 169 (2019) 45–59.
- [206] M. Tarik Hasib, H.E. Ostergaard, X. Li, J.J. Kruzeic, Int. J. Fatigue 142 (2021) 105955.
- [207] T.H. Becker, P. Kumar, U. Ramamurty, Acta Mater. 219 (2021) 117240.
- [208] V. Cain, L. Thijis, J. Van Humbeeck, B. Van Hooreweder, R. Knutsen, Addit. Manuf. 5 (2015) 68–76.
- [209] H.R. Sandgren, Y. Zhai, D.A. Lados, P.A. Shade, J.C. Schuren, M.A. Groeber, P. Kenesei, A.G. Gavras, Addit. Manuf. 12 (2016) 132–141.
- [210] M. Seifi, A. Salem, D. Satko, J. Shaffer, J.J. Lewandowski, Int. J. Fatigue 94 (2017) 263–287.
- [211] E. Lorant, Effect of Microstructure on Mechanical Properties of Ti-6Al-4V Structures Made by Additive Layer Manufacturing, Cranfield University, 2010.
- [212] Y. Xie, M. Gong, Z. Luo, Q. Li, M. Gao, F. Wang, X. Zeng, G. Wang, Mater. Charact. 177 (2021) 111183.
- [213] R. VanSickle, D. Foehring, H.B. Chew, J. Lambros, Mater. Sci. Eng. A 795 (2020) 139993.
- [214] J. Zhang, X. Zhang, X. Wang, J. Ding, Y. Traoré, S. Paddea, S. Williams, Mater. Des. 104 (2016) 365–375.
- [215] S. Lu, R. Bao, K. Wang, D. Liu, Y. Wu, B. Fei, Mater. Sci. Eng. A 690 (2017) 378–386.
- [216] K. Wang, R. Bao, T. Zhang, B. Liu, Z. Yang, B. Jiang, Int. J. Fatigue 124 (2019) 217–226.
- [217] Y. Wang, R. Chen, X. Cheng, Y. Zhu, J. Zhang, H. Wang, J. Mater. Sci. Technol. 35 (2019) 403–408.
- [218] X. Wang, M. Cao, Y. Zhao, J. He, X. Guan, Int. J. Plast. 179 (2024) 104034.
- [219] G. Liu, Q. Zhao, W. Jia, Y. Zhang, S. Song, C. Mao, W. Zhou, S. Zhang, Y. Zhao, J. Alloy. Compd. 1026 (2025) 178937.
- [220] K. Wang, R. Bao, B. Jiang, Y. Wu, D. Liu, C. Yan, Int. J. Fatigue 116 (2018) 535–542.
- [221] G. Liu, Q. Zhao, W. Jia, Y. Zhang, S. Song, C. Mao, W. Zhou, S. Zhang, Y. Zhao, J. Mater. Res. Technol. 31 (2024) 579–592.
- [222] G. Lütjering, Mater. Sci. Eng. A 243 (1998) 32–45.
- [223] K.S. Ravichandran, A.K. Vasudevan, Fracture Resistance of Structural Alloys, ASM International, 1996.
- [224] N.M. Dhansay, R. Tait, T. Becker, Adv. Mater. Res. 1019 (2014) 248–253.
- [225] M. Seifi, M. Dahir, R. Aman, O. Harrysson, J. Beuth, J.J. Lewandowski, Jom 67 (2015) 597–607.
- [226] P. Edwards, A. O'Conner, M. Ramulu, J. Manuf. Sci. Eng. Trans. ASME 135 (2013).
- [227] X. Zhang, F. Martina, J. Ding, X. Wang, S.W. Williams, Fatigue Fract. Eng. Mater. Struct. 40 (2017) 790–803.
- [228] M. Xie, S. Huang, Z. Wang, U. Ramamurty, Acta Mater. 277 (2024) 120211.
- [229] Y. He, K. Zhao, Y. Zhang, K.G. Prashanth, Z. Ye, Z. Yu, F. Zhang, Mater. Sci. Eng. A 924 (2025) 147822.
- [230] J. Zhang, X. Kong, S. Ma, D. Liu, X. Wang, J. Feng, Acta Aeronaut. Astronaut. Sin. 42 (2021) 460–470.
- [231] S. Wang, J. Zhong, S. Li, X. Zhang, Z. Wang, H. Yang, D. Wu, Metals 2713 (2024).
- [232] X. Xue, Y. Ou, H. Chang, W. Wang, Y. Wu, Z. Zhang, Z. Zhai, R. Yang, Mater. Sci. Eng. A 939 (2025).
- [233] L. Zhou, H. Deng, W. Qiu, W. Liu, H. Zuo, H. Chen, P. Xu, J. Tang, Mater. Sci. Eng. A 877 (2023) 145194.
- [234] H. Ding, L. Wang, X. Lin, A. Xue, L. Yuan, M. Dang, W. Huang, Mater. Sci. Eng. A 855 (2022) 143907.
- [235] E. Zhao, S. Sun, Y. Zhang, J. Mater. Res. Technol. 14 (2021) 3029–3042.
- [236] R.A. Michi, A. Plotkowski, A. Shyam, R.R. Dehoff, S.S. Babu, Int. Mater. Rev. 67 (2022) 298–345.
- [237] M. Rizwan, J. Lu, F. Chen, R. Chai, R. Ullah, Y. Zhang, Z. Zhang, Acta Metall. Sin. (Engl. Lett.) 34 (2021) 1201–1212.
- [238] M. Rizwan, J. Lu, R. Ullah, Y. Zhang, Z. Zhang, Mater. Sci. Eng. A 857 (2022) 144062.
- [239] Z.C. Sun, J. Zhang, H. Yang, H.L. Wu, J. Mater. Process. Technol. 222 (2015) 234–243.
- [240] J. Song, Y. Han, M. Fang, F. Hu, L. Ke, Y. Li, L. Lei, W. Lu, Mater. Charact. 165 (2020) 110342.
- [241] D. June, J.R. Mayeur, P. Grndl, A. Wessman, K. Hazeli, Addit. Manuf. 80 (2024) 103970.
- [242] J.R. Zhao, F.Y. Hung, T.S. Lui, Y.L. Wu, Metals 9 (2019).
- [243] S. Ivanov, M. Gushchina, A. Artinov, M. Khomutov, E. Zemlyakov, Materials 14 (2021).
- [244] A. Gupta, C.J. Bennett, W. Sun, Eng. Fail. Anal. 120 (2021) 105115.
- [245] S. Wang, J. Yang, J. Sun, W. Shu, H. Yang, A.H.W. Ngan, Y. Huang, Mater. Sci. Eng. A 888 (2023) 145806.
- [246] J. Sun, H. Lu, H. Zhang, K. Luo, J. Lu, Mater. Sci. Eng. A 908 (2024) 146757.
- [247] G. Zhang, W. Liu, P. Zhang, H. Xiong, J. Gao, H. Yu, H. Yuan, Materials 15 (2022).
- [248] Z. Zhu, C. Wang, X. Hang, T. Liu, C. Dong, Mater. Sci. Eng. A 883 (2023) 145519.
- [249] A. Zhang, D. Liu, X. Wu, H. Wang, J. Alloy. Compd. 585 (2014) 220–228.
- [250] Z. Zhu, T. Liu, C. Dong, D. Dong, S. Zhang, Q. Wang, J. Mater. Res. Technol. 18 (2022) 2582–2592.
- [251] R. Casati, G. Boari, A. Rizzi, M. Vedani, Eur. J. Mater. 1 (2022) 72–83.
- [252] Z. Zhu, P. Kumar, F.L. Ng, H.L. Seet, U. Ramamurty, S.M.L. Nai, J. Alloy. Compd. 925 (2022) 166656.
- [253] J. Yu, K. Su, X. Lin, H. Tan, Q. Yan, Y. Tang, W. Huang, Mater. Sci. Eng. A 850 (2022) 143526.
- [254] R. Boyer, G. Welsch, E.W. Collings, Materials properties handbook: titanium alloys, ASM International, 1994.
- [255] Q.J. Sun, X. Xie, Mater. Sci. Eng. A 724 (2018) 493–501.
- [256] W. Chen, C.J. Boehlert, Metall. Mater. Trans. A Phys. Metall. Mater. Sci. 40 (2009) 1568–1578.
- [257] M.J. Donachie, Titanium a technical guide, ASM International, 1988.
- [258] K. Prasad, V.K. Varma, Mater. Sci. Eng. A 486 (2008) 158–166.
- [259] V.K. Chandravanshi, A. Bhattacharjee, S.V. Kamat, T.K. Nandy, J. Alloy. Compd. 589 (2014) 336–345.
- [260] X. Liu, H. Li, M. Zhan, R. Zhang, Trans. Nonferrous Met. Soc. China (Engl. Ed. 32 (2022) 162–174.
- [261] Z. Sun, Y. Ma, D. Ponge, S. Zaefferer, E.A. Jägle, B. Gault, A.D. Rollett, D. Raabe, Nat. Commun. 13 (2022) 1–12.
- [262] G. Li, W. Chi, W. Wang, X. Liu, H. Tu, X. Long, Int. J. Fatigue 184 (2024) 108287.
- [263] H. Li, Z. Tian, J. Zheng, K. Huang, B. Nie, W. Xu, Z. Zhao, Int. J. Fatigue 167 (2023).
- [264] H. Peng, F. Liu, Y. Chen, C. He, L. Li, H. Zhang, C. Wang, Q. Wang, Y. Liu, Int. J. Fatigue 171 (2023) 107599.
- [265] H.J. Maier, Mater. High. Temp. 15 (1998) 3–14.
- [266] K. Tokaji, Scr. Mater. 54 (2006) 2143–2148.
- [267] F. An, L. Zhang, C.H.T. Lee, Mater. Sci. Eng. A 912 (2024) 146988.
- [268] S. Zhao, R. Zhang, Q. Yu, J. Ell, R.O. Ritchie, A.M. Minor, Science 373 (2021) 1363–1368.
- [269] Y. Xiao, G. Qian, J. Sun, F. Berto, J.A.F. Correia, Y. Hong, Theor. Appl. Fract. Mech. 125 (2023) 103931.
- [270] G. Singh, G. Bajargan, R. Datta, U. Ramamurty, Mater. Sci. Eng. A 611 (2014) 45–57.
- [271] Q. Wang, X. Liu, Y. Ren, M. Song, I. Baker, H. Wu, J. Alloy. Compd. 1001 (2024) 175075.
- [272] H.Z. Niu, S. Liu, M.C. Zang, D.L. Zhang, P. Cao, W.X. Yang, J. Mater. Sci. Technol. 198 (2024) 44–55.
- [273] G. Singh, G. Singh, G. Singh, J. Radhakrishnan, P. Kumar, N. Nayak, U. Ramamurty, B. Gludovatz, K.S. Ravichandran, P. Peralta, Materialia 39 (2025) 102307.
- [274] H. Yang, H. Li, H. Sun, Y.H. Zhang, X. Liu, M. Zhan, Y.L. Liu, M.W. Fu, Int. J. Plast. 156 (2022).
- [275] R. Soltysiak, J. Malecka, Mater. Sci. Eng. A 734 (2018) 476–484.
- [276] A. Azarniya, X.G. Colera, M.J. Mirzaali, S. Sovizi, F. Bartolomeu, M. k St Jeglowksi, W.W. Wits, C.Y. Yap, J. Ahn, G. Miranda, F.S. Silva, H.R. Madaah Hosseini, S. Ramakrishna, A.A. Zadpoor, J. Alloy. Compd. 804 (2019) 163–191.
- [277] J. Günther, D. Krewerth, T. Lippmann, S. Leuders, T. Tröster, A. Weidner, H. Biermann, T. Niendorf, Int. J. Fatigue 94 (2017) 236–245.
- [278] J.V. Gordon, S.P. Narra, R.W. Cunningham, H. Liu, H. Chen, R.M. Suter, J. L. Beuth, A.D. Rollett, Addit. Manuf. 36 (2020) 101552.
- [279] Z. Chen, X. Wu, C.H.J. Davies, Addit. Manuf. 41 (2021) 101987.
- [280] J. Zelin, Cmaj 190 (2018) E1393.
- [281] L. Thijis, F. Verhaeghe, T. Craeghs, J. Van Humbeeck, J.P. Kruth, Acta Mater. 58 (2010) 3303–3312.
- [282] A.M. Vilardell, I. Yadroitsava, M. Albu, N. Takata, M. Kobashi, P. Krakhmalev, D. Kouprianoff, G. Kotheleitner, A. du Plessis, Addit. Manuf. 36 (2020).
- [283] Q.C. Liu, J. Elambasseril, S.J. Sun, M. Leary, M. Brandt, P.K. Sharp, Adv. Mater. Res. 891–892 (2014) 1519–1524.
- [284] J.H. Rao, Y. Zhang, A. Huang, X. Wu, K. Zhang, Int. J. Fatigue 129 (2019) 105215.
- [285] Q. Guo, C. Zhao, L.I. Escano, Z. Young, L. Xiong, K. Fezzaa, W. Everhart, B. Brown, T. Sun, L. Chen, Acta Mater. 151 (2018) 169–180.
- [286] E.O. Olakanmi, R.F. Cochrane, K.W. Dalgarino, Prog. Mater. Sci. 74 (2015) 401–477.
- [287] M. Tang, P.C. Pistorius, J.L. Beuth, Addit. Manuf. 14 (2017) 39–48.

- [288] T. Mukherjee, J.S. Zuback, A. De, T. DebRoy, *Sci. Rep.* 6 (2016) 1–8.
- [289] C. Zhao, N.D. Parab, X. Li, K. Fezzaa, W. Tan, A.D. Rollett, T. Sun, *Science* (80.) 370 (2020) 1080–1086.
- [290] R. Fabbro, K. Chouf, *J. Appl. Phys.* 87 (2000) 4075–4083.
- [291] Y. Chen, S.J. Clark, C.L.A. Leung, L. Sinclair, S. Marussi, M.P. Olbinado, E. Boller, A. Rack, I. Todd, P.D. Lee, *Appl. Mater. Today* 20 (2020) 100650.
- [292] W. Ge, J.Y.H. Fu, S.J. Na, *J. Manuf. Process* 62 (2021) 646–654.
- [293] J. Yang, J. Han, H. Yu, J. Yin, M. Gao, Z. Wang, X. Zeng, *Mater. Des.* 110 (2016) 558–570.
- [294] G. Chen, S.Y. Zhao, P. Tan, J. Wang, C.S. Xiang, H.P. Tang, *Powder Technol.* 333 (2018) 38–46.
- [295] M.J. Kenney, K. O'Donnell, M.J. Quintana, P.C. Collins, *Scr. Mater.* 198 (2021) 113827.
- [296] S. Tammas-Williams, P.J. Withers, I. Todd, P.B. Prangnell, *Scr. Mater.* 122 (2016) 72–76.
- [297] ASTM F3301, ASTM Stand (2018) 3.
- [298] S. Tammas-Williams, P.J. Withers, I. Todd, P.B. Prangnell, *Metall. Mater. Trans. A Phys. Metall. Mater. Sci.* 47 (2016) 1939–1946.
- [299] M.W. Wu, P.H. Lai, *Mater. Sci. Eng. A* 658 (2016) 429–438.
- [300] C.Y. Yap, C.K. Chua, Z.L. Dong, Z.H. Liu, D.Q. Zhang, L.E. Loh, S.L. Sing, *Appl. Phys. Rev.* 2 (2015) 041101.
- [301] D. Gu, Y.C. Hagedorn, W. Meiners, G. Meng, R.J.S. Batista, K. Wissenbach, R. Poprawe, *Acta Mater.* 60 (2012) 3849–3860.
- [302] D. Greitemeier, C. Dalle Donne, F. Syassen, J. Euflinger, T. Melz, *Mater. Sci. Technol.* (U. Kingd.) 32 (2016) 629–634.
- [303] H. Gong, K. Rafi, H. Gu, T. Starr, B. Stucker, *Addit. Manuf.* 1 (2014) 87–98.
- [304] H. Amano, Y. Yamaguchi, T. Ishimoto, T. Nakano, *Mater. Trans.* 62 (2021) 1225–1230.
- [305] H. Amano, T. Ishimoto, T. Nakano, *Mater. Trans.* 64 (2023) 2–9.
- [306] Z. Wang, C. Guo, S. Shi, Z. Chen, G. Jiang, C. Liu, D. Xu, F. Jiang, *Opt. Laser Technol.* 181 (2025).
- [307] D. Sommer, S. Hornung, C. Esen, R. Hellmann, J. Manuf. Mater. Process 9 (2025) 1–14.
- [308] P. Wüst, A. Edelmann, R. Hellmann, *Materials* 13 (2020).
- [309] P.A. Colegrave, J. Donoghue, F. Martina, J. Gu, P. Prangnell, J. Hönnige, *Scr. Mater.* 135 (2017) 111–118.
- [310] J. Pegues, M. Roach, R. Scott Williamson, N. Shamsaei, *Int. J. Fatigue* 116 (2018) 543–552.
- [311] M. Danish, M.K. Gupta, S.M. Ghazali, M.F. Rathore, G.M. Krolczyk, A. Alsaady, *J. Mater. Res. Technol.* 30 (2024) 2955–2967.
- [312] J. Zhou, Y. Song, *Int. J. Adv. Manuf. Technol.* 138 (2025) 4675–4688.
- [313] X.Y. Tan, Y. Ng, T.L. Meng, C.N. Sun, Z. Huang, A.C.Y. Ngo, H. Liu, *Surf. Coat. Technol.* 494 (2024).
- [314] J. Wang, L. Zhang, J. Cheng, J. Liu, Y. Zou, D. Wei, S. Cheng, Y. Wang, *J. Manuf. Process* 133 (2025) 979–991.
- [315] S. Han, F. Salvatore, J. Rech, J. Bajolet, J. Courbon, *Procedia CIRP* 87 (2020) 315–320.
- [316] Y. Liu, X. Liu, J. Lu, Z. Zhang, K. Luo, S. Huang, H. Lu, G. Xu, G. Dai, S. Zhou, *Virtual Phys. Prototyp.* 20 (2025) 1–27.
- [317] J.L. Bartlett, X. Li, *Addit. Manuf.* 27 (2019) 131–149.
- [318] C.H. Ng, M.J. Bermingham, D. Kent, M.S. Dargusch, *Mater. Sci. Eng. A* 816 (2021).
- [319] M.M. Kirk, P. Nandwana, Y. Lee, R.R. Dehoff, *Scr. Mater.* 135 (2017) 130–134.
- [320] W. Xu, M. Brandt, S. Sun, J. Elambasseri, Q. Liu, K. Latham, K. Xia, M. Qian, *Acta Mater.* 85 (2015) 74–84.
- [321] T. Mukherjee, T. DebRoy, T.J. Lienert, S.A. Maloy, P. Hosemann, *Acta Mater.* 209 (2021) 116775.
- [322] C.H. Ng, M.J. Bermingham, L. Yuan, M.S. Dargusch, *Acta Mater.* 224 (2022).
- [323] C.H. Ng, M.J. Bermingham, M.S. Dargusch, *Addit. Manuf.* 39 (2021).
- [324] D. Chen, R. Das, S. Lu, M. Qian, D. Qiu, *J. Mater. Res. Technol.* 29 (2024) 839–850.
- [325] W.D. Zeng, Y.G. Zhou, *Mater. Sci. Eng. A* 260 (1999) 203–211.
- [326] M.J. Bermingham, S.D. McDonald, M.S. Dargusch, D.H. St. John, *J. Mater. Res.* 23 (2008) 97–104.
- [327] W. Zeng, Y. Zhang, H. Yan, *J. Mater. Eng. Perform.* 9 (2000) 222–227.
- [328] C.H. Ng, M. Bermingham, P. Collins, M. Dargusch, *Adv. Eng. Mater.* 26 (2024) 1–7.
- [329] H. Hayakawa, N. Fukada, T. Udagawa, M. Koizumi, H.G. Suzuki, T. Fukuyama, *ISIJ Int* 31 (1991) 775–784.
- [330] A. Mitchell, A. Kawakami, S.L. Cockcroft, *High. Temp. Mater. Process* 26 (2007) 59–77.
- [331] H. Azizi, H. Zurob, B. Bose, S. Reza Ghiasi, X. Wang, S. Coulson, V. Duz, A. B. Phillion, *Addit. Manuf.* 21 (2018) 529–535.
- [332] A. Mitchell, *Mater. Sci. Eng. A* 243 (1998) 257–262.
- [333] Y. Liu, L. Xu, C. Qiu, *Addit. Manuf.* 60 (2022) 103208.
- [334] D. Sharma, S.R. Kada, D. Fabijanic, D. Parfitt, B. Chen, B. Roebuck, M. E. Fitzpatrick, M.R. Barnett, *Addit. Manuf.* 48 (2021) 102384.
- [335] P. Mercelis, J.P. Kruth, *Rapid Prototyp. J.* 12 (2006) 254–265.
- [336] C. Guo, G. Li, S. Li, X. Hu, H. Lu, X. Li, Z. Xu, Y. Chen, Q. Li, J. Lu, Q. Zhu, *Nano Mater. Sci.* 5 (2023) 53–77.
- [337] S. Mereddy, M.J. Bermingham, D.H. StJohn, M.S. Dargusch, *J. Alloy. Compd.* 695 (2017) 2097–2103.
- [338] C. Qiu, Q. Liu, *Addit. Manuf.* 30 (2019) 100893.
- [339] M.J. Bermingham, D. Kent, H. Zhan, D.H. StJohn, M.S. Dargusch, *Acta Mater.* 91 (2015) 289–303.
- [340] C. Chen, S. Chang, J. Zhu, Z. Xiao, H. Zhu, X. Zeng, *J. Manuf. Process* 59 (2020) 621–628.
- [341] L. Sun, X. Ren, J. He, Z. Zhang, *J. Mater. Sci. Technol.* 67 (2021) 11–22.
- [342] C.J. Todaro, M.A. Easton, D. Qiu, D. Zhang, M.J. Bermingham, E.W. Lui, M. Brandt, D.H. StJohn, M. Qian, *Nat. Commun.* 11 (2020) 1–9.
- [343] I. Yadroitsev, I. Yadroitseva, *Virtual Phys. Prototyp.* 10 (2015) 67–76.
- [344] L. Parry, I.A. Ashcroft, R.D. Wildman, *Addit. Manuf.* 12 (2016) 1–15.
- [345] Z. Xiao, C. Chen, H. Zhu, Z. Hu, B. Nagarajan, L. Guo, X. Zeng, *Mater. Des.* 193 (2020) 108846.
- [346] Z.C. Fang, Z.L. Wu, C.G. Huang, C.W. Wu, *Opt. Laser Technol.* 129 (2020) 106283.
- [347] T. Mukherjee, V. Manvatkar, A. De, T. DebRoy, *Scr. Mater.* 127 (2017) 79–83.
- [348] N.C. Levkulich, S.L. Semiatin, J.E. Gockel, J.R. Middendorf, A.T. DeWald, N. W. Klingbeil, *Addit. Manuf.* 28 (2019) 475–484.
- [349] J. Karimi, M. Antonov, L. Kollo, K.G. Prashanth, *J. Alloy. Compd.* 897 (2022) 163207.
- [350] M. Yan, W. Xu, M.S. Dargusch, H.P. Tang, M. Brandt, M. Qian, *Powder Met.* 57 (2014) 251–257.
- [351] F. Bosio, H. Shen, Y. Liu, M. Lombardi, P. Rometsch, X. Wu, Y. Zhu, A. Huang, *Jom* 73 (2021) 770–780.
- [352] X. Chen, X. Xie, H. Wu, X. Ji, H. Shen, M. Xue, H. Wu, Q. Chao, G. Fan, Q. Liu, *Mater. Charact.* 201 (2023) 23–25.
- [353] C. Tan, D. Wang, W. Ma, Y. Chen, S. Chen, Y. Yang, K. Zhou, *Mater. Des.* 196 (2020) 109147.
- [354] T. Kraenzler, R. Rettinger, *Sulzer Tech. Rev.* 100 (2020) 1–13.
- [355] C.K. Sit, L.N.S. Chiu, Y. Tang, A. Huang, *Virtual Phys. Prototyp.* 18 (2023).
- [356] T. Mishurova, K. Artzt, B. Rehmer, J. Haubrich, L. Ávila, F. Schoenstein, I. Serrano-Munoz, G. Requena, G. Bruno, *Int. J. Fatigue* 148 (2021).
- [357] T. Mishurova, S. Cabeza, K. Artzt, J. Haubrich, M. Klaus, C. Genzel, G. Requena, G. Bruno, *Materials* 10 (2017).
- [358] C. Liu, Y. Lu, X. Tian, D. Liu, *Mater. Sci. Eng. A* 661 (2016) 145–151.
- [359] M. Benedetti, C. Santus, *Int. J. Fatigue* 121 (2019) 281–292.
- [360] Y.J. Liu, H.L. Wang, S.J. Li, S.G. Wang, W.J. Wang, W.T. Hou, Y.L. Hao, R. Yang, L.C. Zhang, *Acta Mater.* 126 (2017) 58–66.
- [361] J. Elambasseri, S.L. Lu, Y.P. Ning, N. Liu, J. Wang, M. Brandt, H.P. Tang, M. Qian, *Mater. Sci. Eng. A* 761 (2019).
- [362] A. du Plessis, I. Yadroitseva, S.G. le Roux, I. Yadroitsev, J. Fieres, C. Reinhart, P. Rossouw, *J. Alloy. Compd.* 724 (2017) 267–274.
- [363] A. du Plessis, I. Yadroitseva, I. Yadroitsev, *Mater. Des.* 187 (2020) 108385.
- [364] C. Pei, D. Shi, H. Yuan, H. Li, *Mater. Sci. Eng. A* 759 (2019) 278–287.
- [365] C. Qiu, N.J.E. Adkins, M.M. Attallah, *Acta Mater.* 103 (2016) 382–395.
- [366] P. Edwards, M. Ramulu, *Mater. Sci. Eng. A* 598 (2014) 327–337.
- [367] Y.N. Hu, S.C. Wu, P.J. Withers, J. Zhang, H.Y.X. Bao, Y.N. Fu, G.Z. Kang, *Mater. Des.* (2020) 192.
- [368] Y.N. Hu, S.C. Wu, Z.K. Wu, X.L. Zhong, S. Ahmed, S. Karabal, X.H. Xiao, H. O. Zhang, P.J. Withers, *Int. J. Fatigue* 136 (2020).
- [369] S. Tammas-Williams, P.J. Withers, I. Todd, P.B. Prangnell, *Sci. Rep.* 7 (2017) 1–13.
- [370] Y. Yamashita, T. Murakami, R. Miura, M. Okada, Y. Murakami, *Int. J. Fatigue* 117 (2018) 485–495.
- [371] Y. Murakami, *Metal Fatigue: Effects of Small Defects and Nonmetallic Inclusions*, Elsevier Science, 2019.
- [372] F. Liu, C. He, Y. Chen, H. Zhang, Q. Wang, Y. Liu, *Int. J. Fatigue* 140 (2020) 105795.
- [373] Z. Qu, Z.J. Zhang, Y.K. Zhu, R. Liu, S.L. Lu, S.J. Li, Q.Q. Duan, B.N. Zhang, M. X. Zhao, J. Eckert, Z.F. Zhang, *Addit. Manuf.* 61 (2023).
- [374] E. Moquin, M. Letenneur, A. Kreitzberg, J.R. Poulin-Masson, V. Brailovski, *Mater. Sci. Eng. A* 884 (2023) 145509.
- [375] H. Zhang, D. Dong, S. Su, A. Chen, Chin. J. Aeronaut. 32 (2019) 2383–2393.
- [376] B. Vayssette, N. Saintier, C. Brugger, M. Elmay, E. Pessard, *Procedia Eng.* 213 (2018) 89–97.
- [377] J. Rogers, J. Elambasseri, C. Wallbrink, B. Krieg, M. Qian, M. Brandt, M. Leary, *Addit. Manuf.* 85 (2024) 104149.
- [378] L. Ednie, R.J. Lancaster, A.A. Antonsamy, F. Zelenka, A. Scarpellini, L. Parimi, R. Maddalena, N.C. Barnard, P. Efthymiadis, *Mater. Sci. Eng. A* 857 (2022) 144050.
- [379] S. Aguado-Montero, C. Navarro, J. Vázquez, F. Lasagni, S. Slawik, J. Domínguez, *Int. J. Fatigue* 154 (2022).
- [380] R. Xin, L. Lan, C. Bai, S. Gao, B. He, J. Wang, *J. Mater. Sci.* 57 (2022) 9619–9630.
- [381] E. Atzeni, S. Genna, E. Menna, G. Rubino, A. Salmi, F. Trovalusci, *Materials* 14 (2021) 1–14.
- [382] J. Zhang, M. Bermingham, J. Otte, Y. Liu, M. Dargusch, *Scr. Mater.* 223 (2023).
- [383] R.R.B.C. Chen, *Jom* (1979) 33–39.
- [384] C.H. Ng, M.J. Bermingham, M.S. Dargusch, *Addit. Manuf.* 39 (2021).
- [385] B. Vrancken, R. Wauthle, J.P. Kruth, J. Van Humbeeck, 24th Int. SFF Symp. Addit. Manuf. Conf. SFF 2013 (2013) 393–407.
- [386] P.J. Withers, *Rep. Prog. Phys.* 70 (2007) 2211–2264.
- [387] F.R. Kaschel, R.K. Vijayaraghavan, A. Shmeliov, E.K. McCarthy, M. Canavan, P. J. McNally, D.P. Dowling, V. Nicolosi, M. Celikin, *Acta Mater.* 188 (2020) 720–732.
- [388] M.J. Bermingham, D.H. StJohn, J. Krynen, S. Tedman-Jones, M.S. Dargusch, *Acta Mater.* 168 (2019) 261–274.
- [389] J. Donoghue, A.E. Davis, C.S. Daniel, A. Garner, F. Martina, J. Quinta da Fonseca, P.B. Prangnell, *Acta Mater.* 186 (2020) 229–241.

- [390] A.R. McAndrew, M. Alvarez Rosales, P.A. Colegrove, J.R. Hönnige, A. Ho, R. Fayolle, K. Eiyitayo, I. Stan, P. Sukrungpang, A. Crochemore, Z. Pinter, *Addit. Manuf.* 21 (2018) 340–349.
- [391] J. Hu, J. Zhang, Y. Wei, H. Chen, Y. Yang, S. Wu, D. Kovalchuk, E. Liang, X. Zhang, H. Wang, A. Huang, *Jom* 73 (2021) 2241–2249.
- [392] G.A. Ravi, C. Qiu, M.M. Attallah, *Mater. Lett.* 179 (2016) 104–108.
- [393] N. Sridharan, A. Chaudhary, P. Nandwana, S.S. Babu, *Jom* 68 (2016) 772–777.
- [394] J. Lu, L. Chang, J. Wang, L. Sang, S. Wu, Y. Zhang, *Mater. Sci. Eng. A* 712 (2018) 199–205.
- [395] W. Xu, E.W. Lui, A. Pateras, M. Qian, M. Brandt, *Acta Mater.* 125 (2017) 390–400.
- [396] J. Yang, H. Yu, J. Yin, M. Gao, Z. Wang, X. Zeng, *Mater. Des.* 108 (2016) 308–318.
- [397] M.N. Ahsan, A.J. Pinkerton, R.J. Moat, J. Shackleton, *Mater. Sci. Eng. A* 528 (2011) 7648–7657.
- [398] C. Qian, K. Zhang, J. Zhu, Y. Liu, Y. Liu, J. Liu, J. Liu, Y. Yang, H. Wang, *AIP Adv.* 14 (2024).
- [399] J. Liu, K. Zhang, X. Gao, H. Wang, S. Wu, Y. Yang, Y. Zhu, A. Huang, *Mater. Des.* 223 (2022) 111150.
- [400] S.S. Al-Bermani, M.L. Blackmore, W. Zhang, I. Todd, *Metall. Mater. Trans. A Phys. Metall. Mater. Sci.* 41 (2010) 3422–3434.
- [401] S.M.J. Razavi, B. Van Hooreweder, F. Berto, *Addit. Manuf.* 36 (2020) 101426.
- [402] H. Wang, Q. Chao, H.S. Chen, Z.B. Chen, S. Primig, W. Xu, S.P. Ringer, X.Z. Liao, *Acta Mater.* 235 (2022).
- [403] S. Cao, Q. Hu, A. Huang, Z. Chen, M. Sun, J. Zhang, C. Fu, Q. Jia, C.V.S. Lim, R. Boyer, Y. Yang, X. Wu, J. *Mater. Sci. Technol.* 35 (2019) 1578–1586.
- [404] J. Xu, W. Zeng, X. Zhang, D. Zhou, J. *Alloy. Compd.* 788 (2019) 110–117.
- [405] J. Chen, D. Fabijanic, M. Brandt, Y. Zhao, S.B. Ren, W. Xu, *Acta Mater.* 255 (2023).
- [406] N. Stefansson, S.L. Semiatin, D. Eylon, *Metall. Mater. Trans. A Phys. Metall. Mater. Sci.* 33 (2002) 3527–3534.
- [407] S. Tanii, O. Umezawa, Y. Yamabe-Mitarai, *J. Alloy. Compd.* 854 (2021) 157184.
- [408] M.J. Birmingham, L. Nicastro, D. Kent, Y. Chen, M.S. Dargusch, *J. Alloy. Compd.* 753 (2018) 247–255.
- [409] S. Zherebtsov, M. Murzinova, G. Salishchev, S.L. Semiatin, *Acta Mater.* 59 (2011) 4138–4150.
- [410] J. Xu, W. Zeng, H. Ma, D. Zhou, J. *Alloy. Compd.* 736 (2018) 99–107.
- [411] Z. Zhao, J. Chen, H. Tan, G. Zhang, X. Lin, W. Huang, *Scr. Mater.* 146 (2018) 187–191.
- [412] R. Sabban, S. Bahl, K. Chatterjee, S. Suwas, *Acta Mater.* 162 (2019) 239–254.
- [413] Z. Sun, S. Guo, H. Yang, *Acta Mater.* 61 (2013) 2057–2064.
- [414] M. Salib, J. Teixeira, L. Germain, E. Lamielle, N. Gey, E. Aeby-Gautier, *Acta Mater.* 61 (2013) 3758–3768.
- [415] T. Furuhara, S. Takagi, H. Watanabe, T. Maki, *Metall. Mater. Trans. A* 27 (1996) 1635–1646.
- [416] J. Liu, K. Zhang, Y. Yang, H. Wang, Y. Zhu, A. Huang, *Scr. Mater.* 207 (2022) 114261.
- [417] Z. Zhao, J. Chen, X. Lu, H. Tan, X. Lin, W. Huang, *Mater. Sci. Eng. A* 691 (2017) 16–24.
- [418] Y. Xie, M. Gong, R. Zhang, M. Gao, X. Zeng, F. Wang, *J. Alloy. Compd.* 869 (2021) 159287.
- [419] Z. Zou, M. Simonelli, J. Katrib, G. Dimitrakis, R. Hague, *Mater. Sci. Eng. A* 814 (2021) 141271.
- [420] C.H. Ng, M.J. Birmingham, D. Kent, M.S. Dargusch, *Mater. Sci. Eng. A* 816 (2021) 141326.
- [421] C. Madikizela, L.A. Cornish, L.H. Chown, H. Möller, *Mater. Sci. Eng. A* 747 (2019) 225–231.
- [422] T. Nagase, T. Hori, M. Todai, S.H. Sun, T. Nakano, *Mater. Des.* 173 (2019) 107771.
- [423] Y.J. Liu, Y.S. Zhang, L.C. Zhang, *Materialia* 6 (2019) 100299.
- [424] J. Liu, J. Liu, Y. Li, R. Zhang, Z. Zeng, Y. Zhu, K. Zhang, A. Huang, *Metals* 11 (2021) 1593.
- [425] C.M. Liu, H.M. Wang, X.J. Tian, H.B. Tang, D. Liu, *Mater. Sci. Eng. A* 586 (2013) 323–329.
- [426] J.A. Ballor, T. Li, F. Prima, C.J. Boehlert, A. Devaraj, *Int. Mater. Rev.* 68 (2023) 26–45.
- [427] S. Nag, R. Banerjee, R. Srinivasan, J.Y. Hwang, M. Harper, H.L. Fraser, *Acta Mater.* 57 (2009) 2136–2147.
- [428] D.A. Porter, K.E. Easterling, K.E. Easterling, *Phase Transform. Met. Alloy.* (2009).
- [429] M.J. Birmingham, D. Kent, B. Pace, J.M. Cairney, M.S. Dargusch, *Mater. Sci. Eng. A* 791 (2020) 139646.
- [430] Y. Liu, S.C.V. Lim, C. Ding, A. Huang, M. Weyland, *J. Mater. Sci. Technol.* 97 (2022) 101–112.
- [431] A. Zafari, E.W.C. Lui, M. Li, K. Xia, J. *Mater. Sci. Technol.* 105 (2022) 131–141.
- [432] Z. Liu, Z.B. Zhao, J. Liu, Q. Wang, Z. Guo, J. Wang, G. Yang, S. Gong, *Mater. Sci. Eng. A* 798 (2020) 140093.
- [433] G.M. Ter Haar, T.H. Becker, *Mater. Sci. Eng. A* 814 (2021) 141185.
- [434] C. de Formanoir, S. Michotte, O. Rigo, L. Germain, S. Godet, *Mater. Sci. Eng. A* 652 (2016) 105–119.
- [435] A.A. Antonysamy, J. Meyer, P.B. Prangnell, *Mater. Charact.* 84 (2013) 153–168.
- [436] M. Simonelli, Y.Y. Tse, C. Tuck, *Metall. Mater. Trans. A Phys. Metall. Mater. Sci.* 45 (2014) 2863–2872.
- [437] A.E. Davis, J.R. Kennedy, J. Ding, P.B. Prangnell, *Mater. Charact.* 163 (2020) 110298.
- [438] J. Liu, G. Li, Q. Sun, H. Li, J. Sun, X. Wang, *J. Mater. Process. Technol.* 299 (2022).
- [439] A.J. Saville, S.C. Vogel, A. Creuziger, J.T. Benzing, A.L. Pilchak, P. Nandwana, J. Klemm-Toole, K.D. Clarke, S.L. Semiatin, A.J. Clarke, *Addit. Manuf.* 46 (2021) 102118.
- [440] Y.M. Ren, X. Lin, X. Fu, H. Tan, J. Chen, W.D. Huang, *Acta Mater.* 132 (2017) 82–95.
- [441] A.E. Wilson-Heid, Z. Wang, B. McCornac, A.M. Beese, *Mater. Sci. Eng. A* 706 (2017) 287–294.
- [442] B. Vrancken, L. Thijss, J.P. Kruth, J. Van Humbeeck, *J. Alloy. Compd.* 541 (2012) 177–185.
- [443] P. Barriobero-Vila, J. Gussone, A. Stark, N. Schell, J. Haubrich, G. Requena, *Nat. Commun.* 9 (2018) 1–9.
- [444] Y. Mine, Y. Matsuzaki, K. Takashima, *Scr. Mater.* 177 (2020) 223–228.
- [445] Z. Liu, Z.B. Zhao, J. Liu, Q. Wang, Z. Guo, Y. Zeng, G. Yang, S. Gong, *J. Alloy. Compd.* 850 (2021) 156886.
- [446] X. Pang, Z. Xiong, C. Yao, J. Sun, R.D.K. Misra, Z. Li, *Mater. Sci. Eng. A* 831 (2022) 142265.
- [447] S.A. Mantri, D. Choudhuri, T. Alam, G.B. Viswanathan, J.M. Sosa, H.L. Fraser, R. Banerjee, *Scr. Mater.* 154 (2018) 139–144.
- [448] M.J. Birmingham, S.D. McDonald, M.S. Dargusch, *Mater. Sci. Eng. A* 719 (2018) 1–11.
- [449] G. Lütjering, J. Albrecht, C. Sauer, T. Krull, *Mater. Sci. Eng. A* 468–470 (2007) 201–209.
- [450] K. Narita, M. Niinomi, M. Nakai, Suyalatu, *Mater. Sci. Eng. A* 643 (2015) 109–118.
- [451] J. Sun, X. Li, J. Zhang, G. Wang, M. Yang, H. Wang, D. Xu, Jinshu Xuebao/*Acta Metall. Sin.* 56 (2020) 1113–1122.
- [452] H. Peng, W. Ye, J. Liu, S. Wu, Y. Zhang, Y. Zhang, *J. Mater. Res. Technol.* 36 (2025) 8860–8864.
- [453] S. Han, M.A. Crimp, *Int. J. Plast.* 131 (2020) 102731.
- [454] B.J. Hayes, B.W. Martin, B. Welk, S.J. Kuhr, T.K. Ales, D.A. Brice, I. Ghamarian, A. H. Baker, C.V. Haden, D.G. Harlow, H.L. Fraser, P.C. Collins, *Acta Mater.* 133 (2017) 120–133.
- [455] M.R. Bache, W.J. Evans, *Mater. Sci. Eng. A* 319–321 (2001) 409–414.
- [456] K. Zhang, K.V. Yang, A. Huang, X. Wu, C.H.J. Davies, *Int. J. Fatigue* 80 (2015) 288–297.
- [457] K. Zhang, X. Wu, C.H.J. Davies, *Int. J. Fatigue* 104 (2017) 206–220.
- [458] K. Zhang, K.V. Yang, S. Lim, X. Wu, C.H.J. Davies, *Int. J. Fatigue* 104 (2017) 1–11.
- [459] T. Song, Z. Chen, X. Cui, S. Lu, H. Chen, H. Wang, T. Dong, B. Qin, K.C. Chan, M. Brandt, *Nature* 618 (2023).
- [460] Y. Dong, D. Wang, Q. Li, X. Luo, J. Zhang, K.G. Prashanth, P. Wang, J. Eckert, L. Mädler, I.V. Okulov, M. Yan, *Mater. Today Adv.* 17 (2023) 0–11.
- [461] Z. Xu, A. Liu, X. Wang, B. Liu, M. Guo, *Int. J. Fatigue* 143 (2021) 106008.
- [462] P. Kumar, U. Ramamurthy, *Acta Mater.* 194 (2020) 305–320.
- [463] M. Awd, L. Saeed, F. Walther, *Materials* 18 (2025) 1–31.
- [464] Z. Qi, B. Wang, P. Zhang, R. Liu, Z. Zhang, Z. Zhang, *Fatigue Fract. Eng. Mater. Struct.* 45 (2022) 2457–2467.
- [465] S. Krishnamoorthy, R. Bandyopadhyay, M.D. Sangid, *Int. J. Plast.* 163 (2023) 103569.
- [466] J. Schijve, *Eng. Fract. Mech.* 11 (1979) 169–181.
- [467] M. Peters, A. Gysler, G. Lütjering, *Metall. Trans. A* 15 (1984) 1597–1605.
- [468] M.R. Bache, W.J. Evans, B. Sudell, F.R.M. Herrouin, *Int. J. Fatigue* 23 (2001) 153–159.
- [469] K. Zhang, Y. Liu, X. Tian, Y. Yang, Y. Zhu, M. Birmingham, A. Huang, *Int. J. Fatigue* 168 (2022) 107454.
- [470] G.M. Ter Haar, T.H. Becker, *J. Alloy. Compd.* 918 (2022) 165497.
- [471] G. Wang, M. Zhang, Y. Fu, H. Zhang, W. Zhai, Y. Lu, R. Li, *Mater. Sci. Eng. A* 909 (2009) 146850.
- [472] D. Zhang, D. Shi, F. Wang, D. Qian, Y. Zhou, J. Fu, M. Chen, D. Qiu, S. Jiang, *J. Alloy. Compd.* 966 (2023) 171536.
- [473] J. Liu, K. Zhang, J. Liu, H. Wang, Y. Yang, L. Yan, *Int. J. Fatigue* 176 (2023) 107839.
- [474] Y. Xie, M. Gong, Q. Zhou, Q. Li, F. Wang, X. Zeng, M. Gao, *Mater. Sci. Eng. A* 826 (2021) 141942.
- [475] H. Galarraga, R.J. Warren, D.A. Lados, R.R. Dehoff, M.M. Kirk, *Eng. Fract. Mech.* 176 (2017) 263–280.
- [476] M. Shamir, A.K. Syed, V. Janik, R. Biswal, X. Zhang, *Mater. Charact.* 169 (2020) 110576.
- [477] F. Wang, L.M. Lei, X. Fu, L. Shi, X.M. Luo, Z.M. Song, G.P. Zhang, *J. Mater. Sci. Technol.* 132 (2023) 166–178.
- [478] D. Agius, K.I. Kourousis, C. Wallbrink, *Metals* 8 (2018).
- [479] Z.W. Xu, A. Liu, X.S. Wang, *Mater. Sci. Eng. A* 767 (2019).
- [480] M. Jiang, B. Devincre, G. Monnet, *Int. J. Plast.* 113 (2019) 111–124.
- [481] B. Liu, K. Wang, R. Bao, F. Sui, *Int. J. Fatigue* 137 (2020).
- [482] N. Chen, H. Kou, Z. Wu, F. Qiang, K. Hua, J. Fan, B. Tang, J. Li, J.M. Molina-Aldareguia, *Mater. Sci. Eng. A* 824 (2021).
- [483] Z. Cao, H. Deng, W. Qiu, L. Chen, D. Wu, *Adv. Eng. Mater.* 24 (2022) 1–9.
- [484] Y. Zhang, Z. Zhai, Z. Wu, W. Lin, R. Yang, Z. Zhang, *Mater. Des.* 236 (2023) 112488.
- [485] J. Liu, Y. Li, Y. Zhu, Y. Yang, R. Zhang, Z. Zhang, A. Huang, K. Zhang, *Mater. Sci. Eng. A* 859 (2022) 144201.
- [486] S.V. Zherebtsov, G.S. Dyakonov, A.A. Salem, V.I. Sokolenko, G.A. Salishchev, S. L. Semiatin, *Acta Mater.* 61 (2013) 1167–1178.
- [487] K. Yao, S. Xin, Y. Yang, Y. Du, J. Dai, T. Li, X. Min, *Scr. Mater.* 213 (2022).
- [488] M.C. Zang, H.Z. Niu, S. Liu, J.S. Yu, H.R. Zhang, D.L. Zhang, *J. Alloy. Compd.* 923 (2022).

- [489] S.M. Jamshid Mahdi, Kottman Michael, Snodderly Kirstie, Williams Jacob, Strateg. Guide. Addit. Manuf. Situ Monit. Technol. Readiness (2023).
- [490] W. Liu, J. Huang, J. Liu, X. Wu, K. Zhang, A. Huang, Int. J. Fatigue 148 (2021) 106203.
- [491] D. Wu, M. Hao, T. Zhang, Z. Wang, J. Wang, G. Rao, L. Zhang, C. Ding, K. Zhou, L. Liu, D. Wang, Y. Wang, Acta Mater. 257 (2023).
- [492] Z. Yao, X. Jia, J. Yu, M. Yang, C. Huang, Z. Yang, C. Wang, T. Yang, S. Wang, R. Shi, J. Wei, X. Liu, Mater. Des. 225 (2023) 111559.
- [493] H. Fan, C. Wang, Y. Tian, K. Zhou, S. Yang, Mater. Sci. Eng. A 871 (2023) 144907.
- [494] P.F. Jiang, M.H. Nie, J.Z. Teng, X.H. Cui, C.Z. Liu, X.G. Zhang, Z.H. Zhang, Mater. Sci. Eng. A 890 (2024) 145896.
- [495] K. Wei, F. Li, G. Huang, M. Liu, J. Deng, C. He, X. Zeng, Mater. Sci. Eng. A 802 (2021) 140644.
- [496] S. Wei, C. Hutchinson, U. Ramamurty, Scr. Mater. 230 (2023) 115429.



Mr. Jianwen Liu is a PhD candidate in the Monash Centre for Additive Manufacturing (MCAM) at Monash University, Australia. He received his bachelor's degree from Hefei University of Technology in 2018, and M.Eng. degree from the University of Shanghai for Science and Technology in 2022. His research focuses on microstructure characterizations and mechanical performance of additively manufactured titanium alloys. His publication details can be found: <https://scholar.google.com.au/citations?user=DXHH3skAAAAJ&hl=en>.



Dr. Kai Zhang received his Ph.D. from Monash University and had been working as a research fellow in Monash Centre for Additive Manufacturing from 2015 to 2019. He is currently an associate professor in the Soochow University. His research area is mainly in the field of additively manufacture titanium alloys, particularly in the correlation between the additively manufacturing process, microstructure evolution and mechanical performance. He is also specialized in the fatigue performance research of titanium alloys. Dr. Zhang's publication list can be found: <https://scholar.google.com.au/citations?user=q0OO9fwAAAAJ&hl=en>.



1=en&oi=ao.

Dr. Yuman Zhu obtained his PhD degree by Monash University. He currently serves as the Deputy Director of Monash Centre for Additive Manufacturing (MCAM) at Monash University, Australia. He is also an ARC Future Fellow within the department of Materials Science and Engineering. Dr. Zhu's research interests involve investigating the additively manufactured metallic materials, and application of advanced microscopy techniques to study the rapid solidification and phase transformations associated with the additive manufacturing process, aiming to establish processing-microstructure-property relationships and advance the application of additive manufacturing. Dr. Zhu's publication list can be found: <https://scholar.google.com.au/citations?user=hpoClGsAAAJ&hl=en&oi=ao>



Prof. Aijun Huang holds a PhD from the University of Birmingham, UK. He is a Fellow, Chartered Engineer and Chartered Scientist of the Institute of Materials, Minerals and Mining UK. He is currently the Associate Dean – International, Faculty of Engineering and the Director of Monash Centre for Additive Manufacturing and a full tenured professor in the Department of Materials Science and Engineering, Monash University. Prior to his appointment at Monash University, Prof. Huang was an industry technical expert for a number of multinational corporations. Prof. Huang held the position of the Executive Vice President of the High-Performance Materials Business Unit which exclusively manufacturing all aerospace metallic materials in Baosteel Group; a Fortune Global 500 company. From 2006–2012, Prof. Huang was the Titanium Specialist of Rolls Royce Derby globally leading the titanium and titanium aluminides fundamental research within the company where he was elected to the Rolls Royce Engineering Leadership List in 2011. Prof. Huang's publication details can be found: https://scholar.google.com.au/citations?user=gwBOe_4AAAJ&hl=en.